

RCA Review

September 1974 Volume 35 No. 3

RCARC1 35(3) 331-479, (1974)

RCA Review, published quarterly in March, June, September and December by RCA Research and Engineering, RCA Corporation, Princeton, New Jersey 08540. Entered as second class matter July 3, 1950 under the Act of March 3, 1879. Second-class postage paid at Princeton, New Jersey, and at additional mailing offices. Effective Jan. 1, 1971, subscription rates as follows. United States and Canada: one year \$6.00, two years \$10.50, three years \$13.50; in other countries, one year \$6.40, two years \$11.30, three years \$14.70. Single copies (except for special issues) up to five years old \$3.00

RCA Review

A technical journal published quarterly by RCA
Research and Engineering in cooperation with
the subsidiaries and divisions of RCA.

Contents

- 333 A. N. Goldsmith—In Memoriam
- 335 A Facsimile System Using Room-Temperature Injection-Laser Scanning
P. V. Goedertier, I. Gorog, J. D. Knox, I. Ladany, and J. P. Witke
- 341 Video Processing in Charge-Transfer Image Sensors by Recycling of Sig-
nals Through the Sensor
P. K. Weimer, W. S. Pike, F. V. Shallcross, and M. G. Kovac
- 355 Low-Loss Broadband Microwave Ultrasonic Delay Lines Using Ion-Beam-
Milled Shear-Wave Transducers
David M. Stevenson and J. J. Hanak
- 372 S-Band Trapatt Amplifiers with Four-Layer Diode Structures
H. Kawamoto, S. G. Liu, H. J. Prager, and E. L. Allen, Jr.

An Introduction to the Science and Technology of Liquid Crystals—II

- 388 Introduction to the Molecular Theory of Smectic-A Liquid Crystals
Peter J. Wojtowicz
- 408 Introduction to the Elastic Continuum Theory of Liquid Crystals
Ping Sheng
- 433 Electrohydrodynamic Instabilities in Nematic Liquid Crystals
Dietrich Meyerhofer
- 447 Liquid-Crystal Displays—Packaging and Surface Treatments
L. A. Goodman
- 462 Pressure Effects in Sealed Liquid-Crystal Cells
Richard Williams
- 468 Technical Papers
- 471 Patents
- 473 Authors

RCA Corporation

Robert W. Sarnoff Chairman of the Board and Chief Executive Officer
A. L. Conrad President and Chief Operating Officer

Editorial Advisory Board

Chairman, J. A. Rajchman RCA Laboratories

A. A. Ahmed Solid State Division
E. D. Becken RCA Global Communications
G. D. Cody RCA Laboratories
D. M. Cottler Government and Commercial Systems
N. L. Gordon RCA Laboratories
G. B. Herzog RCA Laboratories
J. Hillier RCA Research and Engineering
E. O. Johnson International Licensing
J. Kurshan RCA Laboratories
C. H. Lane Electronic Components
D. S. McCoy Consumer Electronics
K. H. Powers RCA Laboratories
R. E. Quinn RCA Laboratories
P. Rappaport RCA Laboratories
J. H. Scott, Jr. RCA Laboratories
L. A. Sholliff International Licensing
T. O. Stanley RCA Laboratories
F. Sterzer RCA Laboratories
J. J. Tietjen RCA Laboratories
W. M. Webster RCA Laboratories

Secretary, Charles C. Foster RCA Laboratories

Editor Ralph F. Clafone

Associate Editors

W. A. Chisholm RCA Limited (Canada)
M. G. Gander RCA Service Company
W. O. Hadlock RCA Research and Engineering
D. R. Higgs Missile and Surface Radar Division
W. A. Howard National Broadcasting Company
C. Hoyt Consumer Electronics
E. McElwee Solid-State Division
C. A. Meyer Electronic Components
M. G. Pletz Government and Commercial Systems
C. W. Sall RCA Laboratories
I. M. Seldeman Astro-Electronics Division
R. N. Hurst Communications Systems Division

© RCA Corporation 1974 All Rights Reserved Printed in USA



Alfred N. Goldsmith
Sept. 15, 1888—
July 1, 1974

Dr. Alfred N. Goldsmith died on July 1, 1974 at the age of 86. He was co-founder of the Institute of Radio Engineers, which merged in 1963 with the American Institute of Electrical Engineers to form the Institute of Electrical and Electronics Engineers, an organization that now has a membership of some 175,000. When RCA was formed in 1919, Dr. Goldsmith was first Director of Research and then Vice President and General Engineer until 1931, when he became Senior Technical Consultant. His many achievements and honors have been widely documented in the world press.

Dr. Goldsmith's passing is a particularly sad loss to those who have been involved with the publication of RCA Review over the years. He was the elder statesman of the Board of Editors, which he served for 39 years, and yet at the same time displayed great vigor, remarkable foresight, and constructive enthusiasm. Until two years ago, when failing health brought on a forced retirement, he always made himself available, and was frequently called on, for advice and assistance. His energy and insight never flagged.

We have lost one of the great pioneers of the electronics art.

A Facsimile System Using Room-Temperature Injection-Laser Scanning

P. V. Goedertler, I. Gorog, J. D. Knox, I. Ladany, and J. P. Wittke

RCA Laboratories, Princeton, N. J. 08540

Abstract—This paper reports the first use of cw room-temperature injection lasers in a scanning facsimile system. The document reader can resolve about 2000 spots in each horizontal line of its raster scan, which is close to the performance attained using an He-Ne gas laser. Our results thus suggest that these small, efficient lasers can replace gas lasers in many applications.

Introduction

The recent development of $(\text{AlGa})\text{As}-(\text{AlGa})\text{As}^1$ and $(\text{AlGa})\text{As-GaAs}^2$ cw room-temperature injection lasers with useful operating lifetimes of thousands of hours permits them to be used to replace bulkier, more fragile gas lasers in many applications. Injection lasers are very small, rugged, and reliable. The required power supply must provide only a few watts at a few volts. In addition to these advantages, the lasers can be readily intensity modulated at rates up to hundreds of megahertz by simply modulating the drive current—an important capability in several possible applications currently under study.³

Document Reader

This paper reports on the application of this new device to a document reader, where it is used as the source in a flying-spot scanner.*

* Details of the optics, drive electronics and signal detection and processing techniques will be given in a forthcoming publication.

The operation of the scanner is indicated in Fig. 1. The astigmatic beam from the laser is shaped to a nearly round cross section by an optical chain comprised of spherical and cylindrical lenses. The shaped beam is then brought to a focus in the scanning plane, where

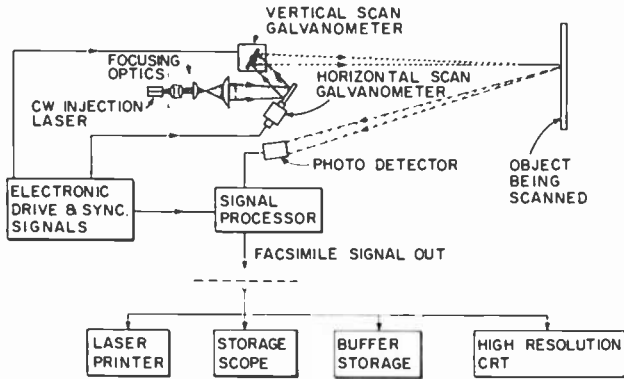


Fig. 1—Schematic representation of the document reader.

the document is placed. Scanning in two orthogonal directions is accomplished using two galvanometer-driven plane mirrors. Ramp voltages are applied to both galvanometers, providing a fast horizontal line scan and a slow vertical scan, raster-scanning the document in 14.0 seconds.

The light scattered from the scanned document is detected in a photomultiplier. Alternatively, an array of silicon photodetectors is used. Spectral filtering is used to minimize the perturbing effects of ambient light. The output signal from the detector is an analog signal corresponding to the diffuse reflectivities of the sequentially scanned document. This signal is fed into a comparator circuit that defines a black-white threshold level. Use of the comparator eliminates the requirement of extreme linearity throughout the system that would otherwise be necessary. The signal from the comparator can be used or displayed in any of several ways, as indicated in Fig. 1.

The oxide-isolated, stripe-geometry laser, developed at this laboratory, is of the double-heterojunction type, with aluminum in the active (high-index) region, as well as in the lower-index waveguiding regions of the structure; the resulting emission wavelength was about 810 nm. As seen in Fig. 2, the far-field emission pattern of such a source is far from axially symmetric. Here, the injection laser used in

this work has been scanned in two orthogonal directions, in the plane of the junction and perpendicular to this plane. When the laser is driven well above threshold, the emission in the plane of the junction is in a narrow, sharply directional beam only a few degrees in width, even though the laser oscillates in several modes simultaneously. Perpendicular to the plane of the junction, due to the narrowness of the

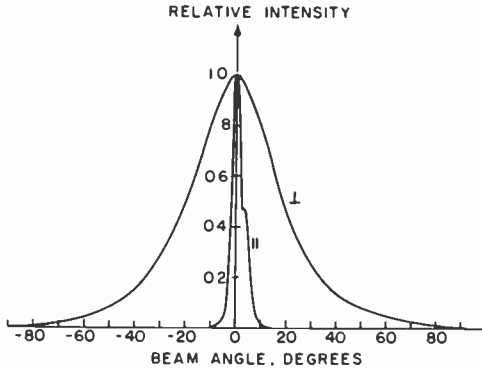


Fig. 2—Far-field beam patterns of the cw room-temperature injection laser source, scanned in the plane of the p-n junction and perpendicular to the junction plane. Laser output power during the scan was 10 milliwatts.

active high-index region, the fields of all the oscillating modes are the same, and the beam pattern, determined by the optical properties of the various layers comprising the laser, is much broader. The patterns were taken at a beam power of 10 milliwatts. The multimode nature of the pattern in the plane of the junction is suggested in the figure but not marked. At this power level, the laser beam is essentially linearly polarized, with the optical E -vector in the plane of the junction.

The laser was operated at an output power of 10 mW. The optical system was able to focus about 3 mW onto the document, the losses occurring predominantly at the lens and mirror surfaces. The laser wavelength closely matched the peak of the spectral responses of the (S-1) photomultiplier and silicon photodetectors used. To utilize the full laser output power, an anamorphic optical system is clearly desirable. Such a system was used to produce the nearly round focused spot in the scan plane indicated in Fig 3. It consists of a $\times 10$ microscope objective close to the emitting facet of the laser, followed by two cylindrical lenses of focal lengths 18 mm and 100 mm. The hori-

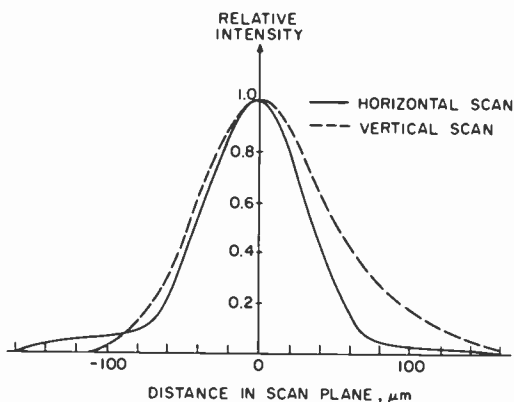


Fig. 3—Focused laser spot in the object plane, scanned horizontally and vertically. The total horizontal scan width was 20 cm.

zontal scan of Fig. 3 is the plane of the laser junction, while the vertical scan direction is perpendicular to the junction plane.

As shown by the figure, the spot diameter at the scan plane was about 100 μm . The total scan length was 20 cm, at an optical lever length of 74 cm. The scan angle was about 15° . Thus, approximately 2000 spots can be resolved in each horizontal scan. The corresponding spatial frequency response (with the above dimensions) is shown in Fig. 4. Typical results obtained with the injection laser document reader are shown in Fig. 5, which is a photograph of (a portion of) the faceplate of a storage oscilloscope that was used to display the output from the signal comparator. Since the display unit had only a resolution of 300 line-pairs across its face, its resolution was inadequate to

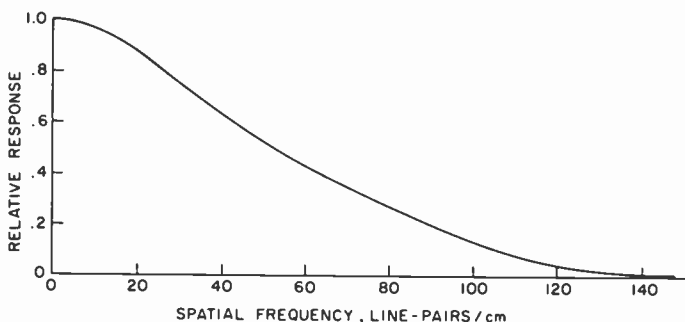


Fig. 4—The spatial-frequency-response function (Fourier transform) corresponding to the horizontal scan in Fig. 3.

show the full performance of the document reader. Nevertheless, a reasonable impression of the capabilities of the system can be obtained from the figure.

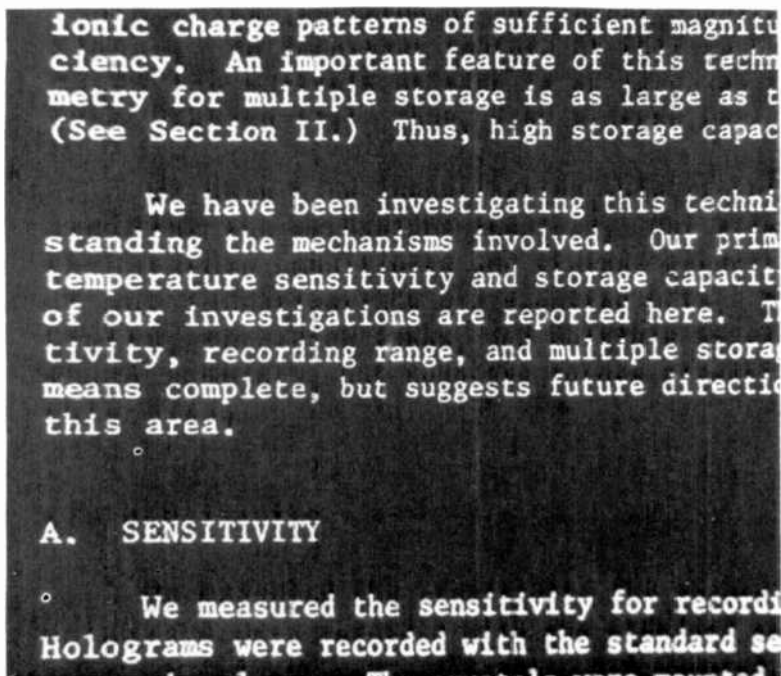


Fig. 5—Portion of a storage-oscilloscope display of a page of typed text as read by the document scanner.

Conclusions

High-resolution flying-spot scanners can be constructed with room-temperature cw injection lasers. These lasers provide an intense light source that can be focused, with simple optics, into a spot comparable in size to that obtainable using gas lasers. It is clear that they will find other applications in a variety of equipments that currently use gas lasers.

Acknowledgments

The injection lasers used in this work were developed in a program partially supported by the Office of Naval Research, Arlington, Vir-

ginia, and by NASA Langley Research Center, Hampton, Virginia. The support and encouragement of Henry Kressel is gratefully acknowledged.

References:

¹ I. Ladany and H. Kressel, to be published.

² R. L. Hartman, J. C. Dymont, C. J. Hwang, and M. Kuhn, "Continuous Operation of GaAs-Ga_{1-x}Al_xAs Double-Heterostructure Lasers with 30°C Half-Lives Exceeding 1000 Hours," *Appl. Phys. Lett.*, **23**, p. 181 (1973).

³ E.g., I. Gorog, J. D. Knox and P. V. Goedertier, "A Television Rate Laser Scanner—I. General Considerations," *RCA Review*, **33**, p. 623 (1972); I. Gorog, J. D. Knox, P. V. Goedertier, and I. Shidlovsky, "A Television Rate Laser Scanner—II. Recent Developments," *RCA Review*, **33**, p. 667 (1972).

Video Processing in Charge-Transfer Image Sensors by Recycling of Signals Through the Sensor

P. K. Weimer, W. S. Pike, F. V. Shallcross, and M. G. Kovac*

RCA Laboratories, Princeton, N.J. 08540

Abstract—The recycling of video signals from the output of a solid-state image sensor back into its input permits the sensor to perform various types of analog signal processing simultaneously with image pickup. Early experiments on background subtraction, multiple readout of a single pattern, and motion detection are discussed.

1. Introduction

A useful feature of charge-transfer scanning in image sensors is the ease with which an input register can be incorporated into the device permitting it to function in an alternative mode as a memory or analog delay line. Such an input register was included in an early three-phase charge-coupled sensor¹ made at Bell Laboratories, and its operation as a "series-parallel-series" analog delay line was reported.² Similar experiments on sensing and delay were performed at RCA Laboratories using a smaller three-phase sensor³ having 45×60 elements.† Preliminary experiments were carried out with this device using a novel mode of operation in which the output signal from the sensor was simultaneously fed back to its input to obtain other useful forms of signal processing. By such recycling of signals it was shown³

* Presently with Dytron, Inc., Waltham, Mass. 02154.

† The 45×60 element sensor was fabricated at RCA Laboratories under ONR Contract No. N00014-71-C-0415.

that with a minimum of peripheral equipment (1) multiple fields or lines of the display could be repeated, (2) image motion between successive fields could be detected, and (3) nonuniform fixed background patterns could be subtracted from the signal. The recycling of signals to obtain enhanced accuracy in measurement of transfer efficiency in CCD's has also been reported.⁴

The purpose of the present paper is to discuss more fully the concept of recycling of signals in image sensors and to report some of the early recycling experiments that were performed. The feasibility of signal processing by this means has been established, but a full evaluation of its effectiveness has not been carried out.

2. General Description of Video Recycling in Image Sensors

The recycling of video signals back into the input of an image sensor permits the sensing and delay capabilities of the sensor to be used si-

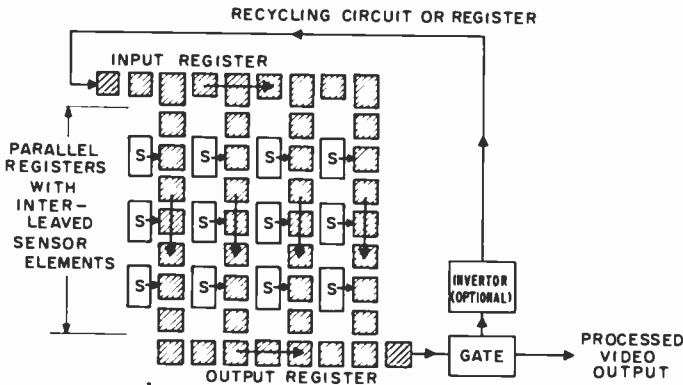


Fig. 1—Block diagram of vertical-transfer charge-coupled image sensor having nonilluminated registers and interleaved sensor elements. Video signals are recycled by direct coupling between the output and input register.

multaneously. Signals from successive frames can be repeated and combined within the sensor for various forms of signal processing. Although video recycling can also be accomplished in other types of sensors, such as a photodiode array with *XY* address strips, the method is particularly convenient with charge-transfer sensors. Consider, for example, a vertical-transfer charge-coupled sensor with nonilluminated registers and interleaved photoelements, as shown in Fig. 1. This structure differs from the currently available interleaved

sensors⁵ by the addition of an input register. By coupling the output of the sensor to its input during the readout of signals it is possible in one scan to replace a given charge pattern by the same or modified form of the original pattern. The recycled pattern can then be read out again or combined internally with subsequent picture information to carry out the desired signal-processing function.

In the normal operation of this sensor, the photoelements are illuminated continuously by the optical image, causing a picture charge pattern to be accumulated on the sensor elements. These charges are transferred simultaneously to the adjacent registers during the vertical retrace period. Scanning is accomplished by transferring the entire pattern step-wise to the output register, where each row is transferred out in sequence. The clock drives for the vertical registers operate at the horizontal line frequency while the output (and input) registers are driven at the element rate.

For successive recycling operations it is necessary to be able to control the return position of the recycled pattern within the registers. In most cases it is desired to return each elemental charge (or some function of the charge) to exactly the same location at which the charge first entered the register. This can be done provided the following conditions are met:

- (1) Transfer losses and charge leakage are sufficiently low that resolution and signal are not appreciably degraded.
- (2) The feedback circuit and the input and output registers are designed so that each line of information returns to coincidence with the column from which it originated. The horizontal blanking interval allows the input and output registers to operate for extra cycles, if necessary, to compensate for small delays in the feedback loop.
- (3) The vertical clock drives are pulsed for the correct number of cycles in each field to match the total number of stages in the vertical registers. Additional scanning lines can be inserted into the vertical blanking interval if needed to compensate for more than one line delay in the feedback loop.

The summing of the recycled pattern and the new pattern occurs within the registers during the vertical retrace period when the new pattern is dumped into the registers. Since the registers transfer only one type of carrier, negative-polarity signals must be recycled as a negative modulation of a fixed bias charge. It is therefore important that the input and output circuits be linear and that the combined charge not exceed the full well capacity of the registers. Various types of low-noise, linear input and output circuits have been described.⁶ The feedback connection could be a charge-transfer register located

on the same chip, or an external circuit coupling the input and output registers.

Fig. 2 shows how the sensor of Fig. 1 can be operated with video recycling for multiple nondestructive readout, motion detection, and background subtraction. For multiple readout, the sensors are exposed during the first field period and the charge pattern is transferred into the vertical registers at the end of this period. During the

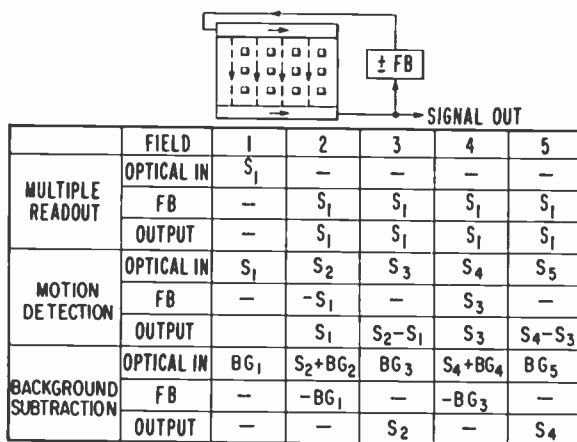


Fig. 2—Operation of a charge-transfer sensor such as shown in Fig. 1 with video recycling for multiple readout, background subtraction, and motion detection.

second and subsequent fields, the charge pattern is read out and simultaneously recycled back into the vertical registers. The recycled signal can be either positive or negative, but in the latter case the displayed signal would alternate in polarity in successive fields. With positive feedback, care must be taken to avoid instability.

For motion detection, the sensor array is exposed during each field, but recycling (with negative polarity) occurs only on alternate fields. The output signal alternates between the normal signal and a difference signal whose value would approach zero in the absence of motion between successive images.

Background subtraction in an image sensor is of interest in applications where the picture signal level is small compared to a fixed background pattern. Such a pattern can be caused by nonuniform dark current in the sensor. Although dark current background can usually be kept small enough to not be objectionable at normal signal

levels, it can limit the performance at low illumination levels. Figs. 2 and 3 show how recycling of the background signal on alternate fields could be used to subtract out the nonuniform background component in the low-light signal. An optical shutter shields the sensor from the

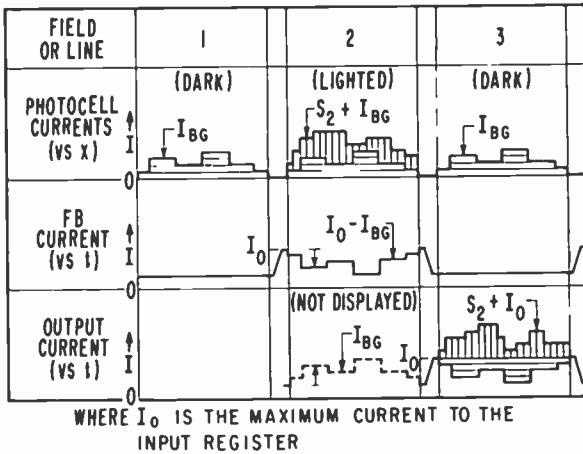


Fig. 3—Use of video recycling for subtraction of background signals caused by nonuniform dark current in an image sensor.

light during fields 1, 3, 5, etc., so that only a dark-current pattern is accumulated on the sensor elements during these fields. At the end of each odd field, the dark-current pattern is transferred into the empty vertical registers. During the even-field scanning period two processes occur: (1) the dark-current signal (BG) is transferred out and recycled with inverted polarity, and (2) a picture signal pattern with accompanying background signal ($S+BG$) is accumulated on the sensor elements. The two signals $S+BG$ and $-BG$ are combined in the register during the next vertical retrace period and the uniformized picture signal S is read out during the odd fields. Fig. 3 illustrates how the inverted background signal is recycled by negatively modulating a fixed input signal I_0 .

It is apparent that this background subtraction method is only 50% efficient in utilization of total light and total bandwidth. Background subtraction would not be useful in sensors in which statistical noise, such as shot noise, transfer noise, or output circuit noise, was limiting the performance. Fortunately such noise sources⁷ can be kept relatively small in charge-coupled sensors, so that a factor of two loss in

total signal can often be tolerated. However, in sensors that have no image section to provide picture charge multiplication prior to scanning, or in sensors that are not cooled to reduce dark currents, the integrated background charge arising from the dark current can be much larger than the picture signal at very low light levels. Under such conditions the spatial variations in the background signal are likely to be more objectionable than the fluctuation noise arising from all other noise sources. A reduction of this fixed background pattern by means of recycling thus offers a means for detecting low-level signals that would otherwise be unrecognizable in such a sensor. The same procedures could also be applied to infrared sensors in which dark current patterns obscure the image.

The use of video recycling is not limited to interleaved sensors of the type shown in Fig. 1. Preliminary experiments on recycling were

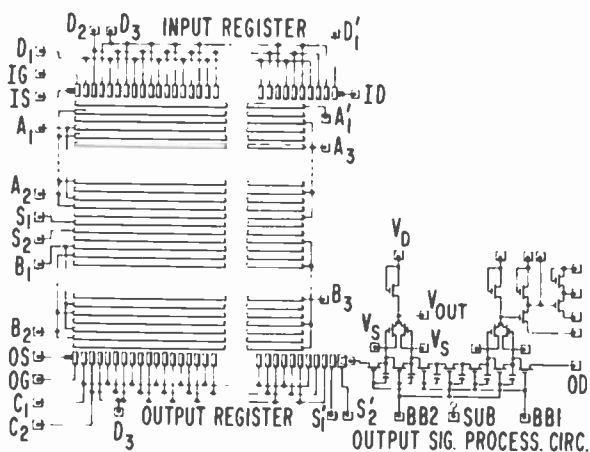


Fig. 4—Layout for a 45×60 element (90×60 interleaved) three-phase charge-coupled sensor including a bucket-brigade output circuit and an input register used for recycling experiments.

carried out on a 45×60 element frame-transfer sensor described in the next section.

3. The 45×60 Element Sensor Used in the Recycling Experiments

Figs. 4 and 5 show a layout and photograph of the three-phase illuminated-register sensor used in these tests.³ The clock electrodes are coplanar aluminum strips with $2.5 \mu\text{m}$ gaps. The sensor area is illumi-

nated from the metallized side through the gaps and the registers are of the n-channel surface-transfer type. The sensor and storage areas each contain 60 vertical registers with 45 stages in each portion. The resulting number of picture elements is 45×60 in the normal mode or 90×60 in the interlaced mode.⁸

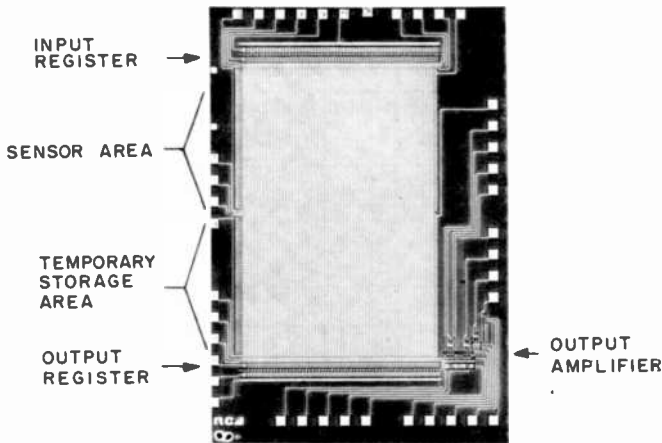


Fig. 5—Photomicrograph of the 45×60 element charge-coupled sensor. The three-phase registers having coplanar aluminum electrodes are directly illuminated from metallized side.

Operation of an illuminated-register frame-transfer sensor requires that the clock supplies connected to the sensor area ($A_1A_2A_3$) be stopped during each field scanning period so that a picture charge pattern can be integrated under one set of electrodes. This pattern is then transferred into the storage area during the subsequent vertical retrace period by activating both the $A_1A_2A_3$ and $B_1B_2B_3$ clock supplies at a relatively fast rate. The readout of the video signal occurs during the following field period, when the pattern is transferred from the storage area to the output register. The $B_1B_2B_3$ clocks operate at line frequency during the scanning periods, causing successive rows of charge to be dropped into the output register during each horizontal retrace interval. Charge integration and scanning proceeds continuously for successive fields as shown in Fig. 6a.

The output clocks $C_1C_2C_3$ were operated at elemental frequency for 65 cycles and were then stopped during the horizontal retrace period with C_2 high and C_1 and C_3 low. The input clocks $D_1D_2D_3$ had

identical waveforms to the output clocks, except that all three phases were kept low during the horizontal retrace period. All four clock drives (A, B, C, D) and the two-phase bucket-brigade clocks were independently adjustable in amplitude and bias.

The frame transfer sensor could be operated as a series-parallel-series delay line by introducing an electrical signal into the input reg-

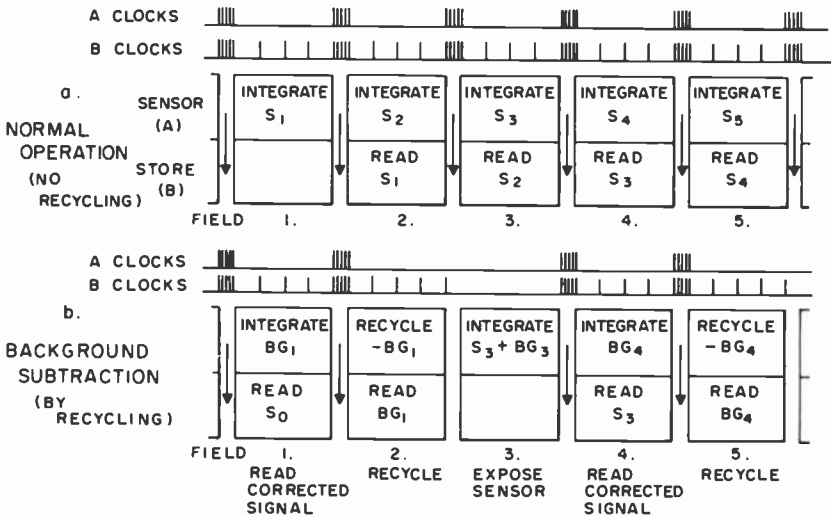


Fig. 6—Clock waveforms for the vertical registers and the resulting function of the sensor and storage regions of the 45×60 frame transfer sensor under two modes of operation: (a) normal sensor mode and (b) background subtraction with recycling of every third field.

ister. For this mode of operation the $A_1A_2A_3$ waveforms described above were not suitable, but successive picture fields containing 45×60 elements could be delayed satisfactorily by driving both the sensor and storage areas with the $B_1B_2B_3$ clock waveforms shown in Fig. 6a. Modified B clocks with 90 equally spaced pulses would be required to utilize the full 90×60 element storage capacity of the array.

The requirement for stopping the vertical clocks in the sensor area for charge integration during each scanning period precludes the recycling of video signals in the normal frame-transfer mode. Fig. 6b illustrates an operating sequence for this sensor that permits recycling signals on every third frame. During field 1, the background pattern BG is integrated. During field 2, the background signal is read out, inverted, and recycled into the sensor area. During field 3,

the sensor area is illuminated by light from the scene, causing the charge pattern $S+BG$ to be built on top of the stored inverted background signal $-BG$. The resulting output signal S is read out (but not recycled) during field 4, when a new background charge is being integrated. It is noted that the optical shutter is open one third of the time for light exposure. This system may be compared with the interleaved sensor shown in Fig. 1, which allowed the shutter to be open one half the time. If the light were sufficiently intense that a full $1/60$ -sec exposure time were not required, a light flash during alternate vertical retrace periods could be used with recycling in the series-parallel-series clocking mode described above.

4. Preliminary Tests on Recycling of Signals

The 45×60 element frame-transfer sensor served to demonstrate the feasibility of recycling signals in the manner proposed, although the experiments performed were not sufficient to evaluate the approach quantitatively. Fig. 7 shows a picture transmitted by one such sensor

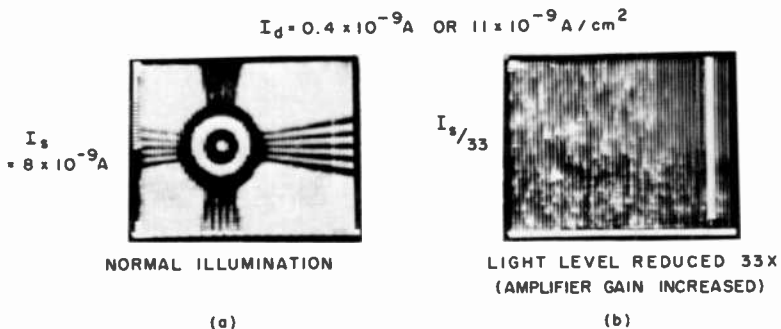


Fig. 7—Pictures transmitted by a 45×60 element sensor showing the effect of nonuniform dark current in limiting low-light-level performance in the normal operating mode. Amplifier gain was increased for the low-light picture in an effort to bring out the picture.

under (a) high light levels and (b) with the light reduced by a factor of 33. In the low-light picture, the amplifier gain was increased in an effort to restore the picture. Although fluctuation noise was not limiting the performance in either case, the low-light picture was completely obscured by the dark-current background. While the dark current spots in this particular sensor were probably more conspicuous than normal, this type of limitation could occur in most sensors

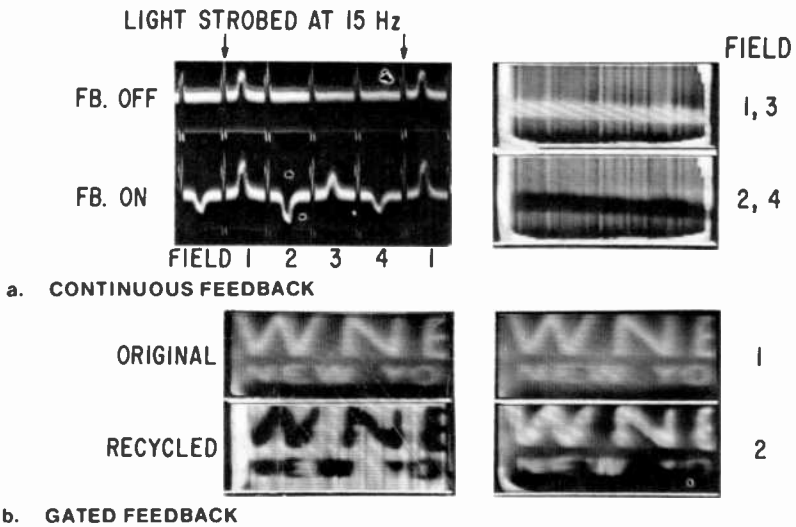


Fig. 8—Video signal recycling in the 45×60 element frame-transfer sensor: (a) multiple (four) readouts of the sensor for each exposure (inverted polarity feedback) and (b) gated feedback of signal with greater than unity gain in the feedback loop.

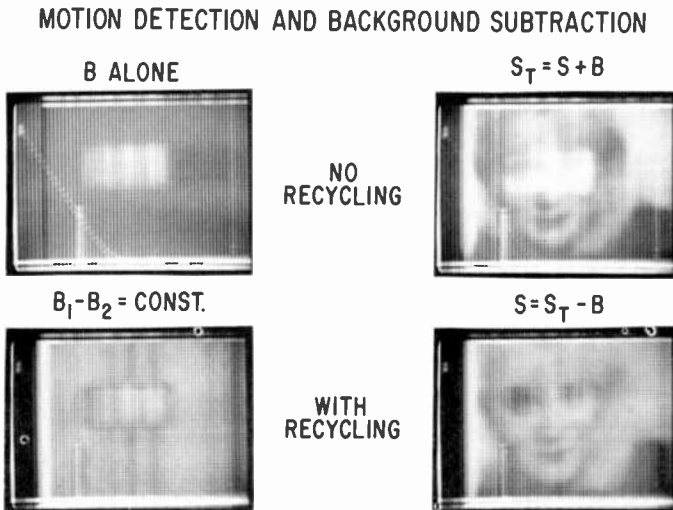


Fig. 9—A demonstration of motion detection and signal component separation with strobed illumination of the frame-transfer sensor (recycling on alternate frames).

at very low levels, i.e., under conditions where background subtraction would be useful.

Fig. 8 illustrates the multiple recycling of a single image produced by a horizontal white bar in the picture. The feedback loop contained an external video amplifier that could be inverted and gated as required. In the upper pictures (a) the signal was recycled three times with the feedback polarity inverted. As would be expected, the output signal is inverted in successive fields. Multiple recycling without inversion tends to be unstable if the loop gain exceeds unity. Stable feedback in either polarity with greater than unity gain is possible if the feedback loop is gated off after one cycle (lower pictures). The vertical stripes noted in the recycled pictures were variable in position and intensity and appeared to be associated with uneven transfer of charge from the input register to the columns.

The technical feasibility of background subtraction was demonstrated in two different arrangements. In Fig. 9 the sensor and storage areas were both driven with the $B_1B_2B_3$ clock (as in a series-parallel-series delay line) while two pictures labeled B and S were flashed onto the sensor area by two strobed illuminators. Picture B (a rectangular white spot simulating a nonuniform background) was flashed at 60 fields per second, while picture S (girl's face) was flashed at 30 fields per second. The combined image (labeled S_T) represented a normal picture having a nonuniform background without recycling. The S component of the combined picture was recovered as shown in the picture on the lower right by recycling the inverted B component. The effect of subtracting the B component from itself by recycling, as in motion detection, is shown on the lower left. The edges of the difference picture are visible because the resolution of the recycled picture has been somewhat degraded by the added number of transfers. In spite of the lack of perfect cancellation of two stationary images, the edges of the light spot were clearly enhanced when the second image was moved relative to the first.

Fig. 10 shows an alternate experiment demonstrating background subtraction by recycling. In this case the sensor was operated as shown in Fig. 6b with a normal $\frac{1}{60}$ -second illumination period occurring every third field. The object was to remove or diminish the intensity of several high-dark-current (white) spots relative to the picture signal (the white rectangle). The external feedback loop included a gated inverting amplifier with no provision for adjustment of delay. In this case, the horizontal position of the recycled negative signal was controlled to the nearest element spacing by adjusting the pulse length of the first vertical clock electrode (labeled A_1' in Fig. 4). As is

evident from the pictures, the recycled spot pattern was somewhat smeared out due to poor transfer efficiency, and did not provide good cancellation even at the best coincidence with the original pattern. However, the overall intensity of the spots was reduced relative to the signal intensity by means of recycling. It would be expected that, by

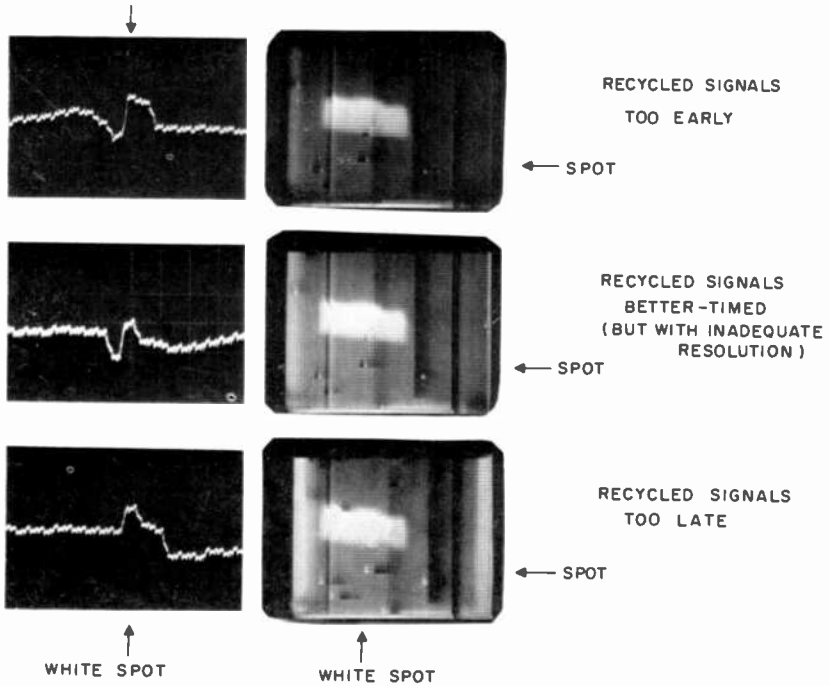


Fig. 10—Background subtraction with recycling every third field in the frame transfer sensor. Horizontal position of the recycled background spots was varied by adjustment of phase of pulse to B_1' electrode. The oscilloscope trace shows

using a sensor with lower transfer losses and by taking greater care in controlling the coincidence of the recycled signal, a significant reduction in background spots could be achieved. However, it was also apparent that the recycling technique is critical to control and will require careful adjustment to provide a significant improvement in overall operating sensitivity. In most cases, the recycling procedure is not useful in removing the effects of major column defects, such as those occurring in Fig. 10.

5. Discussion

The recycling of signals through an image sensor containing an input register offers an economical means for doing certain types of signal processing within the sensor. Although similar processing functions could be carried out using a separate series-parallel-series array operated in parallel with the sensor, the array cost and power consumed would be increased. Either method requires registers with transfer losses no more than half that which would be adequate for the sensor alone. A sensor with recycling is more limited in dynamic range, since a single well must handle both the original and the recycled signal without loss of linearity.

Experimental tests of recycling demonstrated that multiple read-out of signals, background subtraction, and motion detection could be accomplished by this process. These tests also showed that in recycling through an external circuit, the adjustment of signal levels and control of timing are critical. It would be expected that feedback by means of additional charge-transfer registers on the same chip could be more easily controlled. Such a feedback register might include a large number of stages in which the increased delay would be compensated by operating the input register through extra cycles extending into the horizontal and vertical retrace period. Alternatively, if the feedback path comprised only a few bucket-brigade stages with a charge amplifier to drive the higher capacitance coupling lead, the short delay could be compensated by operating the input register for a few extra cycles extending into the horizontal retrace period.

The practical value of background subtraction as a means of lowering the effective light level threshold of an uncooled, nonintensified sensor will depend upon numerous factors. Clearly, background subtraction would be of no value under conditions where actual performance is limited by statistical noise. It would only be useful at moderately low light levels where statistical noise is not objectionable but where background variations in the sensor provide a practical limit on performance. Other solutions to the background problem include cooling of the sensor and use of an image intensifier prior to the charge-coupled sensor. Background subtraction by recycling may be more convenient than these approaches, provided a satisfactory optical shutter can be found.

It is apparent that recycled signals could be returned to the sensor at other points, such as the input of the output register. This system might be useful in combining signals from successive lines, or for repeating a given line before proceeding to the next.

Acknowledgments

The authors are indebted to V. L. Frantz, G. M. Meray, R. Miller, and J. L. Pointkowski for assistance in fabrication and testing of the 45×60 element sensor.

References:

- ¹ C. H. Séquin, D. A. Sealer, W. J. Bertram, Jr., M. F. Tompsett, R. R. Buckley, T. A. Shankoff, and W. J. McNamara, "A Charge-Coupled Area Image Sensor and Frame Store," *IEEE Trans. Electron Devices*, **ED-20**, p. 244 (1973).
- ² M. F. Tompsett and E. J. Zimany, Jr., "Use of Charge-Coupled Devices for Delaying Analog Signals," *IEEE Solid-State Circuits*, **SC-8**, p. 151 (1973).
- ³ P. K. Weimer, W. S. Pike, M. G. Kovac, and F. V. Shallcross, "The Design and Operation of Charge-Coupled Image Sensors," Digest of Technical Papers, p. 132, 1973 IEEE International Solid State Circuits Conf., Phila., Pa. Also in *Data and Communications Design*, **2**, No. 3, p. 21 (1973).
- ⁴ P. Levine, "Measurement of CCD Transfer Efficiency by Use of Feedback to Increase the Effective Number of Transfers," *IEEE Solid-State Circuits*, **SC-8**, p. 104 (1973).
- ⁵ L. Walsh and R. H. Dyck, "A New Charge-Coupled Area Imaging Device," *CCD Applications Conf. Proc. TD-274*, p. 21; sponsored by the Naval Electronics Laboratory, San Diego, Calif., Sept. 1973.
- ⁶ S. P. Emmons and D. D. Buss, "Techniques for Introducing Low Noise Fat Zero in CCD's," (Abstract of paper presented at Solid State Device Research Conf., June 26-28, 1973, Denver, Colo.) *IEEE Trans. Electron Devices*, **ED-20**, p. 1172 (1973).
- ⁷ J. E. Carnes and W. F. Kosonocky, "Noise Sources in Charge-Coupled Devices," *RCA Review*, **33**, p. 327 (1972).
- ⁸ C. H. Séquin, "Interlacing on Charge-Coupled Devices," *IEEE Trans. Electron Devices*, **ED-20**, p. 535 (1973).

Low-Loss, Broadband Microwave Ultrasonic Delay Lines Using Ion-Beam-Milled Shear-Wave Transducers

David M. Stevenson* and J. J. Hanak

RCA Laboratories, Princeton, N.J. 08540

Abstract—Improved bonding and thinning techniques made it possible to use the optimum combination of delay crystal and transducer material in fabricating low-loss, broadband microwave acoustic delay lines operating up to 5 GHz. The delay line consisted of X-cut lithium niobate bonded by means of Cr-Au-In-Au-Cr film sandwich to magnesium aluminate spinel. Proper processing, including ion-beam milling, has resulted in lithium niobate shear-wave transducers with near bulk coupling coefficients. These results have laid the basis for subsequent development of transducers operating up to 11 GHz.

1. Introduction

For signal processing in microwave radar systems, it is desirable to realize the small size of microwave acoustic delay lines without sacrificing the low loss and large bandwidth of electromagnetic delay lines. To achieve the best possible performance from acoustic delay lines, it is necessary to use the optimum combination of delay crystal and transducer material.

Presently available microwave delay lines use sputtered ZnO transducers on longitudinal-wave-propagating sapphire. However, the lowest loss acoustic mode known is for shear waves propagating in the

* Presently with Varian Assoc., Salem Rd., Beverly, Mass. 01915.

(100) direction in magnesium aluminate spinel.^{1,2} YAG and YIG also have low-loss shear modes. Until now it has not been possible to use these low-loss shear-wave modes at high microwave frequencies because of the lack of efficient shear-wave transducers, although some success has been achieved using longitudinal-to-shear-wave conversion by reflecting from the proper crystal planes^{3,4} and at low microwave frequencies by using sputtered zinc oxide shear-wave transducers.^{5,6}

The greatest bandwidth is achieved by using transducer materials with the highest electromagnetic coupling coefficient, since this gives the lowest acoustic radiation Q . X-cut lithium niobate (LiNbO_3) generates shear waves, has low loss at microwave frequencies, and has the very high electromechanical coupling coefficient of 0.68 (compared with 0.2 to 0.25 for sputtered zinc oxide) and is therefore the most suitable material for use with shear-wave-propagating spinel or YAG.

Larson and Winslow⁷ have demonstrated the feasibility of bonding bulk X-cut lithium niobate transducers to shear-wave-propagating crystals and then thinning the transducer to obtain efficient operation up to 1 GHz.

In this paper we present the results of a program to develop improved bonding and thinning techniques for lithium niobate on spinel that has resulted in broadband, low-loss operation up to 5 GHz. We have used very thin (~ 6000 Å) Au-In-Au bonds, and have reduced the lithium niobate transducer thickness to less than 0.5 μm , using a combination of mechanical polishing and ion-beam milling.^{8,9} These thinned transducers exhibit bulk piezoelectric properties and are very efficient. We have achieved *two way* tuned insertion losses of 6.5 dB at 1.0 GHz, 10.5 dB at 1.8 GHz, 12.5 dB at 3.2 GHz, and 17 dB at 4.1 GHz for delays of 2 μs with impedance levels and Q 's that permit achieving octave bandwidths with only a small increase in total insertion loss.

2. Material Properties

Fig. 1 shows the acoustic loss (in dB/ μs) of several low-loss crystals propagating bulk modes at microwave frequencies. The lowest loss material known is magnesium aluminate spinel, which has a loss of 7.5 dB/ μs at 10 GHz for the shear mode in the (100) direction. Other low-loss materials are YAG and YIG, the low-loss mode being shear modes for these materials also. The attenuation of longitudinal waves in sapphire is greater than 20 dB/ μs at 10 GHz; thus spinel has

an advantage of 12.5 dB/ μ s at 10 GHz; this advantage increases to more than 30 dB/ μ s at 16 GHz.

The velocity of shear waves, V_s , is typically a factor of 1.5 to 2 less than that of longitudinal waves, V_f , in the same material (for an elas-

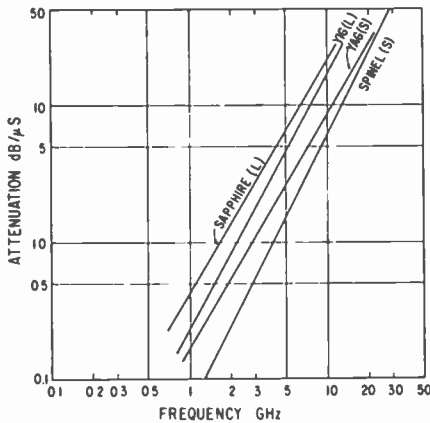


Fig. 1—Attenuation of low-loss acoustic material.

tically isotropic cubic crystal, the factor is theoretically $\sqrt{3} = 1.73$). This lower velocity produces two further advantages for shear-mode over longitudinal-mode operation: (1) for a given crystal length, longer delays can be obtained, and (2) for a given beam diameter, the diffraction loss is lower since it is proportional to V^2 . These advantages make it worthwhile to develop efficient shear-wave transducers even for low microwave frequencies when long delays are required.⁴

The input impedance and radiation Q of a transducer, which determine its loss-bandwidth capability, are determined by the electromechanical coupling coefficient, k ; the higher this coefficient, the greater the bandwidth capability. Fig. 2 shows the transducer material orientations and thicknesses required for several high electromechanical coupling coefficient materials for both longitudinal and shear waves. For shear-wave transducers, lithium niobate is the best material to use, both for its high coupling coefficient and for its relatively high sound velocity, which determines the transducer thickness for a given frequency.

Very high quality lithium niobate is now available commercially. By subjecting this material to proper processing, so that it is free

from any work damage, it was hoped that bulk properties could be maintained even for the very thin layers required for microwave acoustic transducers. Referring to Fig. 2, the transducer thickness for shear wave generation by X-cut lithium niobate is $2.4 \mu\text{m}$ at 1 GHz and only $0.24 \mu\text{m}$ at 10 GHz.

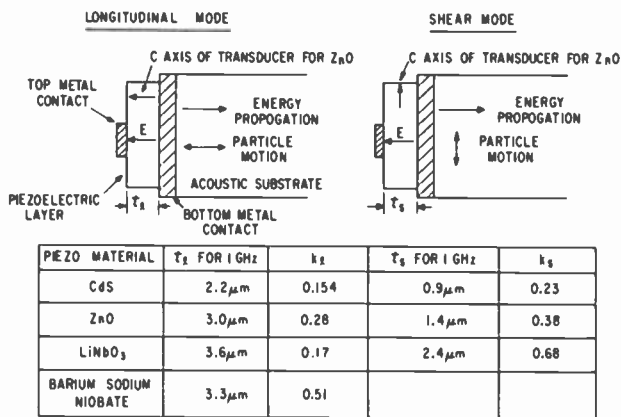


Fig. 2—Transducer geometries and materials parameters.

A more thorough comparison of the relative merits of lithium niobate with other transducer materials for microwave delay lines is presented in the Appendix.

3. Device Fabrication

Materials chosen for the device fabrication were standard optical grade X-cut lithium niobate obtained from a commercial supplier,* and spinel grown at RCA Laboratories¹ and cut with the (100) axis oriented normal to the plane of the transducer crystal. Prior to processing, the LiNbO_3 wafer was 0.025 cm thick and 0.5×0.5 cm in area. The spinel crystal was 0.95 cm thick and had the same area. It was lapped and polished mechanically flat and parallel on the opposite ends. The LiNbO_3 crystal was also lapped parallel mechanically to a thickness of 0.018 cm but then a chemical-mechanical method was used to polish the surfaces to be bonded to the spinel. This pol-

* Crystal Technology, Inc., 2510 Old Middlefield Way, Mountainview, Calif. 94040.

ishing, which removes only about 0.001 cm of the material, leaves the bottom surface completely free of scratches and surface damage, as shown by scanning electron microscopy.

After polishing, several different metal layers were deposited by evaporation onto the damage-free surface of the wafer and one surface of the spinel crystal; first chromium (200 to 300 Å), then gold (1000 to 2000 Å), and finally indium (1000 to 2000 Å). Indium was evaporated in the same vacuum system where bonding took place, so as not to oxidize its surface. Then, without breaking vacuum, the wafer and crystal are placed in a pressure device capable of exerting a pressure of 1000 to 2000 kg/cm², in which range a good indium-to-indium bond can be obtained at room temperature. After the bonding, the LiNbO₃ wafer is ready for thinning.

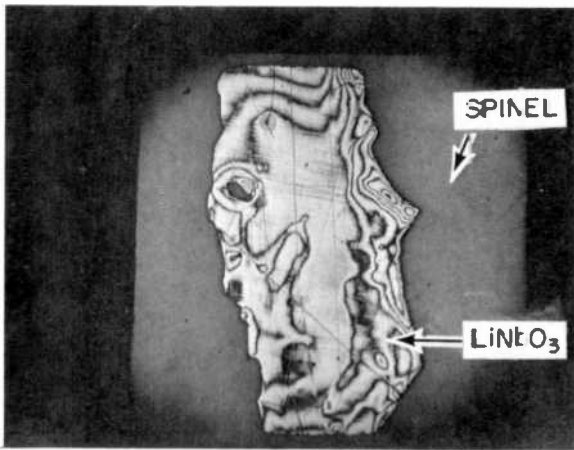
In the first stage of thinning, the wafer thickness was reduced by mechanical lapping from 0.018 cm to as little as 7 μm by using consecutively finer polishing powders. The second stage of thinning involved an ion-beam milling method. This method consists of letting an argon ion beam accelerated to several thousand volts impinge on the wafer surface at an oblique angle of incidence, thereby removing the surface atoms of the wafer via sputtering at a steady controlled rate. The ion-milling machine* used had a beam diameter of 1.27 cm. The accelerating dc voltage used was 6000 to 7000 V and the beam current ranged from 40 to 120 mA. The angle of incidence between the beam and the wafer surface ranged between 7° and 15°. Under these conditions, removal rates ranged from a few tenths to 1.5 μm/hr. Normally, higher etch rates were used in the beginning of the ion-beam thinning and lower rates in the final stages of thinning. The thickness of the wafer was checked periodically by optical interferometry.

As the ion density of the beam peaks near the center, the thinning was not uniform. Typically, the final wafer thickness near the edges was about 10% greater than near the center.

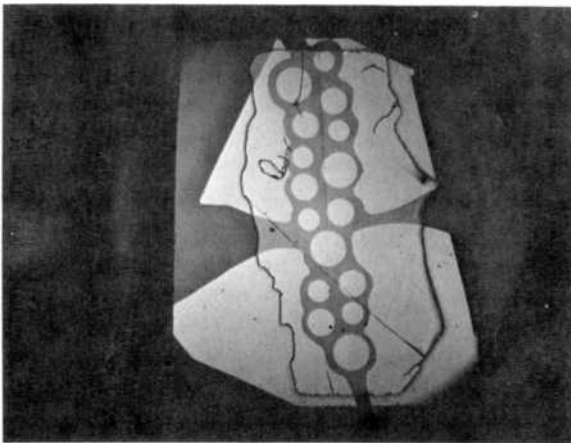
During the ion milling process the exact thickness of the transducer could be determined by viewing the transducer under polarized sodium light. Lithium niobate is birefringent and the fringe patterns formed under orthogonal polarizations were used to determine the thickness of the crystal to within ± 0.05 μm. Fig. 3(a) shows a photograph of a transducer with the fringe pattern formed with sodium light clearly visible. This lithium niobate transducer was thinned to 0.55 μm, corresponding to a half-wavelength resonance frequency of 4.3 GHz.

* Alba ion bombardment machine, Alba Engineers, Asnieres, France.

Scanning electron micrographs of the ion-beam-milled surface of LiNbO_3 wafers, processed as described, showed no evidence of damage extending from the bonded surface. Similar micrographs made of samples for which the bonded surface had been only mechanically lapped and polished, showed the ion-beam-milled surface resembling an orange peel—an evidence of underlying damage. This damage ex-



(a)



(b)

Fig. 3—(a) Interference photograph of LiNbO_3 transducer on $\langle 100 \rangle$ oriented spinel after ion-beam milling (thickness in central area is $2.2 \mu\text{m}$) and (b) Transducer shown in Fig. 3(a) with evaporated Au top electrode pattern.

tended from the mechanically lapped bonded surface to as much as $10\ \mu\text{m}$ into the crystal.

4. Insertion Loss Measurements

A top electrode for the transducer was made by evaporating a number of dots onto each of the thinned crystals. A typical top dot pattern is shown in the photograph of Fig. 3(b). The delay line parameters were measured in the microstrip test fixture shown in Fig. 4. A

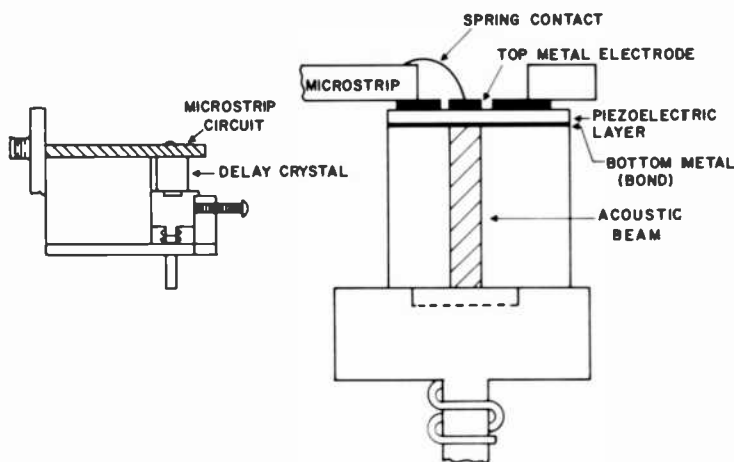


Fig. 4—Acoustic-delay-line test fixture.

spring contact connects the 50-ohm line on ceramic to each of the top electrode dots in turn. The ground plane of the microstrip shorts together all the top electrodes except the one being tested. Coupling to the bottom electrode is capacitive, through the high dielectric constant of the transducer; the exposed bottom electrode was removed during ion milling. This capacitive coupling, of course, excites acoustic waves in the lithium niobate, that is, under the ground plane, but these waves are weak and result in an additional loss of less than 1 dB.

Measurements of the performance of the delay lines were made using two techniques. The first of these was the standard pulse echo technique, which gives the round trip loss quite directly. The input impedance of the delay line could be determined by using a tuner to match in the input signal and then measuring the impedance of the

tuner on a network analyzer. However, this information can be obtained much more rapidly by using the network analyzer directly, in a modification of a method presented by Rupprecht and Steinberg.¹⁰ When the delay line is connected directly to the network analyzer

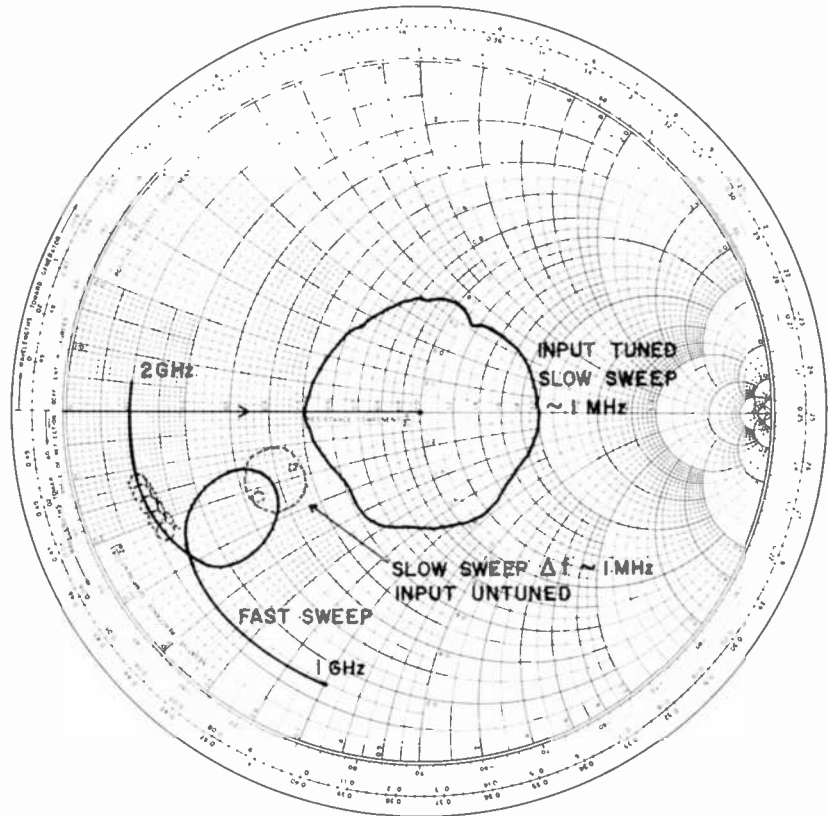


Fig. 5—Acoustic delay line measured using polar display of network analyzer.

and the frequency swept slowly, the input impedance display on the Smith chart is a series of overlapping circles, as shown in Fig. 5. The circles result from the rapidly changing phase of the echoes in the crystal. A line drawn through the circles gives the input impedance of the delay line. This input impedance can be observed directly by frequency modulating the input signal at a high enough rate that the re-

flected signal is outside the i-f band of the analyzer, which locks into the input frequency; the network analyzer therefore "sees" only the input impedance, since the internal reflections are eliminated.

A simple model for the delay line is shown in Fig. 6. The input im-

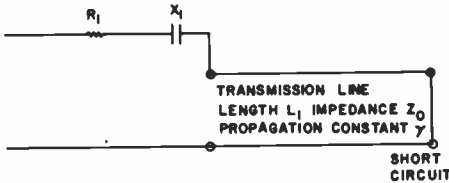


Fig. 6—Simple model of delay line.

pedance Z_{in} is given by

$$Z_{in} = R_1 + jX_1 + Z_0 \tanh(\gamma L_1). \quad [1]$$

R_1 arises from dissipative losses in the circuit and transducer electrodes. X_1 can be determined directly from the network analyzer display. By putting a tuner before the delay line, one of the circles can be brought approximately to the center of the Smith chart and placed symmetrically about the real axis. The input impedance Z'_{in} is then given by

$$Z'_{in} = KZ_{in} - jKX_1. \quad [2]$$

Standard transmission line analysis then permits the separate determination of R_1 , X_1 , Z_0 and γ from which the total round-trip loss can be determined and separated into components due to R_1 and the real part of γ . The input impedance can also be fully characterized and the contributions due to losses (R_1) and acoustic radiation separated. When account is taken of the impedance changes due to the detuning effect of the metal electrodes using the modeling technique presented by Reeder and Winslow,¹¹ a fairly accurate determination of the electromechanical coupling coefficient K_1 can be made.

The crystals were thinned in a series of ion-milling operations and r-f measurements performed after each stage. A series of measurements from UHF to low C-band frequencies for the same transducer/delay crystal combination were thus obtained.

Fig. 7 shows the tuned round-trip insertion loss of the delay line measured from 200 MHz to 4.5 GHz. The transducer was 2.2 μm thick, corresponding to a resonance of 1.1 GHz, but this was tuned down to 830 MHz by the top gold electrode, which was 1500 \AA thick.

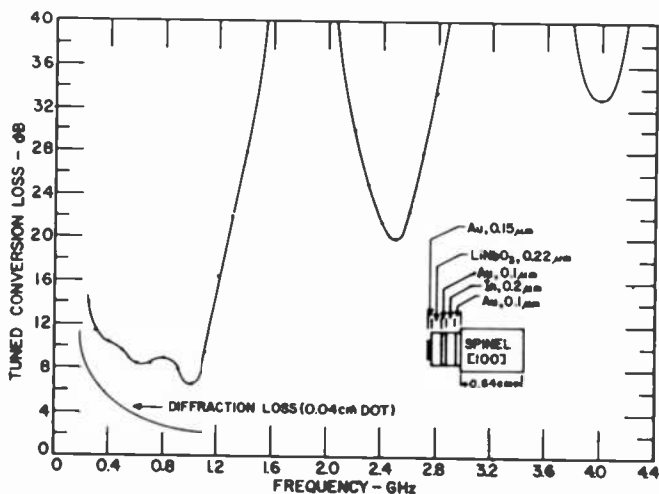


Fig. 7—Tuned round-trip insertion loss of X-cut LiNbO_3 on spinel delay line; delay time 2 μsec , transducer thickness 2.2 μm .

The two-way insertion loss has a minimum of only 6.5 dB at 1 GHz. The calculated diffraction loss at 1 GHz is 2.5 dB and the propagation loss through the indium is probably 1 to 2 dB (for two transits). If we include the losses in the tuner and input circuit, we conclude that the one-way conversion loss of the transducer can be no more than 1 dB, easily the best result that has ever been achieved with bonded transducers at this frequency.

The input impedance of the transducer is consistent with a value of coupling coefficient equal to the bulk value, showing that the process of ion-beam milling does not degrade the transducer efficiency.

In the next ion-milling step, the transducer was thinned from 2.2 to 1.2 μm , corresponding to a half wavelength center frequency of 2.0 GHz, which is reduced to 1.8 GHz by the aluminum top dot electrode. The excellent performance obtained in the 1 to 2 GHz band is shown in Fig. 8. The tuned two-way loss for 2 μs delay is less than 11 dB over much of the band and only 14 dB at the band edges.

The measured real part of the input impedance of the transducer is also shown in Fig. 8. Because of the high coupling coefficient of lithium niobate, the radiation Q of the transducer is low, and the real part of the impedance varies by only a factor of two over the octave band.

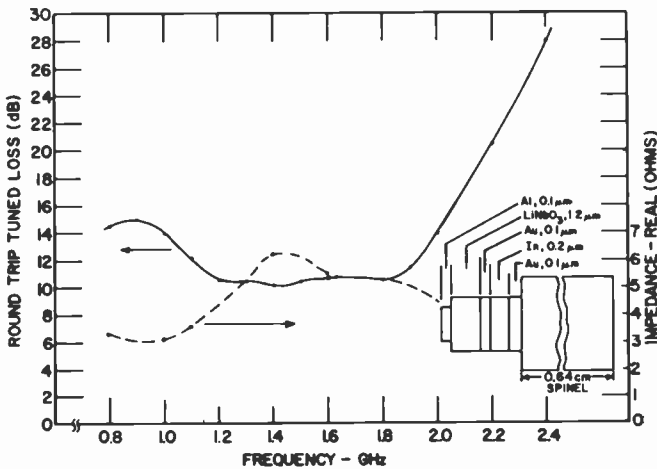


Fig. 8—Tuned round-trip loss and input impedance of LiNbO_3 on spinel delay line; delay time $2 \mu\text{sec}$, transducer thickness $1.2 \mu\text{m}$.

This permits the design of a low-loss, broadband matching circuit, as predicted by theory for high coupling coefficient piezoelectric materials. A circuit could readily be designed to give a round trip conversion loss of less than 17 dB over the entire octave bandwidth.

Further thinning of the transducer resulted in two thicknesses, since we ion milled the aluminum top dots to remove them. The transducer thickness was $0.65 \mu\text{m}$ where the aluminum had been and $0.55 \mu\text{m}$ where there had been no aluminum. A new aluminum top dot pattern was evaporated to include transducers of each thickness. The resulting tuned round-trip conversion loss for two of these transducers is shown in Figs. 9 and 10. For the $0.65\text{-}\mu\text{m}$ transducer, the loss had a minimum of 12.5 dB at 3.2 GHz and was less than 20 dB over most of S-band. The $0.55\text{-}\mu\text{m}$ transducer had 17 dB round-trip loss at 4.1 GHz.

These new results demonstrate the low-loss, broadband capability of bonded high coupling coefficient materials that cannot be achieved with sputtered zinc oxide films.

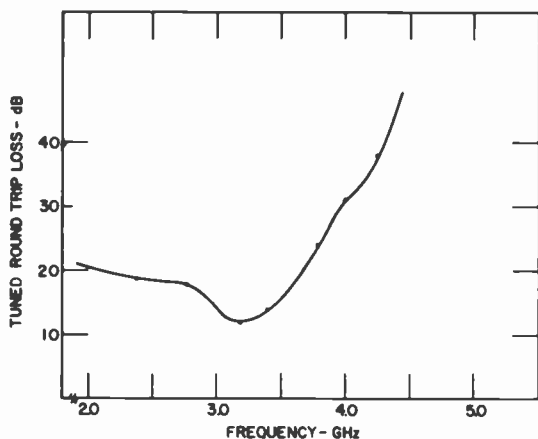


Fig. 9—Tuned round-trip loss in S-band of LiNbO_3 on spinel shear-wave delay line; delay time $2 \mu\text{sec}$, transducer thickness $0.65 \mu\text{m}$.

It should be noted that although indium was used in the bond, the observed transducer losses are less than expected based on the attenuation of indium as determined by Larsen and Winslow.⁷ Also, we did not observe the band-stop characteristics expected as a result of the low acoustic impedance of the indium. In retrospect, we believe that this is due to diffusion of indium into the gold during the ion milling.

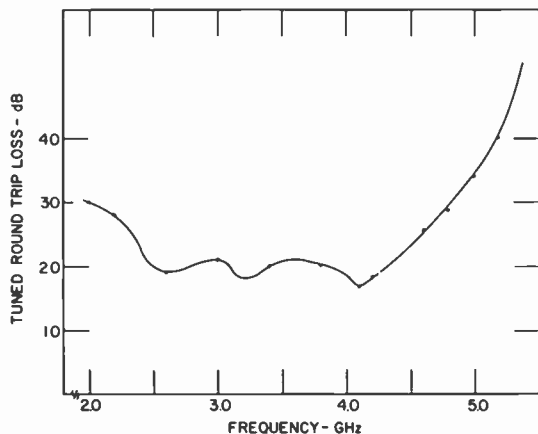


Fig. 10—Tuned round-trip loss in S-band of LiNbO_3 on spinel shear-wave delay line; delay time $2 \mu\text{sec}$, transducer thickness $0.55 \mu\text{m}$.

The ion milling jig was not well heat-sunked, and temperatures of 100° to 200°C were probably maintained for about 10 hours of milling time. This would permit the formation of brittle Au-In compounds, which probably have lower loss and considerably higher acoustic impedance than pure indium, thus accounting for the observed results.

This demonstration of the feasibility of fabricating low-loss delay lines up to 5 GHz has laid the basis for continued effort to extend the frequency range of these devices. By the use of the thinning techniques described above and improved bonding techniques, lithium niobate transducers having thicknesses as low as 0.25 μm have been fabricated that had a useful operating range of up to 11 GHz, as reported by Huang et al.¹²

5. Conclusions

Improved metal-bonding and crystal-thinning techniques have been applied to the fabrication of microwave acoustic delay line transducers. These techniques permit using the optimum combination of delay crystal and transducer material and have resulted in low-loss broadband delay lines operating up to 5 GHz. Proper processing of the transducer has resulted in lithium niobate shear-wave transducers with near bulk coupling coefficients. These results have laid the basis for subsequent development of transducers operating up to 11 GHz.

Acknowledgments

The authors wish to acknowledge the assistance of H. E. Temple in growing the spinel crystals; B. J. Seabury, G. W. Leck, and C. G. Bjorling for their valuable help in device processing; and J. S. O'Brien for his assistance in physical measurements. The authors are also grateful to E. F. Belohoubek and J. Collard for constructive discussions.

Appendix—Losses in Delay Lines

A delay line consists of two transducers separated by a delay medium. The total loss consists of two transducer conversion losses ($2 \times \text{TCL}$), two bond losses ($2 \times \text{BL}$), two transducer reflection losses ($2 \times \text{TRL}$), the loss in the material (ML), and the diffraction loss (DL). Thus the delay line loss (DLL) is given by

$$\text{DLL} = (2 \times \text{TCL}) + (2 \times \text{BL}) + (2 \times \text{TRL}) + (\text{ML}) + (\text{DL})$$

Each of these loss mechanisms is discussed here to show how the figures of Table 1 were deduced.

Material Loss

The attenuation of stoichiometric magnesium aluminate spinel has been measured to be about 7.5 dB/ μ s at 10 GHz for shear waves in the $\langle 100 \rangle$ direction at room temperature, and about 20 dB/ μ s for longitudinal waves propagating along the C-axis of sapphire. These values can be extrapolated to 16 GHz through the f^2 dependence of attenuation on frequency.

Transducer Reflection Losses

For a transducer with thin electrodes, the radiation Q of the transducer, Q_r , at the resonance frequency f_c , for which the transducer is one-half wavelength thick, is given by

$$Q_r = \frac{1}{\omega_0 C_0 R_a} = \frac{\pi r_D}{4k^2}$$

Here C_0 is the clamped capacitance of the transducer and R_a is the radiation resistance at f_c . The quantity r_D is the ratio of the acoustic impedance ρv of the transducer to that of the delay medium; r_D is

Table 1—Bulk Piezoelectric Properties of ZnO and LiNbO₃

Material	Cut	Mode	k	V (10^3 m/s)	Z_0 (10^6 kg/s/m ²)	Q_r $r_D = 1$
ZnO sputtered	Z	Long	0.22	6.33	36.0	16
ZnO bulk	Z	Long	0.28	6.33	36.0	10
	Z	Shear	0.32	2.72	15.5	8
LiNbO ₃ bulk	Z	Long	0.17	7.33	34.0	27
	Y(35°)	Long	0.50	7.40	35.0	3
	X	Shear	0.68	4.80	22.6	1.7

near unity for well-matched materials. The electromechanical coupling coefficient is k . Thus $Q_r \sim 1/k^2$. Table 1 shows the bulk piezoelectric properties of ZnO and LiNbO₃ for various orientations. Also shown are the typical values for sputtered ZnO. From Table 1 it can

be seen that Q_r is 1.7 for bulk LiNbO_3 X-cut to generate shear waves, and about 16 for sputtered ZnO oriented for longitudinal wave generation. Thus the input impedance is complex and typically highly reactive.

It is well known that to have constant input power to a complex load it is necessary to suffer reflection losses, and that for a given bandwidth these losses increase with increasing Q . This is expressed through the relationship

$$\int_{\omega_0}^{\omega_0 + \Delta\omega} \ln \left| \frac{1}{\Gamma} \right| d\omega = \frac{\pi}{RC}$$

where Γ is the reflection coefficient at frequency ω . Over an octave bandwidth, the reflection losses are approximately 4 dB less for a Q of 1.7 (LiNbO_3) than for a Q of 16 (sputtered ZnO). Since this reflection loss occurs at both input and output, the advantage for LiNbO_3 is approximately 8 dB.

Diffraction Losses

The acoustic beam radiated by the transducer spreads due to diffraction. In general, the propagating medium is anisotropic and the diffraction loss is direction dependent. Since no theoretical calculations are available for shear waves in anisotropic media, we will use the isotropic approximation, which gives

$$\alpha \sim \frac{\lambda_s}{a^2}$$

where α is the loss in dB/cm, λ_s is the acoustic wavelength in the delay medium, and a is the radius of the transducer.

The loss/ μs , α' , is given by

$$\alpha' = \frac{V_{sm}^2}{a^2 f}$$

where V_{sm} is the second velocity in the delay medium. From this equation we see that DL increases with V_{sm}^2 , thus the low velocity of shear waves compared with longitudinal waves reduces the diffraction loss.

The attenuation α' can also be expressed in terms of the transducer electrical characteristics in the form

$$\alpha' = V_{st}^2 R_a \left\{ \frac{\epsilon^s}{k^2 V_{st}} \right\} r_D (\pi^3 \epsilon_0) \left(\frac{f_c^2}{f} \right);$$

here V_{st} is the velocity of sound in the transducer and ϵ^s is the clamped dielectric constant of the transducer. The quantity $M_D = k^2 V_{st} / \epsilon^s$ can be considered a figure of merit for the transducer in terms of diffraction loss. For sputtered ZnO, $M_D = 3.4 \times 10^3$ cm/sec and for bulk LiNbO₃, $M_D = 5.0 \times 10^3$ cm/sec. Thus in terms of this figure of merit, LiNbO₃ is somewhat better than ZnO. At the resonance frequency $f = f_c$, we get

$$\alpha' = 0.24 R_{afc} \text{ dB}/\mu\text{s for LiNbO}_3 \text{ on spinel,}$$

$$\alpha' = 1.20 R_{afc} \text{ dB}/\mu\text{s for ZnO on sapphire,}$$

where f_c is in GHz. Thus for a given delay time and diffraction loss, the input impedance of the LiNbO₃ transducer can be five times greater than that of the ZnO transducer.

In any delay line design, a compromise must be made between diffraction loss and input impedance. A low input impedance is undesirable because the matching circuit losses become too great.

Transducer Conversion Losses

The transducer forms a capacitor with a resistive component due to acoustic radiation, dielectric losses and electrode resistive losses. The total Q , Q_{tot} of the input is given by

$$\frac{1}{Q_{tot}} = \frac{1}{Q_r} + \frac{1}{Q_D} + \frac{1}{Q_M}$$

where Q_r is the radiation Q ; Q_D is the dielectric Q , and Q_M the electrode Q . For the transducer to have small losses, it is necessary that $Q_D \gg Q_r$ and $Q_M \gg Q_r$.

It should be noted here that Q_r is about ten times greater for sputtered zinc oxide than for lithium niobate, so it is very much easier to meet these conditions for lithium niobate than for zinc oxide.

Q_D depends on the condition of the transducer material, which for very thin films (0.1 to 0.2 μm) should be better for thinned bulk material than for sputtered films. Q_M depends on the resistance of the metal electrodes, which, being of necessity very much less than one skin depth thick at high frequencies, contribute a significant effect. Ideally, the top electrode would be spaced a few \AA from the transducer; then it could be thick and of low loss without detuning the trans-

ducer at all. In practice, the top electrode must be in contact with the transducer and much thinner than the transducer to minimize frequency loading. These considerations hold equally for ZnO and LiNbO₃, for which Q_M is of the same magnitude. The net result is that, because of the higher Q_r of LiNbO₃, it should be possible to achieve much lower conversion loss than for zinc oxide.

Metal Bond Losses

The losses of metal bonds at high microwave frequencies are not known. The relatively high loss of indium at low microwave frequencies (probably in the range of 2 to 8 dB/ μ m at 1 GHz) means that it cannot be used at high microwave frequency bands. Also, indium is a poor acoustic match to both LiNbO₃ and spinel and this gives rise to pass bands and stop bands.

Gold has low loss at low microwave frequencies (~ 0.1 dB/ μ m at 1 GHz) and matches both LiNbO₃ and spinel well. The attenuation of gold for shear waves at high frequencies is not known, but at the very worst should be no more than 10 dB/ μ s at 10 GHz. With thin bonds (less than 0.2 μ m), it should be possible to achieve acceptable bond losses.

References:

- ¹ M. F. Lewis and E. Patterson, "Microwave Phonon Attenuation in Magnesium Aluminate Spinel," *J. Appl. Phys.*, **39**, No. 7, p. 3420, June 1968.
- ² M. F. Lewis, "Recent Developments in Microwave Ultrasonics," *Ultrasonics*, **8**, p. 24, June 1970.
- ³ A. B. Smith, "C-band Ultrasonic Delay Line Using Mode Conversion in YAG," *IEEE Trans. MIT*, **18**, p. 733, Oct. 1970 (Letter).
- ⁴ M. F. Lewis, "22 μ s S-Band Delay Line," *Electronics Letters*, **8**, No. 5, p. 131, March 1972.
- ⁵ N. F. Foster, "Performance of Shear Mode Zinc Oxide Thin Film Ultrasonic Transducers," *J. Appl. Phys.* **40**, No. 10, p. 4202, Sept. 1969.
- ⁶ H. W. Lehmann and R. Widmer, "RF Sputtering of ZnO Sheer-Wave Transducers," *J. Applied Phys.*, **40**, p. 3868 (1973).
- ⁷ J. D. Larson and K. K. Winslow, "Ultrasonically Welded Piezoelectric Transducers," *IEEE Trans. Sonics and Ultrasonics*, **SU-18**, No. 3, p. 142, July 1971.
- ⁸ D. Beecham, "Sputter Machining of Piezoelectric Transducers," *J. Applied Phys.*, **40**, p. 4357 (1969).
- ⁹ E. G. Spencer and P. H. Schmidt, "Ion Beam Techniques for Device Fabrication," *J. Vac. Sci. Tech.*, **8**, No. 5, p. S52, Oct. 1971.
- ¹⁰ G. Rupprecht and R. E. Steinberg, "Determination of Microwave Transducer and Delay Line Properties with a Modified Nodal Shift Method," *IEEE Trans.*, **MTT-17**, No. 11, p. 942, Nov. 1969.
- ¹¹ T. M. Reeder and D. K. Winslow, "Characteristics of Microwave Acoustic Transducers for Volume Wave Excitation," *IEEE Trans.*, **T-17**, No. 11, p. 927, Nov. 1969.
- ¹² H. C. Huang, J. D. Knox, Z. Turski, R. Wargo, and J. J. Hanak, "Fabrication of Sub-Micron LiNbO₃ Transducers for Microwave Delay Lines," *Appl. Phys. Letters* **24**, p. 109 (1974).

S-Band Trapatt Amplifiers with Four-Layer Diode Structures*

H. Kawamoto, S. G. Liu, H. J. Prager, and E. L. Allen, Jr.

RCA Laboratories, Princeton, N. J. 08540

Abstract—New four-layer ($n^+ - n - p - p^+$) diode structures have simultaneously achieved both large pulse width and broad bandwidth in a stagger-tuned Trapatt amplifier. The high impedance of the four-layer structures facilitates impedance matching over a broad frequency range, and the active region of the diode, because it is close to an integrated heat sink, exhibits low thermal resistance. A unique stagger-tuned second-harmonic extraction amplifier circuit consists of two one-quarter-wavelength open-circuited microstrip lines on one side of the diode with two rf-terminated branched microstrip lines on the other side. The four lines are of slightly different lengths (stagger-tuned) for broad-bandwidth operation. A four-layer diode has simultaneously achieved 50 μ s pulse width, 300 MHz bandwidth, 74 W output power, and 1% duty cycle in the stagger-tuned S-band amplifier. With different four-layer diodes, the S-band amplifier has demonstrated: (1) 120 μ s pulse width with 110 W power; (2) 380 MHz bandwidth with 75 W output power; and (3) 13 dB gain with 200 W output power.

1. Introduction

Trapatt diode amplifiers as used in phased-array radar systems require pulse widths of more than 50 μ s, instantaneous bandwidths broader than 300 MHz, and power levels of at least 50 watts. The large pulse width, broad bandwidth, and high power have, in the past,

* This work was supported in part concurrently by NAVORD and NAVSEC under Aegis Weapons Contract No. N00017-73-C-2404 and the Department of the Army under sub-contract to MIT Lincoln Laboratory, Contract No. F19628-70-C-0230, B-283.

been difficult to achieve simultaneously because the thermal characteristics have limited dissipation capability to power densities of about 100 kW/cm^2 . This limitation forces one to choose a diode diameter as large as 0.9 mm in order to obtain 150 watts of power. Such large diodes have low rf impedances, resulting in narrow instantaneous bandwidth. To achieve long pulse width with large bandwidth, a fundamental change has been made in both diode and circuit designs. New four-layer diodes, of both graded and abrupt types, have been developed for the S-band Trapatt amplifiers. Both types operate at broad bandwidth, since they have wide depletion-layer widths and, hence, present a high impedance to the circuit. Furthermore, they have excellent heat dissipation capabilities because their junctions are located close to a heat sink. A stagger-tuned, second-harmonic extraction circuit was employed to obtain broad instantaneous bandwidth.

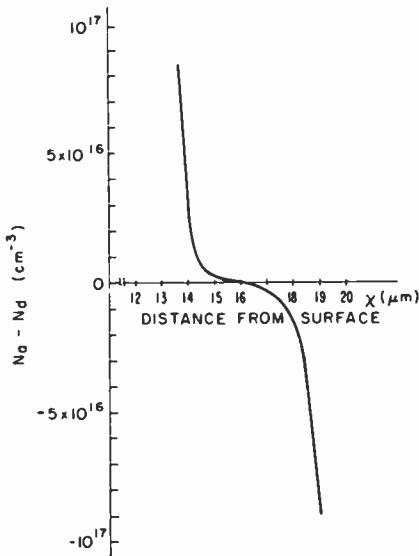


Fig. 1—Typical impurity profile of a diode fabricated with deep boron diffusion into $n\text{-}n^+$ epitaxial silicon with antimony-doped substrate.

2. Deep-Diffused Four-Layer Diode Structure

Diodes exhibiting the best rf performance have been fabricated from deep-diffused boron on $n\text{-}n^+$ epitaxial wafers with antimony substrate.¹ Fig. 1 shows a typical impurity profile of such deep-diffused

diodes measured by a two-point probe technique. In making the measurements, a diffused wafer is angle-lapped and the two-point probe is applied to measure the resistivity as a function of the depth of the diffused layer. The out-diffusion of antimony from the n^+ -substrate into the n -layer, in addition to the in-diffusion of boron from the surface, forms a graded p-n junction sandwiched between high-density p^+ and n^+ regions. This is referred to as a deep-diffused four-layer structure. Such a diode (JP180) has demonstrated excellent peak power and broad bandwidth characteristics, whereas n^+ - p - p^+ type three-layer diodes did not perform as well. Table 1 compares the am-

Table 1—Amplifier test results showing that large-size three-layer diodes consistent with low dissipation-power density exhibit narrow bandwidths, whereas a large-size four-layer diode demonstrates a broad band width.

	n ⁺ -p-p ⁺ Three-Layer Types		Deep-Diffused Four Layer JP180
	JP197	JP236	
Diameter (mm)	0.89	0.91	0.89
Depletion Layer Width (μm)	3.1	4.2	7.9
Transmission-Line Impedance Used in test (ohms)	12	12	12
Optimum Transmission Line Impedance (ohms)	3.2	6.2	12
Bandwidth (MHz)	120	90	300
Output Power (W)	100	100	157
Dissipation Power Density (kW/cm^2)	106	103	126
Pulse Width (μs)	50	50	1

plifier results for the two structures. The bandwidth of the deep-diffused diode is significantly greater, although the pulse width was limited to 1 μsec .

To understand the better operation of the deep-diffused diode, a computer simulation was carried out for the operation of a deep-diffused four-layer Trapatt diode.² The results of the simulation were in good agreement with experiments. The computer results show that the optimum depletion-layer width W in μm is expressed by $W = 12/f$

for the deep-diffused four-layer diodes, while $W = 7/f$ for the three-layer diodes, where f is the operational frequency in GHz (Fig. 2). For a given frequency, therefore, the depletion-layer width is approximately twice as great for the four-layer diode. The advantage of the deep-diffused four-layer structure is that the diode derives high

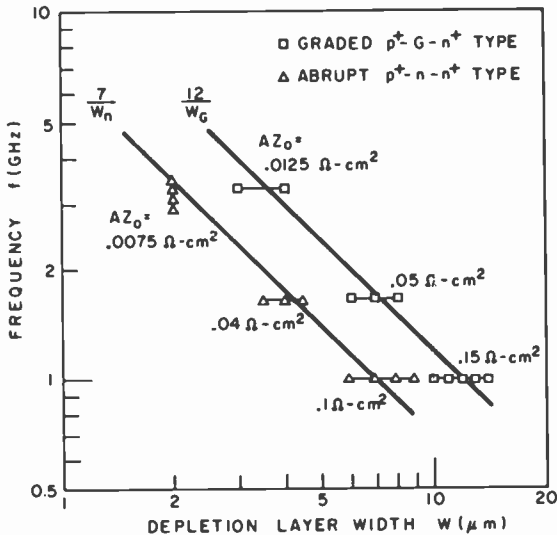


Fig. 2—Optimum depletion-layer width as a function of operational frequency.

peak-power output without the complexity of series-connected diodes,² since the larger depletion layer allows one to use a larger area while keeping the impedance level constant. The simulation in Ref. (2) was carried out with a diode placed on a transmission line. This revealed the effect of the transmission-line surge impedance on diode performance. For the best operating efficiency, the transmission-line surge impedance, Z_o , was found² to have an optimum value for a given diode depletion-layer width W and cross sectional area A . This occurs because the time constant in charging the diode capacitance ($\sim AZ_o/W$) must be of the order of the rise time of the rf signal ($1/f \sim W$); combining the two expressions leads to $AZ_o \sim W^2$ which agrees well with the results of simulations. Fig. 3 shows the optimum AZ_o product as a function of depletion-layer width for both the three-layer and the four-layer structures. The simulation at each depletion-layer width was carried out at a frequency defined by the relationship

in Fig. 2. Included in Fig. 3 are experimental points, which are in reasonable agreement with the simulation.

Table 1 shows how the four-layer diode improves the bandwidth while maintaining the low dissipation power density necessary for

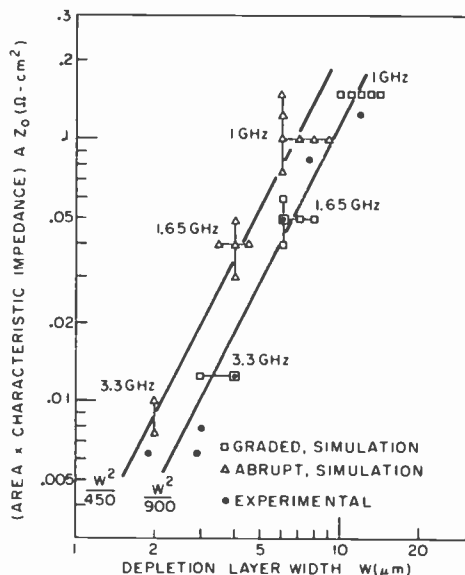


Fig. 3—Comparison of optimum AZ_0 for graded- and abrupt-junction diodes as a function of depletion-layer width and frequency.

50- μ s operation. To achieve a high output power, Trapatt diodes were operated at a dissipation power density as high as 250 kW/cm², resulting in a pulse width of less than 1 μ s. To extend the pulse width to 50 μ s, the thermal requirements limit the dissipation density to about 100 kW/cm² for large circular diodes. A diode size as large as 0.9 mm in diameter was chosen to meet these requirements. For the conventional JP197 three-layer diode having a 3.1- μ m depletion-layer width, the optimum transmission-line surge impedance is as low as 3 ohms according to Fig. 3. Even with a multiple-line, stagger-tuned circuit as described in Section 4, the surge impedance presented to the diode has a practical limit of 12 ohms, since unwanted transverse waves may be excited in wider microstrip transmission lines. The mismatching between diodes and circuits resulted in narrow amplifier bandwidths for the large-size three-layer diodes. On the other hand,

for the JP180 four-layer diode having 7.9- μm depletion-layer width, the optimum surge impedance is 12 ohms, which matches well with the circuit. This surge-impedance matching facilitated the circuit tuning, and a bandwidth as broad as 300 MHz resulted for the large-size four-layer diode.

3. Thermally Improved Four-Layer Diodes

The four-layer diode fabricated by the deep-diffusion process demonstrated peak-power and bandwidth capabilities; however, the pulse width was limited to 5 μs , although the dissipation power density was as low as 126 kW/cm². This is because the diode active region (graded p-n regions) is separated from the heat sink by the deep-diffusion length of 15 μm , resulting in poor heat-dissipating capability. Two techniques, double-diffusion and double-epitaxy, have been developed to improve the thermal characteristics of the four-layer diode. Both have an n⁺-n-p-p⁺ structure. The double-diffused diodes have graded n-p regions, whereas the double-epitaxy diodes have rather abrupt n-p junctions. Both techniques result in active regions close to the surface; thus the techniques of integral heat sinking and heat capacitor were found very effective in operating the diodes at large pulse width and high duty cycles.

3.1 Double-Diffusion Process

The double-diffusion process used to fabricate a graded four-layer diode consists of a moderately long-time, low-density phosphorus diffusion to form the graded junction, followed by a high-density phosphorus diffusion for a short time to provide a good ohmic contact. Fig. 4(a) shows a schematic impurity profile of the diode fabricated by the double-diffusion process. The finished diodes typically exhibited $V_B = 130$ V, $W_G = 5.4$ μm and $V_{\text{punch through}} = 35$ V. The double-diffused diodes have consistently operated in large-pulse-width conditions. This is because the substrate has been out-diffused during the first diffusion process, thus minimizing microplasma effects.¹

3.2 Double-Epitaxy Process

A double-epitaxy process was used to fabricate four-layer diodes with relatively abrupt junctions; these are referred to as double-ended diodes in Ref. (3). The diodes were made by diffusion of phosphorus into double-epitaxially grown n-p-p⁺ silicon wafers (Fig. 4b). The

doping densities of the n- and p- regions were of the order of 1 to $4 \times 10^{15} \text{ cm}^{-3}$, and the junction depth extended about $4 \mu\text{m}$ below the surface of the wafer. These values were monitored during epitaxial growth, and also checked within the accuracy of the two-point-probe spreading-resistance technique. From the C-V measurement of a representative diode, the capacitance and depletion width were determined to be 7 pF and $6 \mu\text{m}$, respectively. The voltage reached breakdown at 130 V . The slope of capacitance versus voltage on a log-log plot was 0.4 .

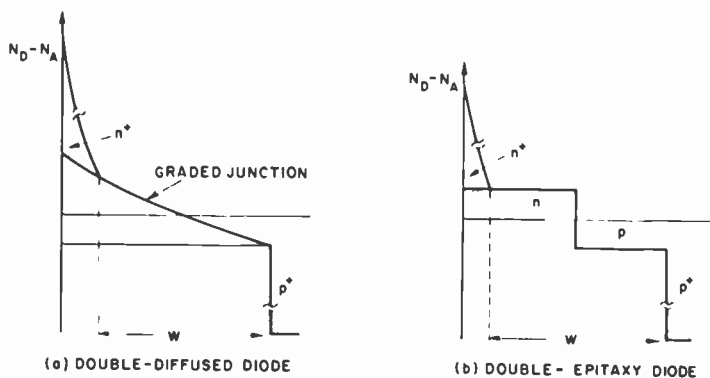


Fig. 4—Impurity profile of (a) graded four-layer diode fabricated by double-diffusion process and (b) abrupt four-layer diode fabricated by double-epitaxy process.

3.3 Integral Heat Sink and Heat Capacitor

The double-diffused and double-epitaxy diodes were made with an integral copper heat sink and a heat capacitor to achieve long-pulse-width operation. The integral copper heat sink was fabricated by electroplating a 0.2-mm -thick copper layer on the junction side of the metalized wafer. The adhesion of the electroplated copper to the metalized diode is better than can be obtained by a thermal compression method, thus providing a more reliable thermal contact.

To extend the heat sinking from the bottom to the top of the diode, i.e., the substrate side, a piece of copper measuring $1.5 \times 1.5 \times 0.5 \text{ mm}$ was soldered onto the top gold contact of the diodes, as shown in Fig. 5. The additional copper mass acts as a heat capacitor, temporarily absorbing heat transients and thus extending the permissible oper-

ational pulse width. A double-diffused JP258 diode assembled in this manner was capable of operating with a pulse width of 120 μs at a peak output power of 110 watts. Furthermore, the heat capacitor was

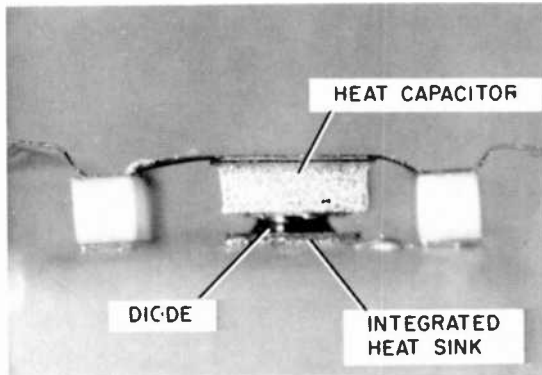


Fig. 5—A diode mounted with an integrated heat sink and a heat capacitor to improve thermal capabilities.

found especially effective in preventing diode burn-out during circuit tuning. We have often found that diodes burn out while dissipating only $\frac{1}{3}$ of their expected limit. This occurs when the circuit is being tuned for maximum pulse width or maximum bandwidth. With the heat capacitor on top of the diode, we have had fewer problems with diode burn-out during tuning; we were able to tune the amplifier circuits for broad bandwidth while the diodes were taking pulses as wide as 50 μs .

4. Stagger-Tuned, Second-Harmonic Microstrip Line Circuit

An S-band amplifier circuit in which a second-harmonic signal was extracted from the middle of a straight transmission line was previously described.⁴ This circuit has been modified into a stagger-tuned type to operate the diodes over a broader frequency range.

Fig. 6 shows the schematic diagram of the stagger-tuned second-harmonic extraction amplifier circuit fabricated on a Duroid substrate. The circuit consists of two one-quarter-wavelength open-circuited microstrip lines on one side of the diode with two rf terminated branched microstrip lines on the other side of the diode. Large

tuning plates, acting as rf shorts, are placed on each branch a quarter wavelength from the diode. The four microstrip lines determine in effect the frequency range of operation. The four lines are of slightly different lengths, resembling a stagger-tuned circuit for broad-bandwidth operation. The characteristic impedances of the four lines are

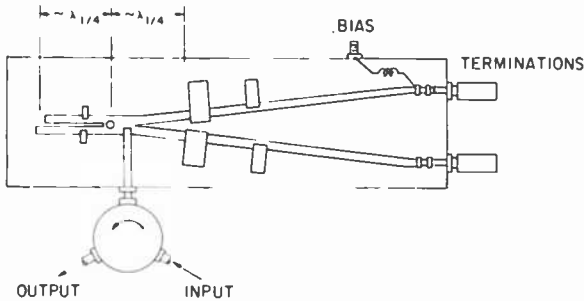


Fig. 6—Schematic of second-harmonic extraction amplifier circuit on Duroid substrate.

50, 50, 45 and 45 ohms; the four lines together present a 12-ohm surge impedance to the diode, and offer excellent surge-impedance matching to the 0.9-mm four-layer diode.

The input-output line to the circulator is coupled to a point between the diode and the tuning plate. A time-domain analysis has shown that the circuit at this point has a strong second-harmonic component with a relatively weak fundamental component.⁵ To verify this, the circuit was modified to accommodate microwave chip resistors for waveform measurements. Waveforms were measured with a 12-GHz sampling oscilloscope. Fig. 7b shows the waveform measured at the output terminal. This output waveform is sinusoidal and has a repetition rate of 320 ps, corresponding to the output frequency of 3.15 GHz. Fig. 7a shows the waveform at the diode as measured through a 1000-ohm microwave resistor connected to the diode. The diode waveform is similar to those generally observed in actual and computer-simulated performances of Trapatt diodes, an over voltage (negative-going) followed by a voltage drop (positive-going) representing the sequence leading to the trapped-plasma state. Note, however, that the repetition period is twice as long as the repetition period of the output signal. This indicates that both the input and output signals are second harmonics of the trapped-plasma occurrence.

Fig. 8 shows a miniaturized version of the stagger-tuned circuit. By folding the microstrip lines and using Johanson capacitors, the circuit

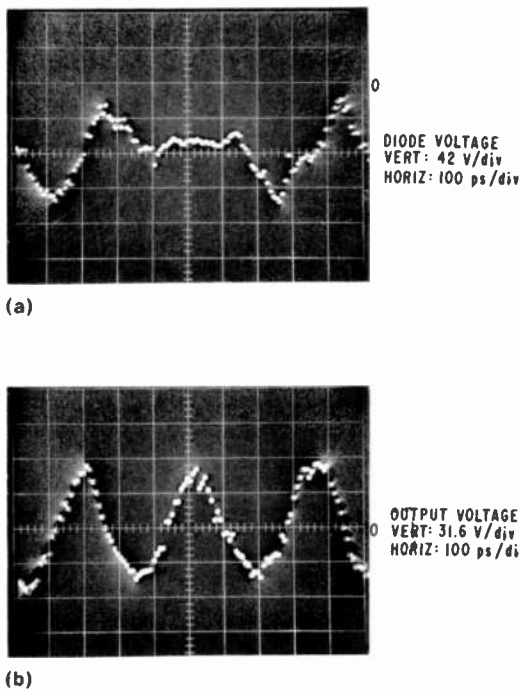


Fig. 7—RF voltage waveform at the diode (top) and the output terminal (bottom of the second-harmonic amplifier circuit).

area has been reduced by a factor of three. The miniaturized circuit has demonstrated the same results as those of the original circuit.

5. Amplifier Performance

All three types of four-layer diodes have been operated in the stagger-tuned amplifier circuit. Table 2 summarizes their performance.

A deep-diffused JP180 diode has demonstrated the highest output power—200 W at narrow bandwidth and 157 W at 300 MHz (3-dB output power variation) bandwidth. The depletion-layer width of the diode was $7.9 \mu\text{m}$ and the breakdown voltage was 150 V. The operation of this deep-diffused diode was limited to $5 \mu\text{s}$ pulse width because of the deep n^+ layer.

Fig. 9 exhibits the gain vs. frequency characteristic of the stagger-tuned second-harmonic amplifier. Included in Fig. 9 is phase shift vs. gain, an important parameter in phased-array-radar applications.

Table 2—Four-layer diodes tested in stagger-tuned second-harmonic amplifier circuit.

Diode Type	Peak Output Power (W)	Bandwidth (MHz) (Power Variation)	Maximum Gain (dB)	Maximum Efficiency (%)	Duty Cycle (%)	Pulse Width (μ s)
Deep-Diffused	JP 180 0.9 mm dia.	300 (3 dB)	8.7	16.9	0.01	1
	JP 180 0.9 mm dia.	narrow	13	13.2	0.01	1
Double Epitaxy	CD16 0.7 mm dia. heat capacitor	250 (4 dB)	5.9	16.4	1	50
	CD16 0.7 mm dia. heat capacitor	300 (2.6 dB)	4.4	15.4	0.2	50
	CD16 0.7 mm dia. heat capacitor	380 (4.3 dB)	4.4	16.3	0.2	10
Double-Diffused	KK 265 1 mm dia. ring package	300 (4 dB)	4.7	9.7	1	50
	JP 253 1 mm dia. heat capacitor	narrow	8.2	15.5	0.4	50
	JP 253 1.1 mm dia. heat capacitor	narrow	6.8	13.9	0.3	120

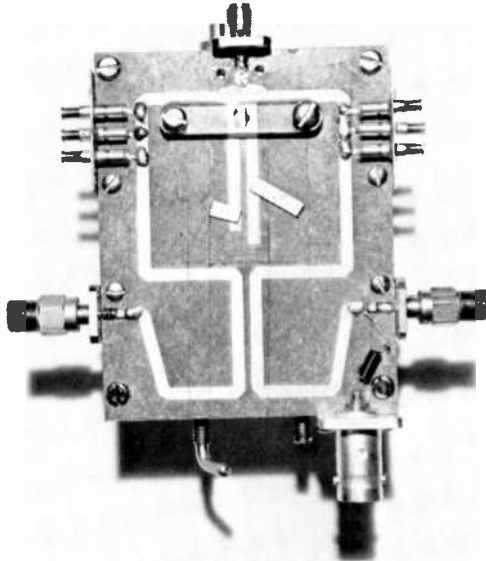


Fig. 8—A miniaturized stagger-tuned second-harmonic circuit.

The method used to make the measurements employs a straightforward phase bridge that makes use of a precision line stretcher. As can be seen, there is a linear phase shift with frequency. The rms phase deviation is 15.6° .

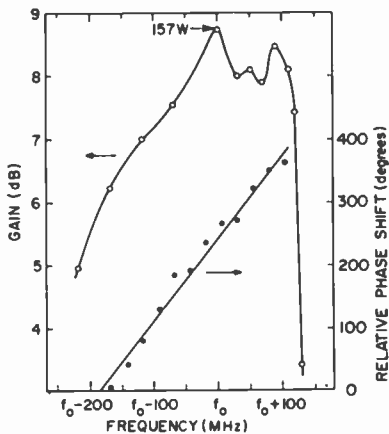


Fig. 9—Gain and relative phase shift of a stagger-tuned Trapatt amplifier.

The four-layer diodes fabricated by the double-epitaxy process were easily tuned for broad bandwidth. For example, a CD16 diode exhibited a 380 MHz (4.3 dB) bandwidth with 10 μ s pulse width. The CD16 diode had a depletion-layer width of 6 μ m and a breakdown voltage of 130 V. The oscilloscope waveforms in Fig. 10 demonstrate

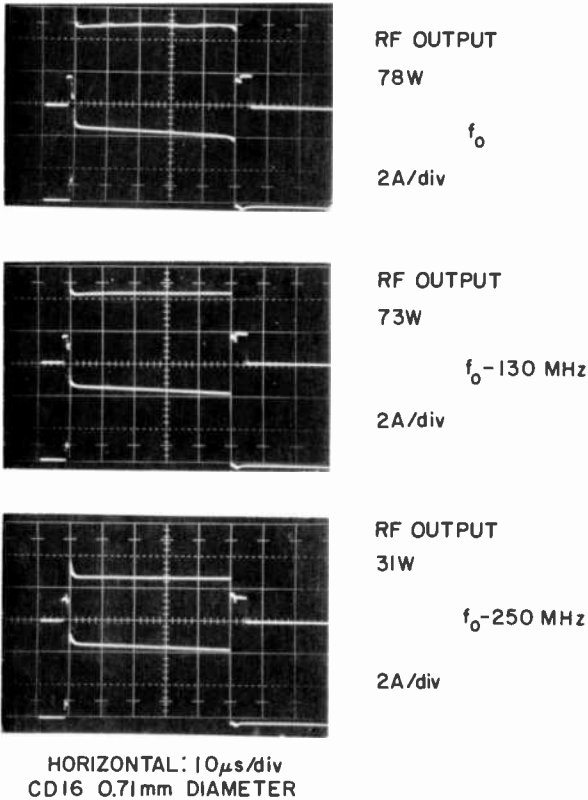


Fig. 10—Oscilloscope photographs showing that a stagger-tuned amplifier with a four-layer diode delivers noiseless 50 μ s wide output power over the frequency range of 250 MHz.

that the 50- μ s-wide rf-detected waveforms show no observable noise over the frequency range of 250 MHz.

The four-layer diodes fabricated by the double-diffusion process have consistently operated in wide-pulse conditions. A JP253 double-diffused diode exhibited 120 μ s pulse width at 110 W peak output power as shown in Fig. 11. A KK265 diode has achieved a 300-MHz

bandwidth with $50 \mu\text{s}$ pulse width and 1% duty cycle. The peak output power was 74 W with a peak power gain of 4.7 dB. The depletion-layer width of the KK265 diode was $5.4 \mu\text{m}$ and the breakdown voltage was 130 V.

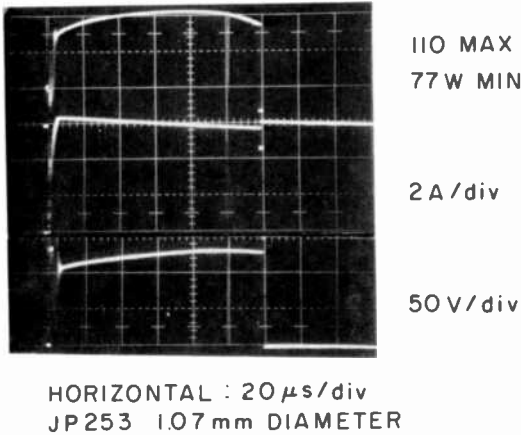


Fig. 11—Oscilloscope pictures showing that a graded four-layer diode is capable of operating with $120 \mu\text{s}$ pulse-width and 110 W peak output power.

6. Conclusions

Four-layer diodes fabricated by double-epitaxy and double-diffusion processes are capable of achieving both broad instantaneous bandwidth and large pulse width simultaneously. This comes about because the high impedance of the four-layer structures facilitates impedance matching over a broad frequency range, and the active n-p region fabricated close to the surface contributes to a low thermal resistance. Of the two types of four-layer diodes, the double-epitaxy diode was more easily tunable for broad bandwidth, whereas the double-diffused diode more consistently operated at long pulse width. The stagger-tuned second-harmonic circuits have operated with a variety of diodes, and demonstrated the best results for large pulse width and bandwidth combinations.

Acknowledgments

The authors are indebted to N. Klein for his contributions in wafer processing, device fabrication, and packaging; to J. Kaminski for his

aid in wafer processing; and to R. D'Aiello for the two-point probe measurements. They are grateful to L. S. Napoli and to F. Sterzer for their comments on the manuscript.

References:

¹ S. G. Liu and J. J. Risko, "Fabrication and Performance of Kilowatt L-Band Avalanche Diodes," *RCA Review*, **31**, p. 3, March 1970.

² H. Kawamoto, "P⁺-Graded Junction -N⁺ High Efficiency Avalanche (TRAPATT) Diode," Digest of the 1973 International Conf. on Solid-State Devices, Tokyo, Japan, also in Proc. of the Conf. Supplement to *J. of Japan Society of Applied Physics*, **43**, 1974, p. 246.

³ S. G. Liu, "Trapatt Diodes and Circuits for High-Power Microwave Generation," *Proc. Fourth Biennial Conf. on Microwave Semiconductor Devices, Circuits and Applications*, **4**, p. 359, Cornell University, Ithaca, New York, 1973.

⁴ K. K. N. Chang, H. Kawamoto, H. J. Prager, J. Reynolds, A. Rosen, and V. A. Mikenas, "High-Efficiency Avalanche Diodes (TRAPATT) for Phase-Array Radar Systems," Digest of 1973 IEEE International Solid-State Circuits Conf., p. 122, Phila., Pa., Feb. 1973.

⁵ H. Kawamoto, H. J. Prager, et al, "S-Band Avalanche Diode Amplifiers," Final Report to MIT Lincoln Laboratory, Contract No. 19628-70-C-0230, B-283, July, 1972.

An Introduction to the Science and Technology of Liquid Crystals—II

The next five papers in this issue comprise the second installment in a series of lectures on liquid crystals being published in *RCA Review*. This series grew out of a weekly study seminar conducted by members of the liquid-crystal activity at RCA Laboratories to stimulate increased interaction among individuals from different disciplines who share a common interest in liquid crystals. Thus, these papers are intended as a primer in the science and technology of liquid crystals for those using or contemplating the use of these devices.

A third, and final, group of papers in this series will appear in a future issue of *RCA Review*. Listed below are the first six papers, which appeared in the March 1974 issue of *RCA Review*:

- Liquid-Crystal Mesophases
E. B. Priestley
- Structure-Property Relationships in Thermotropic Organic Liquid Crystals
Aaron W. Levine
- Introduction to the Molecular Theory of Nematic Liquid Crystals
P. J. Wojtowicz
- Generalized Mean Field Theory of Nematic Liquid Crystals
P. J. Wojtowicz
- Hard Rod Model of the Nematic-Isotropic Phase Transition
Ping Sheng
- Nematic Order: The Long Range Orientational Distribution Function
E. B. Priestley

Introduction to the Molecular Theory of Smectic-A Liquid Crystals

Peter J. Wojtowicz

RCA Laboratories, Princeton, N. J. 08540

Abstract—The symmetry and structure of the smectic-A phase is reviewed and the order parameters identified. Several versions of the mean-field approximation to the theory are derived based on the Kobayashi-McMillan form of potential. Comparisons with experiment are made. The important question of the existence of second-order smectic-A to nematic phase transitions is examined.

1. Introduction

Contributions to the theory of smectic-A liquid crystals have been made by a number of investigators.¹⁻⁵ In all cases the treatments are an extension of the Maier-Saupe⁶ mean-field model of nematics examined in a previous paper.⁷ Here we essentially follow the development of McMillan.^{3,4}

The symmetry and structure of the smectic-A liquid crystals are reviewed; the natural order parameters are identified. The relationship of the smectic-A phase to the nematic (or cholesteric) and isotropic phases in homologous series is also examined. The McMillan form of the single molecule potential function is then deduced starting from the Kobayashi form of the potential^{1,2} and using the formal development presented earlier.⁸ The derivation of the statistical thermodynamics then follows, along with a presentation of McMillan's numerical results and a comparison with experiment. Improvements in the theory introduced by Lee et al⁵ are also considered. In the last section, the important question of whether the smectic-A to nematic (cholesteric) phase transition can ever be second order is examined.

2. Symmetry, Structure and Order Parameters

An examination of the optical properties of smectic-A liquid crystals shows that they have uniaxial symmetry. Just as in the nematic phase, the smectic-A phase has a unique axis (again called the director and denoted by \hat{n}) along which the elongated rod-like molecules tend to align. In addition, x-ray diffraction from smectic-A liquid crystals displays one sharp ring demonstrating that this phase possesses one-dimensional translational periodicity. The structure is depicted in Fig. 1. The centers of mass of the molecules tend to lie on planes perpendicular to the director. The spacing between planes, d , is approximately a molecular length. There is no ordering of the centers of mass of the molecules within the planes.

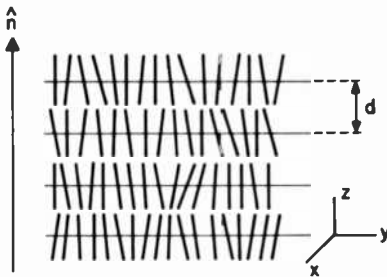


Fig. 1—Schematic representation of the structure of the smectic-A phase of liquid crystals.

As in the nematics, the orientational order of the molecules is described by the order parameter $\langle P_2(\cos\theta) \rangle$, where P_2 is the second-order Legendre polynomial, θ is the angle between the long axis of the molecule and the director, and $\langle \ \rangle$ denotes the average value. A simple phenomenological deduction of this orientational order parameter was presented in a previous paper.⁷ The identification of the order parameter required to describe the periodic layering of the molecules is not as straightforward, however. For the smectic-A structure we must examine the problem more formally.

In the case of nematics, Priestley⁹ has described how the orientational distribution function could be expanded in a series of even-order Legendre polynomials:

$$f(\cos\theta) = \sum_{L(\text{even})} \frac{2L+1}{2} \langle P_L(\cos\theta) \rangle \dot{P}_L(\cos\theta). \quad [1]$$

The traditional order parameter, $\langle P_2(\cos \theta) \rangle$ appears in the first non-trivial term in the series. Succeeding terms contain the average values of higher-order Legendre polynomials, which can be thought of as order parameters of higher degree. The $\langle P_L \rangle$ thus describe features of increasing subtlety in the orientational ordering, and many are clearly required to give a good account of the true orientational distribution function.

How can this formal treatment of the distribution function (and resulting order parameters) be generalized to include the smectic-A structure? We find the clue in Kirkwood's treatment^{10,11} of the melting of crystalline solids. In a crystal the density distribution function (the translational molecular distribution function) is periodic in three dimensions and can be expanded in a three-dimensional Fourier series. Kirkwood does this and then identifies the order parameters of the crystalline phase as the coefficients in the Fourier series. For simplicity let us consider a one-dimensionally periodic structure (such as the smectic-A but with the orientational order suppressed for the moment). The distribution function, which describes the tendency of the centers of mass of molecules to lie in layers perpendicular to the z -direction, can be expanded in a Fourier series:

$$f(z) = \sum_{n=0} \alpha_n \cos\left(\frac{2\pi n z}{d}\right), \quad [2]$$

$$\int_0^d f(z) dz = 1, \quad [3]$$

where d is the layer spacing and Eq. [3] expresses the normalization condition. Since the distribution is periodic we need only integrate over a single period. We now find the coefficients, α_n by multiplying both sides of Eq. [2] by $\cos(2\pi m z/d)$ and integrating:

$$\alpha_m = \frac{2}{d} \int_0^d \cos\left(\frac{2\pi m z}{d}\right) f(z) dz. \quad [4]$$

The integral on the right hand side is immediately recognized as the definition of the average value, so that

$$\alpha_m = \frac{2}{d} \left\langle \cos\left(\frac{2\pi m z}{d}\right) \right\rangle. \quad [5]$$

For the special case of $m = 0$, $\alpha_0 = 1/d$. Combining these results we obtain

$$f(z) = \frac{1}{d} + \frac{2}{d} \sum_{n=1} \left\langle \cos\left(\frac{2\pi n z}{d}\right) \right\rangle \cos\left(\frac{2\pi n z}{d}\right). \quad [6]$$

The coefficients in the series and hence the order parameters turn out to be the average values of the cosine functions of the series (in complete analogy to the situation in Eq. [1]). When the structure has perfect periodic order, all the $\langle \cos(2\pi n z/d) \rangle$ have the value unity; for the completely disordered system with all molecules randomly distributed in z , all $\langle \cos(2\pi n z/d) \rangle$ vanish. Again, many order parameters are required to make a good approximation to the distribution function, Eq. [6].

The smectic-A liquid crystals possess both orientational and translational order. The molecular distribution function must therefore describe both the tendency of the molecules to orient along \hat{n} and to form layers perpendicular to \hat{n} . The distribution function is thus a function of both $\cos\theta$ and z , and can be expanded in a double series:

$$f(\cos\theta, z) = \sum_{\substack{L=0 \\ (\text{even})}} \sum_{n=0} A_{L,n} P_L(\cos\theta) \cos\left(\frac{2\pi n z}{d}\right), \quad [7]$$

$$\int_{-1}^1 \int_0^d f(\cos\theta, z) dz d(\cos\theta) = 1. \quad [8]$$

The coefficients $A_{L,n}$ are found by multiplying both sides of Eq. [7] by $P_K(\cos\theta) \cos(2\pi m z/d)$, integrating and recognizing the definition of averages:

$$\langle X \rangle \equiv \int_{-1}^1 \int_0^d X f(\cos\theta, z) dz d(\cos\theta). \quad [9]$$

The results are

$$\begin{aligned} A_{m,0} &= 1/2d, \\ A_{0,n} &= \frac{1}{d} \left\langle \cos\left(\frac{2\pi n z}{d}\right) \right\rangle, (n \neq 0), \\ A_{L,0} &= \frac{2L+1}{2d} \langle P_L(\cos\theta) \rangle, (L \neq 0), \\ A_{L,n} &= \frac{2L+1}{2d} \left\langle P_L(\cos\theta) \cos\left(\frac{2\pi n z}{d}\right) \right\rangle, (L, n \neq 0). \end{aligned} \quad [10]$$

In addition to the purely orientational and translational order parameters, the $\langle P_L(\cos\theta) \rangle$ and $\langle \cos(2\pi n z/d) \rangle$, we find the set of mixed-order parameters, $\langle P_L(\cos\theta) \cos(2\pi n z/d) \rangle$. These describe the

correlation or coupling between the degrees of orientational and translational order. The three order parameters of lowest degree in Eq. [10] appear in all the published theories¹⁻⁵ of the smectic-A phase and have been given special symbols:

$$\begin{aligned}
 \eta &\equiv \langle P_2(\cos\theta) \rangle, \\
 \tau &\equiv \langle \cos(2\pi z/d) \rangle, \\
 \sigma &\equiv \langle P_2(\cos\theta) \cos(2\pi z/d) \rangle.
 \end{aligned}
 \tag{11}$$

In the isotropic phase, $\eta = \tau = \sigma = 0$; in the nematic phase, $\eta \neq 0$, $\tau = \sigma = 0$; in the smectic-A phase $\eta \neq 0$, $\tau \neq 0$, $\sigma \neq 0$. For perfect order all three tend to unity. Part of the task of molecular theory is, of course, to calculate the temperature dependence of these order parameters. Again we point out that although the three quantities of Eq. [11] are sufficient to parametrize simple mean field models, a good approximation to the true distribution function, $f(\cos\theta, z)$ requires many terms in Eq. [7].

3. Phase Diagrams

Of special interest to the molecular theory are the transition temperatures at which the various liquid-crystal phases transform into each other and into the isotropic fluid. The collection of such temperatures in homologous series can be conveniently summarized in phase diagrams such as those schematically depicted in Fig. 2. The phase diagram for the homologous series of 4-ethoxybenzal-4-amino-n-alkyl- α -methyl cinnamates is displayed in Fig. 2a. The regions of stability of the smectic-A, nematic and isotropic phases are shown. Fig. 2b depicts the phase diagram for the homologous series of the cholesteryl esters of saturated aliphatic acids. Here the regions of stability of the smectic-A, cholesteric, and isotropic phases are shown. For the present purpose we can treat the cholesteric phase as thermodynamically similar to the nematic; the terms in the free energy, which differentiate between cholesteric and nematic structures, are very small and may be neglected in this context. Three major features of these diagrams should be noted: (a) the nematic (cholesteric) to isotropic transition temperature $T_{NI}(T_{CI})$ decreases strongly with increasing chain length, (b) the smectic-A to nematic (cholesteric) transition temperature $T_{AN}(T_{AC})$ first increases with chain length, then stays constant or gently decreases, and (c) $T_{NI}(T_{CI})$ and $T_{AN}(T_{AC})$ are converging with increasing chain length, so that for sufficiently

long chains the smectic-A phase transforms directly into the isotropic fluid without passing through the nematic (cholesteric) phase.

Another experimental quantity of interest is the entropy of transition from smectic-A to nematic (cholesteric) structure. Just as in the

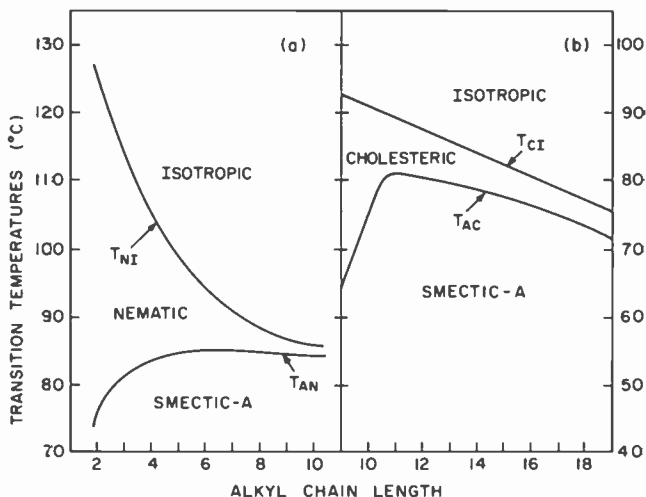


Fig. 2—(a) Schematic representation of the phase diagram of the homologous series of 4-ethoxybenzyl-4-amino-n-alkyl- α -methyl cinnamates (after Ref. [3], data of Ref. [12]). (b) Schematic representation of the phase diagram of the homologous series of cholesteryl esters of saturated aliphatic acids (after Ref. [3], data of Ref. [13]).

case of the nematic to isotropic transition, the entropy changes are very small, in keeping with the fact that only one degree of freedom of the molecules (translational motion in the z -direction) is being influenced at $T_{AN}(T_{AC})$. For both of the examples shown in Fig. 2 the transition entropies range from about 0.2 to 1.2 cal/° mole, being low for short chains and increasing with increasing chain length.^{12,13}

4. The Molecular Potential

The stability of the smectic-A structure is a direct consequence of the interactions between the constituent molecules. Even though we have virtually no detailed knowledge of their precise nature, we do know that there must be both orientation and distance dependence in the intermolecular pair potentials. That is, there must exist forces that

cause the molecules to align parallel to each other and to form layers perpendicular to the director. Kobayashi^{1,2} has suggested a simple form of pair interaction potential that contains the minimum necessary features:

$$V_{12} = U(r) + W(r)P_2(\cos\theta_{12}), \quad [12]$$

where r is the separation between the centers of mass of the molecules and θ_{12} is the angle between their long axes. The functional dependence of U and W on r is not specified; $U(r)$ represents the short range central forces while $W(r)$ describes the orientational forces due to the anisotropic dispersion forces, quadrupole-quadrupole forces, etc.

An exact statistical theory of smectics based on the pair potential, Eq. [12], is extremely difficult to accomplish. Therefore we derive a mean-field approximation to the theory. For this purpose we require the mean-field version of the single molecule potential function. In a previous paper⁸ this problem was examined for the case of the nematic phase. A perfectly general form of V_{12} was assumed and expanded in a series of spherical harmonics. A new coordinate system was then chosen such that the polar axes coincided with the director. The single molecule potential was then obtained by averaging V_{12} over all possible positions and orientations of molecule 2 consistent with the structure of the nematic phase. The resulting single molecule potential had the form

$$V_1(\cos\theta) = \sum_L^{(\text{even})} \left\langle \sum_m U_{L,L,m}(r) \right\rangle \langle P_L \rangle P_L(\cos\theta), \quad [13]$$

where the constants $\langle \sum_m U_{L,L,m}(r) \rangle$ are the averages of the distance dependent parts of the potential (averaged over all intermolecular separations), and where the $\langle P_L \rangle$ are the averages of the Legendre polynomials averaged with respect to the nematic orientational distribution function. The term in $L = 0$ is a constant and was discarded; the term in $L = 2$ led to the Maier-Saupe⁶ version of the theory of nematics.

The analogous process applied to the Kobayashi potential, Eq. [12], in the case of the smectic-A structure is at the same time simpler and more complex. It is simpler because Eq. [12] exhibits a simple angular dependence and higher-order P_L do not enter the calculation. It is more complex, however, because we are now required to average over the positions and orientations of the second molecule in a way consistent with the smectic-A structure; that is, with a distribution

function that depends on both angular and spatial coordinates, the $f(\cos\theta, z)$ discussed in Section 2 above. Applying these averaging procedures to Eq. [12] we obtain the single molecule potential as

$$V_1(\cos\theta, z) = \langle U(r) \rangle + \langle W(r)P_2 \rangle P_2(\cos\theta), \quad [14]$$

where the averages $\langle U(r) \rangle$ and $\langle W(r)P_2 \rangle$ are functions of z , the position of the centers of mass of the molecule of interest with respect to the layers, and where θ is the angle between the axis of this molecule and \hat{n} . In obtaining Eq. [14] we have used the relation, $P_2(\cos\theta_{12}) = P_2(\cos\theta_1)P_2(\cos\theta_2) +$ terms in $\varphi_2 - \varphi_1$. The terms in the azimuthal angle φ vanish in the averaging process since the smectic-A phase has cylindrical symmetry. It has been customary in the treatment¹⁻⁴ of the smectic-A phase to further simplify the potential by expanding the position dependent terms in a Fourier series. Taking $U(r)$ as an example:

$$U(r_{12}) = \frac{2}{\pi} \int_0^\infty \tilde{U}(x_{12}, y_{12}; s) \cos sz_{12} ds,$$

where \tilde{U} is the Fourier transform of U ,

$$\tilde{U}(s) = \tilde{U}(x_{12}, y_{12}; s) = \frac{1}{2\pi} \int_0^\infty U(r'_{12}) \cos sz_{12} dz_{12}.$$

Taking the average of U over the smectic-A distribution of molecule 1,

$$\langle U(r_{12}) \rangle = \sum_n \langle U_n \rangle \left\langle \cos\left(\frac{2\pi n z_1}{d}\right) \right\rangle \cos\left(\frac{2\pi n z_2}{d}\right), \quad [15]$$

where the coefficient $\langle U_n \rangle = \langle \tilde{U}(2\pi n/d) \rangle (2/\pi)$. The several steps required to obtain this form of Eq. [15] are presented in the Appendix. Since there is no ordering of the molecules in the layers, the $\langle U_n \rangle$ are just constants. The same considerations as above apply to the $W(r)$ portion of the potential. Retaining only the first few terms gives the result

$$V_1(\cos\theta, z) = U_0 + U_1 \tau \cos\left(\frac{2\pi z}{d}\right) + \dots \\ + \left[W_0 \eta + W_1 \sigma \cos\left(\frac{2\pi z}{d}\right) + \dots \right] P_2(\cos\theta), \quad [15]$$

where $U_0, U_1, W_0,$ and W_1 are the Fourier coefficients of U and W , and where $\eta, \tau,$ and σ are the order parameters, the average values in-

troduced earlier, Eq. [11]. U_0 is a constant and can be discarded. This version of the potential function is particularly instructive in demonstrating the cooperative nature of the formation of the smectic-A structure. The U_1 term shows the influence of the translational order τ in forcing the molecules into layers, the W_0 term shows the influence of the orientational order parameter η in forcing the molecules to align with \hat{n} , while the W_1 term shows how the degree of translational order can influence the orientational order (and vice versa) through the action of the mixed parameter σ .

Specific forms of the functions $U(r)$ and $W(r)$ were chosen by McMillan:^{3,4}

$$\begin{aligned} W(r) &= -\frac{v}{r_0^3 \pi^{3/2}} \exp\{- (r/r_0)^2\}, \\ U(r) &= \delta W(r), \end{aligned} \quad [16]$$

where v and δ are constants characterizing the strengths of the two parts of the interaction, and where r_0 specifies the range of interaction; r_0 is of the order of the length of the molecules. The Fourier coefficients of Eq. [16] are

$$\begin{aligned} W_0 &= -v, U_1 = \delta W_1, \\ W_1 &= -v\alpha = -2v e^{-\pi r_0/d)^2}. \end{aligned} \quad [17]$$

Substitution of Eq. [17] into Eq. [15] gives the McMillan model of the potential in the form

$$\begin{aligned} V_{M}(\cos\theta, z) &= -v \left\{ \delta\alpha\tau \cos\left(\frac{2\pi z}{d}\right) \right. \\ &\left. + \left[\eta + \alpha\sigma \cos\left(\frac{2\pi z}{d}\right) \right] P_2(\cos\theta) \right\}. \end{aligned} \quad [18]$$

The functional dependence chosen in Eq. [16] makes it convenient to discuss the variation of liquid-crystal behavior in homologous series. Lengthening the alkyl chains in a series increases the spacing d . This decreases the ratio r_0/d and hence increases the parameter α introduced in Eq. [17]. The properties of the short end of the homologous series can thus be computed using small values of α while those at the long end of the series will require larger values of α .

5. Statistical Thermodynamics

Having derived a particular form of the single molecule potential function in the mean-field approximation, we are now in a position to

calculate the thermodynamic properties of the model. According to the rules of classical statistical mechanics the single molecule distribution function corresponding to the potential function, Eq. [18], is

$$f_M(\cos\theta, z) = Z^{-1} \exp[-\beta V_M(\cos\theta, z)], \quad [19]$$

$$Z = \int_0^1 \int_0^d \exp[-\beta V_M(\cos\theta, z)] dz d(\cos\theta),$$

where Z is the single molecule partition function and $\beta = 1/kT$ (k is Boltzmann's constant and T the temperature). The integrations can be restricted to $0 \leq \cos\theta \leq 1$ since V_M is even in $\cos\theta$, and $0 \leq z \leq d$ since V_M is periodic. The distribution function as it stands in Eq. [19] is not as yet useful for computing average values or thermodynamic quantities. The potential, V_M , Eq. [18], contains the as yet undetermined order parameters η , τ , and σ . The self-consistent determination of the order parameters and their temperature dependence can be realized by combining their definition, Eq. [11] with Eq. [19]:

$$\eta = \int_0^1 \int_0^d P_2(\cos\theta) f_M(\cos\theta, z) dz d(\cos\theta),$$

$$\tau = \int_0^1 \int_0^d \cos\left(\frac{2\pi z}{d}\right) f_M(\cos\theta, z) dz d(\cos\theta), \quad [20]$$

$$\sigma = \int_0^1 \int_0^d P_2(\cos\theta) \cos\left(\frac{2\pi z}{d}\right) f_M(\cos\theta, z) dz d(\cos\theta).$$

Each of the above equations contains one of the order parameters on the left and all three order parameters in the integrals on the right. The simultaneous solution of these three equations yields the temperature dependence of the order parameters.

The set of self-consistent equations above admits a number of simultaneous solutions. In addition to the smectic-A, nematic, and isotropic solutions, Eq. [20] also yields various less physical solutions. To find which of the possible solutions represents the physically observed states we must calculate the free energy and determine which solution gives the minimum in this quantity at different temperatures.

The energy, entropy, and free energy are obtained in exactly the same way as described in earlier papers^{7,8} on the simpler theory of the nematics:

$$E = \frac{1}{2} N \langle V_M \rangle = -\frac{1}{2} N u (\eta^2 + \alpha \delta \tau^2 + \alpha \sigma^2), \quad [21]$$

$$S = -Nk(\ln f_M) \quad [22]$$

$$= -\frac{N\nu}{T}(\eta^2 + \alpha\delta\tau^2 + \alpha\sigma^2) + Nk\ln Z,$$

$$F = -NkT\ln Z + \frac{1}{2}N\nu(\eta^2 + \alpha\delta\tau^2 + \alpha\sigma^2), \quad [23]$$

where N is the number of molecules present. Just as in the case of the mean-field theories of the nematics,^{7,8} the free energy is found to contain an additional term beyond the usually expected $\ln Z$ term. Again, these terms arise because we have approximated a pair potential V_{12} by a temperature-dependent single molecule potential V_M . The form of Eq. [23] can be verified to be correct, however. Setting the partial derivatives of F with respect to η , τ , and σ to zero regains the self-consistency conditions, Eq. [20]. Further testing Eqs. [21] and [23] we see that they do satisfy the thermodynamic identity, $E = (\partial\beta F/\partial\beta)$.

6. Numerical Results

McMillan has obtained numerical solutions to Eqs. [20] through [23] for several sets of the potential parameters δ and α . In his first paper³ he did not yet realize the need for the $U(r)$ term in the potential, Eq. [12], so that he was treating the case of $\delta = 0$. In his subsequent paper⁴ he included the missing term. These two sets of results are now examined.

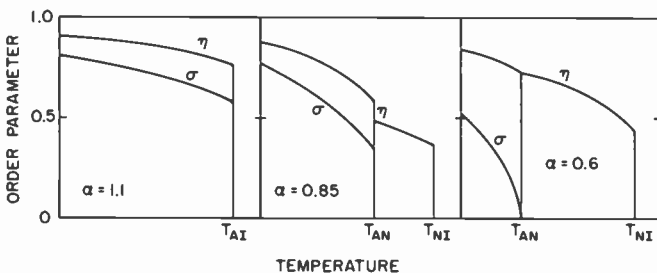


Fig. 3—Temperature dependence of the order parameters for $\delta = 0$ and several values of α (after Ref. [3]).

When $\delta = 0$, the term in τ drops out of the potential, Eq. [18], and the theory now involves only the order parameters η and σ . The translational order of the smectic-A phase is then described only by the mixed-order parameter σ . Fig. 3 shows the temperature depen-

dence of the order parameters for three representative values of α . For $\alpha = 1.1$ (long chain length) η and σ change discontinuously at the same temperature; both the translational and orientational order vanish simultaneously. There is thus a first-order phase change from the smectic-A structure directly into the isotropic fluid; no nematic phase exists. For $\alpha = 0.85$, η and σ display discontinuities at T_{AN} but only σ vanishes. η then vanishes discontinuously at a higher temperature T_{NI} . The system thus displays a first-order transition from smectic-A to nematic followed by another first-order transition from nematic to isotropic. For $\alpha = 0.6$ (short chain length), σ is seen to vanish continuously at a temperature T_{AN} . η shows a discontinuity in slope at this temperature then vanishes discontinuously at a higher temperature T_{NI} . There is thus a second-order phase transition from smectic-A to nematic followed by the usual first-order transition from nematic to isotropic.

The collection of phase transition temperatures obtained from the model with $\delta = 0$ and for numerous values of α is summarized in the phase diagram shown in Fig. 4a. These results are to be compared with the schematic phase diagram shown in Fig. 4b; this diagram is representative of many real systems and displays the features discussed in Section 3. Note that while there is qualitative agreement between the model and experiment, there are numerous significant discrepancies in the overall behavior of the phase transition lines.

The entropy changes of the smectic-A to nematic phase transitions have also been computed with $\delta = 0$ and for numerous values α . The results are summarized in Fig. 5, where we have plotted ΔS as a function of the ratio T_{AN}/T_{NI} ; small values of T_{AN}/T_{NI} correspond to short chain length, large values of T_{AN}/T_{NI} to long chain length (see Fig. 4a). The results of this model are shown as the solid line; the points are experimental, taken from the homologous series described in Fig. 2. Again, there is qualitative agreement in that the general trend and order of magnitude are correct, but there are serious discrepancies.

In his second paper⁴ McMillan included all the terms in the potential, Eq. [18] and studied the model for several values of δ and α . He was particularly interested in two substances, cholesteryl nonanoate and cholesteryl myristate. The nonanoate calculations were made using $\alpha \approx 0.41$; $\delta = 0$ and 0.65; for the myristate, $\alpha \approx 0.45$ was chosen with $\delta = 0$ and 0.65. With $\delta = 0.65$ the temperature dependences of the order parameters for both values of α were similar in appearance to those shown in Fig. 3b. In both examples η looked like the η of Fig. 3b while τ and σ resembled the σ of Fig. 3b. The model thus displayed successive first-order phase changes—smectic-A to cholesteric fol-

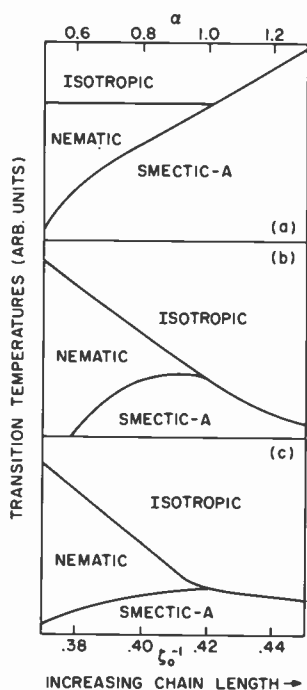


Fig. 4—Schematic phase diagrams for liquid crystals: (a) theory of McMillan,³ (b) schematic representation of typical experimental diagrams and (c) theory of Lee et al (after Ref. [5]).

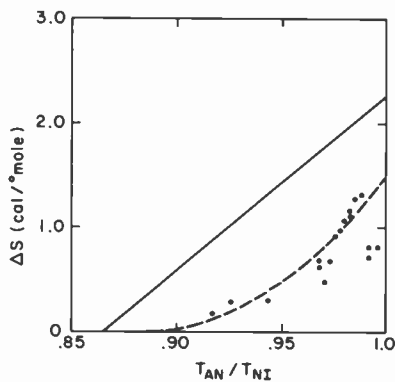


Fig. 5—Entropy of transition plotted as a function of the ratio T_{AN}/T_{NI} . Solid curve is theory of McMillan,³ dashed curve is theory of Lee et al⁵ and the points are experimental^{12,13} for compounds of Fig. 2 (after Ref. [5]).

lowed by cholesteric to isotropic in agreement with experimental observations. A quantitative test of the theory was attempted by comparing the temperature dependence of τ^2 with the measured x-ray Bragg scattering intensity (to which it is proportional). The results are shown in Fig. 6. In the case of the myristate, excellent agreement

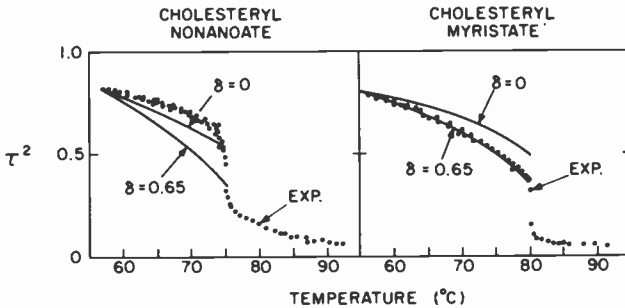


Fig. 6—Comparison of calculated and observed Bragg scattering intensity (after Ref. [4]).

with experiment is obtained using the value $\delta = 0.65$. For the nonanoate, however, the agreement between theory and experiment is poor, although the calculation with $\delta = 0$ is somewhat better than with $\delta = 0.65$. Phase diagrams such as those shown in Fig. 4 were not computed for finite values of δ . This is unfortunate, since it is important to know whether finite values of δ in the potential, Eq. [18], would have improved the appearance of the theoretical phase diagram, Fig. 4a.

7. Improved Theory

Motivated primarily by the disagreement between the theoretical and experimental phase diagrams, Fig. 4 (a and b), Lee et al⁵ have derived a modified version of the mean-field theory of smectic-A liquid crystals. The authors begin by adopting the McMillan form of the Kobayashi pair potential, Eqs. [12] and [16]. The pair potential is then treated intact without going into the process of deriving the equivalent mean-field single molecule potential. Further, the pair potential is *not* expanded in a truncated Fourier series as in the manner leading to Eq. [15].

The statistical thermodynamics is based on the variational principle. Guided by Eqs. [18] and [19], the following variational form was chosen for the single molecule distribution function (of the i -th molecule):

$$f(\cos\theta_i, z_i) = Z^{-1} \exp\{-\beta V(\cos\theta_i, z_i)\}$$

$$Z = \int_0^1 \int_0^d \exp\{-\beta V(\cos\theta_i, z_i)\} dz_i d(\cos\theta_i), \quad [24]$$

$$V(\cos\theta_i, z_i) = -v \left[a P_2(\cos\theta_i) + b P_2(\cos\theta_i) \cos\left(\frac{2\pi z_i}{d}\right) + c \delta \cos\left(\frac{2\pi z_i}{d}\right) \right], \quad [25]$$

where a , b , and c are variational parameters. The values of these parameters as a function of the temperature are determined by minimizing the free energy. The free energy was taken to have the form

$$F = NkT \int_0^1 \int_0^d f(\cos\theta_1, z_1) \ln f(\cos\theta_1, z_1) dz_1 d(\cos\theta_1)$$

$$+ \frac{1}{2} N^2 \int_0^1 \int_0^d \int_0^1 \int_0^d f(\cos\theta_1, z_1) f(\cos\theta_2, z_2) V_{12}(\theta_{12}, z_{12})$$

$$\times dz_1 d(\cos\theta_1) dz_2 d(\cos\theta_2), \quad [26]$$

where the first term comes from the entropy contribution (similar to Eq. [22]), and where the second term is the energy E written in terms of the average value of the pair potential. Although the energy is computed from a pair potential (in contrast to the usual mean-field definition, Eq. [21]) the free energy as written in Eq. [26] is still a mean-field approximation. The reason for this is the use of two single-molecule distribution functions in place of the proper (but unknown) pair distribution function in calculating E from V_{12} . The form of F is self-consistent, however, and, along with the variational conditions (Eq. [27] below), does satisfy the required thermodynamic identity, $E = (\partial F / \partial \beta)$.

The temperature dependence of the variational parameters a , b , and c are obtained from minimization of the free energy, Eq. [26]:

$$\left(\frac{\partial F}{\partial a}\right) = \left(\frac{\partial F}{\partial b}\right) = \left(\frac{\partial F}{\partial c}\right) = 0. \quad [27]$$

Of the many possible solutions to these equations we take only those giving the absolute minimum in F . The temperature dependence of the order parameters η , τ , and σ are then calculated by combining the equilibrium solutions of Eq. [27] with Eqs. [11], [24] and [25]. We note in passing that if the pair potential $V_{12}(\theta_{12}, z_{12})$ could be written in (or approximated by) a separable form $V_1(\theta_{12}, z_{12}) V_1(\theta_{22}, z_{22})$, then $\eta = a$, $\sigma = b$, and $\tau = c$.

Numerical calculations were performed⁵ using $\delta = 0.65$ and numerous values of the range parameter $\zeta_0 = 2\pi r_0/d$, where r_0 is the range of the interaction and d is the layer spacing (ζ_0 plays the same role in parameterizing chain length as McMillan's α). The collection of phase-transition temperatures obtained is displayed in Fig. 4c. The agreement between the theoretical diagram and the representative experimental phase diagram, Fig. 4b, is nothing less than remarkable. All the features described in Section 3 and shown in Fig. 4b are indeed present in the theoretical results. Numerical calculations of the entropy changes of the smectic-A to nematic phase transition were also made. Fig. 5 shows the results, ΔS plotted vs. the ratio T_{AN}/T_{NI} ; the result of this calculation is depicted as the dashed line. The agreement with the experimental points is again remarkable. Note further that this theory predicts that the entropy change, ΔS (Fig. 5) will go to zero at $T_{AN}/T_{NI} = 0.88$; the first-order smectic-A to nematic phase change becomes second order. This feature is examined in more detail in the next section.

The comparison of the results of the two models in Figs. 4 and 5 shows that Lee et al⁵ have indeed made a very significant improvement over the original considerations of McMillan.³ Three important changes were made in the theory: (a) the theory was based on a variational principle with E being computed from a pair potential V_{12} ; (b) the complete Kobayashi form of potential was used (finite δ); and (c) the pair potential was not approximated by a truncated Fourier series. With all three improvements made simultaneously one can only speculate as to which is the most important. (a) seems not to be a major factor; the resulting theory is still a mean-field approach, and using V_{12} in E should only influence small details. (c) is certainly an important factor. The influence of this improvement cannot be too great, however, since the variational form for the potential of mean force, Eq. [25], is in effect a truncated Fourier series of the true potential. (b) seems to be the most important. The influence of the purely translational term U in the Kobayashi potential, Eq. [12], must be the over-riding factor that produced the spectacular improvements depicted in Figs. 4 and 5.

8. The Possibility of Second-Order Transitions

The question of whether the normally first-order smectic-A to nematic phase transition can be second order in some materials is somewhat controversial. All of the published mean-field theories¹⁻⁵ of the smectic-A phase do exhibit second-order phase changes for certain values of the potential parameters. In both McMillan's theory³ and that of Lee et al,⁵ the second-order transition is predicted to occur at that end of homologous series having short chain lengths. More specifically, these models predict the second-order changes to occur when the ratio of transition temperatures T_{AN}/T_{NI} (or T_{AC}/T_{CI}) is at or below about 0.88 (see Fig. 5).

The experimental situation is contradictory. For the homologous series of 4-n-alkoxybenzylidene-4'-phenylazoanilines, Doane et al¹⁴ have observed a possible second-order smectic-A to nematic transition at the extreme short end of the series. In the case of COC (cholesteryl oleyl carbonate), Keyes et al¹⁵ found the first-order phase transition to change to second order at a pressure of 2.66 kbar where $T_{AC}/T_{CI} = 0.88$. The phase transitions of CBAOB (p-cyanobenzylidene-amino-p-n-octyloxybenzene)^{16,17} and CBOOA (p-cyanobenzylidene-p'-octyloxyaniline)^{18,19} have also been believed to be of second order. Torza and Cladis,²⁰ on the other hand, have concluded from volumetric studies that the smectic-A to nematic phase transition is unambiguously first order in CBOOA. Lin, Keyes, and Daniels²¹ concur in this conclusion based on high pressure studies of CBOOA. In any case, we must be mindful of the fact that the experimental verification of the order of the phase transition in these examples is most difficult. The entropy and volume discontinuities are very small and near critical fluctuations are present to complicate the interpretation. (The nature of fluctuations in the nematic to isotropic transition has been discussed in a previous paper.⁷)

The situation with respect to Landau-type phenomenological theories is also contradictory. Drawing an analogy between the smectic-A phase of liquid crystals and the superconducting phase of metals, de Gennes^{22,23} has constructed a phenomenological theory from which he concludes that the smectic-A to nematic phase transition can be second order. Halperin and Lubensky,²⁴ on the other hand, have improved the analogy with superconductors and conclude that the transition will always be at least weakly first order.

My own conjecture in this matter is that the smectic-A to nematic phase transition is always first order. The basis of my argument is the analogy between this transition and the melting of a crystalline solid. When a crystal melts, three dimensional long-range translational

order disappears; when a smectic-A goes nematic, one-dimensional long-range translational order disappears.

Kirkwood^{10,11} has pointed out that the density distribution function of a crystalline solid (the translational molecular distribution function) can be expanded in a three-dimensional Fourier series. The coefficients in this series are then identified as the order parameters of the crystalline phase. All these order parameters vanish discontinuously at the first-order melting point. Empirically, there are no second-order melting transitions, nor do there seem to be any solid-liquid critical points. Though not a proven fact (as far as I am aware), it seems reasonable that crystal melting is always first order because all of the order parameters cannot vanish simultaneously and continuously before the free energy of the solid phase exceeds that of the liquid phase.

In the smectic-A phase, the single-molecule distribution function, Eqs. [7] and [10] can likewise be represented as a (one-dimensional) Fourier series in which all the coefficients may be considered order parameters. The disappearance of smectic-A order requires the simultaneous vanishing of all the order parameters. That they all can vanish simultaneously and continuously before the free energy of the smectic-A phase exceeds that of the nematic phase seems just as unlikely here as in the (empirically verified) case of the crystalline solids. It seems clear to me that the reason the various theoretical treatments mentioned above can exhibit second-order phase changes is that an insufficient number of order parameters is included. In all the treatments, either the potential, the potential of mean force, or the distribution function are expressed in terms of highly truncated Fourier series. Such truncation automatically limits the number of order parameters. Small numbers of order parameters can then vanish simultaneously and continuously under certain conditions providing the spurious second-order phase transitions.

Appendix

The average value of $U(r_{12})$, averaged over the distribution of molecule 1 is defined by

$$\langle U(r_{12}) \rangle = \int_0^\infty f(z_1) U(r_{12}) dz_1; \int_0^\infty f(z_1) dz_1 = 1, \quad [28]$$

where we have temporarily suppressed the angular dependence of f for clarity. Substituting the Fourier integral representation of U ,

$$\begin{aligned}
 \langle U(r_{12}) \rangle &= \frac{2}{\pi} \int_0^\infty \int_0^\infty f(z_1) \langle \tilde{U}(s) \rangle \cos sz_{12} ds dz_1, \\
 &= \frac{2}{\pi} \int_0^\infty \langle \tilde{U}(s) \rangle \langle \cos sz_1 \rangle \cos sz_2 ds,
 \end{aligned}
 \tag{29}$$

where $\langle \tilde{U}(s) \rangle$ is the Fourier transform \tilde{U} averaged over all the (random) positions of the molecules in the layers, and where the sine terms which come from $\cos sz_{12} = \cos s(z_2 - z_1)$ are omitted since they will vanish in the averaging. The next step is to evaluate $\langle \cos sz_1 \rangle$ using the expansion, Eq. [6]:

$$\begin{aligned}
 \langle \cos sz_1 \rangle &= \int_0^\infty f_1(z_1) \cos sz_1 dz_1, \\
 &= \frac{2}{d} \sum_n \left\langle \cos \left(\frac{2\pi n z}{d} \right) \right\rangle \int_0^\infty \cos \left(\frac{2\pi n z_1}{d} \right) \cos sz_1 dz_1, \\
 &= \sum_n \left\langle \cos \left(\frac{2\pi n z}{d} \right) \right\rangle \delta \left(s - \frac{2\pi n}{d} \right).
 \end{aligned}
 \tag{30}$$

where δ is the usual delta function. Substitution of the result of Eq. [30] into Eq. [29] gives

$$\begin{aligned}
 \langle U(r_{12}) \rangle &= \frac{2}{\pi} \int_0^\infty \langle \tilde{U}(s) \rangle \sum_n \left\langle \frac{\cos 2\pi n z}{d} \right\rangle \delta \left(s - \frac{2\pi n}{d} \right) \cos sz_2 ds, \\
 &= \frac{2}{\pi} \sum_n \left\langle \tilde{U} \left(\frac{2\pi n}{d} \right) \right\rangle \left\langle \cos \frac{2\pi n z}{d} \right\rangle \cos \frac{2\pi n z_2}{d},
 \end{aligned}
 \tag{31}$$

which is the desired result, Eq. [15].

References

- ¹ K. K. Kobayashi, "Theory of Translational and Orientational Melting with Application to Liquid Crystals," *J. Phys. Soc. (Japan)*, **29**, p. 101 (1970).
- ² K. K. Kobayashi, "Theory of Translational and Orientational Melting with Application to Liquid Crystals," *Mol. Cryst. Liq. Cryst.*, **13**, p. 137 (1971).
- ³ W. L. McMillan, "Simple Molecular Model for the Smectic-A Phase of Liquid Crystals," *Phys. Rev.*, **A4**, p. 1238 (1971).
- ⁴ W. L. McMillan, "X-ray Scattering from Liquid Crystals. I. Cholesteryl Nonanoate and Myristate," *Phys. Rev.*, **A6**, p. 936 (1972).
- ⁵ F. T. Lee, H. T. Tan, Y. M. Shih, and C. W. Woo, "Phase Diagram for Liquid Crystals," *Phys. Rev. Lett.*, **31**, p. 1117 (1973).
- ⁶ W. Maier and A. Saupe, *Z. Naturforsch.*, **14a**, p. 882 (1959) and **15a**, p. 287 (1960).
- ⁷ P. J. Wojtowicz, "Introduction to the Molecular Theory of Nematic Liquid Crystals," *RCA Rev.*, **35**, p. 105 (1974).
- ⁸ P. J. Wojtowicz, "Generalized Mean Field Theory of Nematic Liquid Crystals," *RCA Rev.*, **35**, p. 118 (1974).

- ⁹ E. B. Priestley, "Nematic Order: The Long Range Orientational Distribution Function," *RCA Rev.* **35**, p. 144 (1974).
- ¹⁰ J. G. Kirkwood and E. Monroe, "Statistical Mechanics of Fusion," *J. Chem. Phys.*, **9**, p. 514 (1941).
- ¹¹ J. G. Kirkwood, "Crystallization as a Cooperative Phenomenon," p. 67 in *Phase Transformations in Solids*, ed. by R. Smoluchowski, J. Wiley and Sons, Inc., New York, (1951).
- ¹² H. Arnold, *Z. Physik Chem. (Leipzig)* **239**, p. 283 (1968); **240**, p. 185 (1969).
- ¹³ G. J. Davis and R. S. Porter, "Evaluation of Thermal Transitions in Some Cholesteryl Esters of Saturated Aliphatic Acids," *Mol. Cryst. Liq. Cryst.*, **10**, p. 1 (1970).
- ¹⁴ J. W. Doane, R. S. Parker, B. Cvilk, D. L. Johnson, and D. L. Fishel, "Possible Second-Order Nematic-Smectic-A Phase Transition," *Phys. Rev. Lett.*, **28**, p. 1694 (1972).
- ¹⁵ P. H. Keyes, H. T. Weston, and W. B. Daniels, "Tricritical Behavior in a Liquid-Crystal System," *Phys. Rev. Lett.*, **31**, p. 628 (1973).
- ¹⁶ W. L. McMillan, "Measurement of Smectic-A Phase Order-Parameter Fluctuations near a Second Order Smectic-A Nematic Phase Transition," *Phys. Rev.*, **7A**, p. 1419 (1973).
- ¹⁷ B. Cabane and W. G. Clark, "Orientational Order in the Vicinity of a Second Order Smectic-A to Nematic Phase Transition," *Solid State Comm.*, **13**, p. 129 (1973).
- ¹⁸ L. Chueng, R. B. Meyer, and H. Gruler, "Measurement of Nematic Elastic Constants near a Second Order Nematic-Smectic-A Phase Change," *Phys. Rev. Lett.*, **31**, p. 349 (1973).
- ¹⁹ M. Delaye, R. Robatta, and G. Durand, "Rayleigh Scattering at a Second Order Nematic to Smectic-A Phase Transition," *Phys. Rev. Lett.*, **31**, p. 443 (1973).
- ²⁰ S. Torza and P. E. Cladis, "Volumetric Study of the Nematic-Smectic-A Transition of N-p-cyano-benzylidene-p-octyloxyaniline," *Phys. Rev. Lett.*, **32**, p. 1406 (1974).
- ²¹ W. J. Lin, P. H. Keyes, and W. B. Daniels, private communication.
- ²² P. G. de Gennes, "An Analogy Between Superconductors and Smectics-A," *Solid State Comm.* **10**, p. 753 (1972).
- ²³ P. G. de Gennes, "Some Remarks on the Polymorphism of Smectics," *Mol. Cryst. Liq. Cryst.*, **21**, p. 49 (1973).
- ²⁴ B. I. Halperin and T. C. Lubensky, "On the Analogy Between Smectic-A Liquid Crystals and Superconductors," *Solid State Comm.*, **14**, p. 997 (1974).

Introduction to the Elastic Continuum Theory of Liquid Crystals

Ping Sheng

RCA Laboratories, Princeton, N. J. 08540

Abstract—The fundamental equations of the continuum theory of nematic and cholesteric liquid crystals are obtained by considering the form of free energy associated with a spatially-varying orientational director field. In terms of the continuum theory we discuss the following four effects: (1) the twisted nematic cell, (2) the magnetic (electric) coherence length, (3) the Fréedericksz transition, and (4) the unwinding of the cholesteric helix in a static magnetic (electric) field.

1. Introduction

In the previous papers of this series we have seen that in terms of molecular theories^{1,2} one can calculate and successfully explain various properties of mesophase transitions. However, there exists a class of liquid-crystal phenomena involving the response of bulk liquid-crystal samples to external disturbances, with respect to which the usefulness of a molecular theory is not immediately obvious. These phenomena are usually distinguished by two characteristics: (1) the energy involved, per molecule, in producing these effects is small compared to the strength of intermolecular interaction; and (2) the characteristic distances involved in these phenomena are large compared to molecular dimensions. In describing these large-scale phenomena, it is more convenient to regard the liquid crystal as a continuous medium with a set of elastic constants than to treat it on a molecular basis. Based on this viewpoint, Zocher,³ Oseen,⁴ and Frank⁵ devel-

oped a phenomenological continuum theory of liquid crystals that is very successful in explaining various magnetic (electric) field-induced effects. It is the purpose of the present paper to develop this elastic continuum theory for nematic and cholesteric liquid crystals and to discuss and illustrate its use. In this paper, the derivation of the fundamental equation of the elastic continuum theory is followed by the application of the theory to four effects: (1) the twisted nematic cell, (2) the magnetic (electric) coherence length, (3) the Fréedericksz transition, and (4) the magnetic (electric) field-induced cholesteric-nematic transition.

2. The Fundamental Equation of the Continuum Theory of Liquid Crystals

In previous papers we have seen that liquid crystals are characterized by an orientational order of their constituent rod-like molecules.^{1,2,6,7} In nematic liquid crystals this orientational order has uniaxial (cylindrical) symmetry, the axis of uniaxial symmetry being parallel to a unit vector \hat{n} , called the director. Let us now consider a very small spatial region inside a macroscopic sample of nematic liquid crystal that contains a sufficiently large number of molecules so that the long-range orientational order is well defined within that region. Such a spatial region can be characterized by a director pointing along the of local axis of uniaxial orientational symmetry. Let us imagine the division of the macroscopic sample into such small spatial regions. In each of the regions, we define an orientational director. In this manner the macroscopic sample of nematic liquid crystal can be characterized by a local director at every spatial "point," where we use the term point loosely to mean a small region of space as defined above. Obviously, this characterization of orientational order by a director field, $\hat{n}(\vec{r})$, is not limited to nematic liquid crystals, which we have used as an example in the above discussion. In fact, the director-field characterization can be applied equally well to cholesteric liquid crystals, since, locally, cholesterics also possess uniaxial symmetry in their orientational order. However, for convenience, we will continue to use nematic liquid crystals as our reference in the following discussion. The generalization of the theory will be made at appropriate places to permit application to cholesteric liquid crystals. In what follows, we first consider the free energy associated with a distortion in the director field. Next, we examine the free energy associated with the interaction of liquid crystals with external fields. The combination of all the free-energy contributions then yields the fundamental equation, which is an expression for the

total free energy of a sample of nematic or cholesteric liquid crystal in an external field.

The starting point for the development of continuum theory is the consideration of the equilibrium state. In nematic liquid crystals, parallel alignment of all the local directors represents the equilibrium state, or the state of minimum free energy. However, when we perturb the system by pinning the surface directors to the walls of the container, applying an external field, or introducing thermal fluctuations, the local directors will no longer be spatially invariant. A quantitative formulation of the above statements is that the quantities dn_α/dx_β , (where x is the spatial variable and the subscripts $\alpha, \beta = 1, 2, 3$ denote the components along the three orthogonal axes of the Cartesian coordinate system) are zero for the equilibrium state but are nonzero for some, or all, values of α and β when the system is distorted. In other words, we can think of dn_α/dx_β as the distortion parameters, and the equilibrium state is given by the uniformly aligned state for which $dn_\alpha/dx_\beta = 0$ everywhere. Since the distorted state represents a state with higher free energy than the equilibrium state, we can write the free-energy density of the distorted state as

$$f(\text{distorted}) = f_0(\text{equilibrium}) + \Delta f. \quad [1]$$

where f and f_0 are the free-energy densities of the distorted and equilibrium states, respectively; Δf (>0) is a function of the n_α and the dn_α/dx_β that vanishes when all $dn_\alpha/dx_\beta = 0$. Since, in general, $dn_\alpha/dx_\beta \ll (\text{molecular dimension})^{-1}$ for the phenomena of interest, we can expand Δf as a power series in the n_α and the dn_α/dx_β and retain only the lowest-order nonvanishing terms of the series. Let \mathcal{F}_D (subscript D stands for distortion) denote such an approximation to Δf . \mathcal{F}_D must satisfy several requirements. First, since we are expanding in powers of the dn_α/dx_β around $dn_\alpha/dx_\beta = 0$, which is a free-energy minimum, the lowest-order nonvanishing terms must be quadratic in the dn_α/dx_β (i.e. proportional to terms of the form $(dn_\alpha/dx_\beta) \cdot (dn_\gamma/dx_\delta)$). Second, since the "head" and the "tail" of a nematic director represent the same physical state, \mathcal{F}_D must be even in the n_α . Third, \mathcal{F}_D must be a scalar quantity. In addition, we will discard terms of the form $\nabla \cdot \tilde{u}(\vec{r})$ where $\tilde{u}(\vec{r})$ is any arbitrary vector field, since they represent surface contributions to the distortion free-energy density and are assumed to be small (by Gauss's Theorem, $\int \nabla \cdot \tilde{u}(\vec{r}) dV = \int d\hat{\sigma} \cdot \tilde{u}(\vec{r})$, where $d\hat{\sigma}$ is a surface element with unit vector perpendicular to the surface). With the above constraints, it can be shown⁵ that \mathcal{F}_D contains only three linearly independent terms. They are (1)

$[\nabla \cdot \hat{n}(\vec{r})]^2$, (2) $[\hat{n}(\vec{r}) \cdot \nabla \times \hat{n}(\vec{r})]^2$, and (3) $[\hat{n}(\vec{r}) \times \nabla \times \hat{n}(\vec{r})]^2$. It is obvious that all three terms satisfy the requirements stated above. Interested readers are referred to Refs. [5] and [8] for proofs that these three terms are indeed unique. In Fig. 1 we show the physical distortions

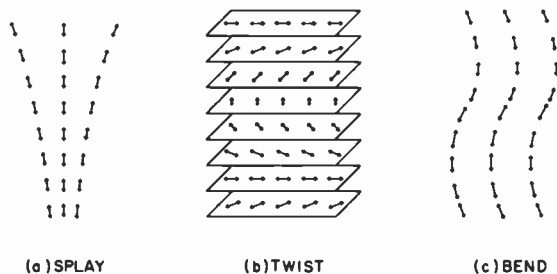


Fig. 1—Three types of distortion in a director field: (a) gives $\nabla \cdot \hat{n}(\vec{r}) \neq 0$, (b) gives $\hat{n}(\vec{r}) \cdot \nabla \times \hat{n}(\vec{r}) \neq 0$, and (c) gives $\hat{n}(\vec{r}) \times \nabla \times \hat{n}(\vec{r}) \neq 0$. Each director is shown with double arrows in order to indicate that the "head" and the "tail" directions represent exactly the same physical state in a nematic sample.

tions of the director field associated with the three terms. The first term is called "splay," the second term "twist," and the third term "bend." \mathcal{F}_D can now be written as

$$\mathcal{F}_D = \frac{1}{2} \{ K_{11} [\nabla \cdot \hat{n}(\vec{r})]^2 + K_{22} [\hat{n}(\vec{r}) \cdot \nabla \times \hat{n}(\vec{r})]^2 + K_{33} [\hat{n}(\vec{r}) \times \nabla \times \hat{n}(\vec{r})]^2 \}. \quad [2]$$

where the constants K_{11} , K_{22} , K_{33} are, respectively, the splay, twist, and bend elastic constants and are named collectively as the Frank elastic constants. The factor $\frac{1}{2}$ is included so that the K 's may agree with their historical definitions. Since \mathcal{F}_D must be positive in order to give stability for the uniformly aligned state, all the K 's must be positive. As for their values, we note that the theoretical determination of the K 's from molecular parameters represents a task of linking the continuum theory to the microscopic theories of liquid crystals and is beyond the scope of the present paper. However, from dimensional analysis we can get an order-of-magnitude estimate of what the values of the K 's should be. Since the K 's are in units of energy/length, we must look for the characteristic energy and length in the problem. The only energy in the problem is the intermolecular inter-

action energy, which is estimated* to be ~ 0.01 eV, and the only suitable length is the separation between two molecules, which is ~ 10 Å. Therefore, $K \simeq 10^{-7}$ dyne, in order-of-magnitude agreement with measured values⁸ of 10^{-7} – 10^{-6} dyne. The K 's are also temperature dependent. In fact, it can be shown⁹ that the temperature dependence is of the form $K \sim \langle P_2(\cos \theta) \rangle^2$, where $\langle \rangle$ denotes averaging over that small volume of the sample that is characterized by a local director $\hat{n}(\vec{r})$, P_2 is the Legendre polynomial of second order, and θ is the angle between any molecule inside the volume where the average is taken, and the local director $\hat{n}(\vec{r}) \cdot \langle P_2(\cos \theta) \rangle$ is just the local order parameter measured with $\hat{n}(\vec{r})$ as the axis of symmetry. The dependence of the K 's on the square of the local order parameter is plausible if one thinks of the K 's as the macroscopic analog of the anisotropic intermolecular interaction constants, the difference being that, in place of molecules, we have small volumes of the sample with well-defined long-range orientational order. In such an analogy $\langle P_2(\cos \theta) \rangle$ plays the role of a (temperature-dependent) dipole strength of the molecules.

Suppose now the sample of nematic liquid crystal is placed under the influence of a magnetic or an electric field. Because the liquid crystal molecules are generally diamagnetic, electrically polarizable, and anisotropic in their magnetic and electric properties, the application of a field usually contributes an amount of free-energy density which is opposite in sign to that of the distortion free-energy density (because fields help align molecules). Let us first discuss the magnetic field contribution. Consider again a small region of the sample characterized by a local director $\hat{n}(\vec{r})$. The diamagnetic susceptibility per unit volume in such a small volume is usually anisotropic. Let χ_{\parallel} denote the susceptibility per unit volume parallel to $\hat{n}(\vec{r})$ and χ_{\perp} denote the susceptibility per unit volume perpendicular to $\hat{n}(\vec{r})$. The difference, $\Delta\chi \equiv \chi_{\parallel} - \chi_{\perp}$, is a measure of the local anisotropy. As shown in Ref. [6], $\Delta\chi$ is equal to $N \langle P_2(\cos \theta) \rangle (\xi_{\parallel} - \xi_{\perp})$, where N is the number of molecules per unit volume, $\langle P_2(\cos \theta) \rangle$ is the orientational order within the small region under consideration, and $\xi_{\parallel}(\xi_{\perp})$ is the diamagnetic susceptibility of a single rod-like molecule

* The intermolecular interaction energy responsible for the nematic ordering can be estimated from the latent heat of isotropic–nematic phase transition $\Delta E \simeq 300$ cal/mol $\simeq 0.01$ eV/molecule (see, for example, G. H. Brown, J. W. Doane, and D. D. Neff, *A Review of the Structure and Physical Properties of Liquid Crystals*, p. 43, CRC Press, Cleveland, Ohio, 1971).

parallel (perpendicular) to its long axis. In the following we will assume that $\chi_{\parallel} > \chi_{\perp}$ (i.e., positive anisotropy) and that the value of $\langle P_2(\cos \theta) \rangle$ is uniform throughout the volume of the sample, implying that $\Delta\chi$, K_{11} , K_{22} , and K_{33} have no spatial dependence. In

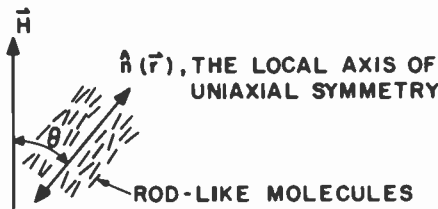


Fig. 2—Orientation of the local axis of uniaxial symmetry with respect to the external magnetic field direction.

Fig. 2 we show the relative directions of magnetic field \vec{H} and local director $\hat{n}(\vec{r})$. The induced diamagnetic moments per unit volume parallel and perpendicular to $\hat{n}(\vec{r})$ are, respectively,

$$\begin{aligned} M_{\parallel} &= H\chi_{\parallel}\cos\theta, \\ \bar{M}_{\perp} &= H\chi_{\perp}\sin\theta. \end{aligned}$$

The work done by the field per unit volume is

$$\begin{aligned} W_{\text{magnetic}} &= \int_0^H (-M_{\parallel}'\sin\theta - M_{\perp}'\cos\theta)dH' \\ &= -\frac{H^2}{2}(\chi_{\perp} + \Delta\chi\cos^2\theta). \end{aligned}$$

Discarding the spatially invariant term, $-H^2\chi_{\perp}/2$, we obtain the magnetic field contribution to the free-energy density

$$\mathfrak{F}_M = -\frac{\Delta\chi}{2}[\vec{H}\cdot\hat{n}(\vec{r})]^2. \quad [3]$$

Using similar arguments as above, we obtain the electric-field contribution to the free-energy density

$$\mathfrak{F}_E = -\frac{\Delta\epsilon}{8\pi}[\vec{E}\cdot\hat{n}(\vec{r})]^2, \quad [4]$$

where $\Delta\epsilon \equiv \epsilon_{\parallel} - \epsilon_{\perp}$ is the difference between the local dielectric con-

starts in directions parallel and perpendicular to the local director. Values of $\Delta\chi$ and $\Delta\epsilon$ typically range from 10^{-7} – 10^{-6} cgs units for $\Delta\chi$ and 0.1–1 for $\Delta\epsilon$.

At this point we make a slight generalization so that the theory can be applied to cholesteric liquid crystals as well. The basic difference between cholesteric and nematic liquid crystals lies in the fact that the equilibrium state of cholesterics is characterized by a nonvanishing twist in the director field. If we denote the cholesteric helical axis as the x -axis, the equilibrium state is characterized by

$$\begin{aligned}n_x &= 0, \\n_y &= \cos(\pi x/\lambda_0), \\n_z &= \sin(\pi x/\lambda_0),\end{aligned}$$

where λ_0 is the pitch of the helix. Using this representation of the director field, the twist term, $[\hat{n}(\vec{r}) \cdot \nabla \times \hat{n}(\vec{r})]^2$, is calculated to be $(\pi/\lambda_0)^2$. This suggests that the twist part of free-energy density for the cholesteric liquid crystals should be expanded around $|\hat{n}(\vec{r}) \cdot \nabla \times \hat{n}(\vec{r})| = \pi/\lambda_0$, where $||$ is the absolute value sign. In fact, it can be shown⁵ that the appropriate form is $||\hat{n}(\vec{r}) \cdot \nabla \times \hat{n}(\vec{r})| - \pi/\lambda_0|^2$.

We are now in a position to combine all the free-energy density terms to give a total free-energy density \mathcal{F} of the system under external fields:

$$\begin{aligned}\mathcal{F} &= \mathcal{F}_D + \mathcal{F}_M + \mathcal{F}_E \\&= \frac{1}{2} \left\{ K_{11} [\nabla \cdot \hat{n}(\vec{r})]^2 + K_{22} \left[\left| \hat{n}(\vec{r}) \cdot \nabla \times \hat{n}(\vec{r}) \right| - \frac{\pi}{\lambda_0} \right]^2 \right. \\&\quad \left. + K_{33} [\hat{n}(\vec{r}) \times \nabla \times \hat{n}(\vec{r})]^2 - \Delta\chi [\vec{H} \cdot \hat{n}(\vec{r})]^2 - \frac{1}{4\pi} \Delta\epsilon [E \cdot \hat{n}(\vec{r})]^2 \right\}. \quad [5]\end{aligned}$$

The total free energy of the sample is given by

$$F = \int_{\text{volume of the sample}} \mathcal{F} d^3r. \quad [6]$$

Eqs. [5] and [6] are the fundamental equations of the elastic continuum theory of nematic and cholesteric liquid crystals (for nematics λ_0 in Eq. [5] is set equal to ∞). In the following section we use the fundamental equations to solve four examples as illustrations for their applications.

3. Applications of the Elastic Continuum Theory

The basic principle involved in the application of the fundamental equations to the solution of actual problems is that the equilibrium state of the director field is always given by that director configuration that minimizes the free energy of the system with specified boundary conditions.

Before getting into actual calculations we first simplify Eq. [5] by setting $K_{11} = K_{22} = K_{33} = K$. This greatly facilitates the mathematics but does not affect the qualitative behavior of the results. Neglecting the term π/λ_0 for the moment, we have

$$\begin{aligned} \mathfrak{F} &= \frac{K}{2} \left\{ [\nabla \cdot \hat{n}(\bar{r})]^2 + [\hat{n}(\bar{r}) \cdot \nabla \times \hat{n}(\bar{r})]^2 + [\hat{n}(\bar{r}) \times \nabla \cdot \hat{n}(\bar{r})]^2 \right. \\ &\quad \left. - \frac{\Delta\chi}{K} [\bar{H} \cdot \hat{n}(\bar{r})]^2 - \frac{1}{4\pi} \frac{\Delta\epsilon}{K} [\bar{E} \cdot \hat{n}(\bar{r})]^2 \right\} \\ &= \frac{K}{2} \left\{ [\nabla \cdot \hat{n}(\bar{r})]^2 + [\nabla \times \hat{n}(\bar{r})]^2 - \frac{\Delta\chi}{K} [\bar{H} \cdot \hat{n}(\bar{r})]^2 \right. \\ &\quad \left. - \frac{1}{4\pi} \frac{\Delta\epsilon}{K} [\bar{E} \cdot \hat{n}(\bar{r})]^2 \right\}. \end{aligned} \quad [7]$$

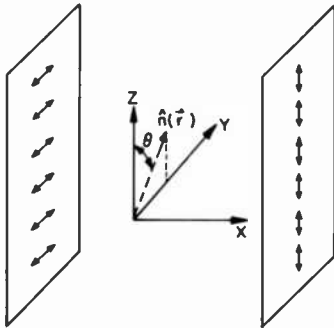


Fig. 3—The geometry of a 90°-twisted nematic cell.

3.1 Twisted Nematic Cell

In Fig. 3 we show a planar cell containing nematic liquid crystal, two of whose bounding walls are rubbed or otherwise treated so that the directors near the walls are pinned in the directions shown. Since the

directors at the two walls are perpendicular to each other, the local nematic directors must undergo a 90° twist in passing from one wall to the other. The question is how this twist is distributed across the cell, i.e., should the distribution be uniform or nonuniform? To answer this question, we must calculate the free energy of an arbitrary twist pattern with the specified boundary conditions. The correct twist pattern is then given by that director configuration that minimizes the free energy of the system. Assuming all the directors lie in the y - z plane, we write

$$\begin{aligned} n_x &= 0, \\ n_y &= \sin\theta(x), \\ n_z &= \cos\theta(x). \end{aligned}$$

From this representation of the director field, it is easily calculated that $\nabla \cdot \hat{n}(\vec{r}) = 0$ and $\nabla \times \hat{n}(\vec{r}) = (d\theta(x)/dx)[\sin\theta\hat{j} + \cos\theta\hat{k}]$, where we use $\hat{i}, \hat{j}, \hat{k}$ to denote the unit vectors in the x, y, z directions, respectively. Using Eqs. [6] and [7], we obtain

$$\begin{aligned} F &= \int d^3r \frac{K}{2} [\nabla \times \hat{n}(\vec{r})]^2 \\ &= \frac{K}{2} \int d^3r \left[\frac{d\theta(x)}{dx} \right]^2 \\ &= \frac{KA}{2} \int_{\text{thickness of the cell}} dx \left[\frac{d\theta(x)}{dx} \right]^2, \end{aligned} \quad [8]$$

where A is the area of the cell in the y - z plane. To minimize F , we recall that if one wants to minimize the value of an integral

$$I = \int_a^b G\left(y(x), \frac{dy(x)}{dx}, x\right) dx$$

by varying the functional form of $y(x)$, the optimal function $y(x)$ must satisfy the equation

$$\frac{\partial G}{\partial y} - \frac{d}{dx} \frac{\partial G}{\partial \left(\frac{dy}{dx}\right)} = 0, \quad [9]$$

which is called the Euler-Lagrange equation. In our present case θ corresponds to y , and $G = [d\theta(x)/dx]^2$; the application of Eq. [9]

yields $d^2\theta(x)/dx^2 = 0$, or $d\theta(x)/dx = C$, where C is an integration constant that can be determined by the boundary condition $C \times (\text{cell thickness}) = \pm\pi/2$ ($+\pi/2$ is indistinguishable from $-\pi/2$ for nematics). This is the result we are looking for. It tells us that the twist will be uniformly distributed across the cell. However, because $d\theta/dx$ can be either $+$ or $-$, the twist can be either left handed or right handed. In an actual 90° -twisted nematic cell, both senses of the twist are usually present, a fact that is indicated by the existence of visible disinclination lines separating regions of opposite senses of the twist.

3.2 Magnetic Coherence Length

The geometry of this problem is shown in Fig. 4. A semi-infinite sample of nematic liquid crystal with positive anisotropy is bound on one

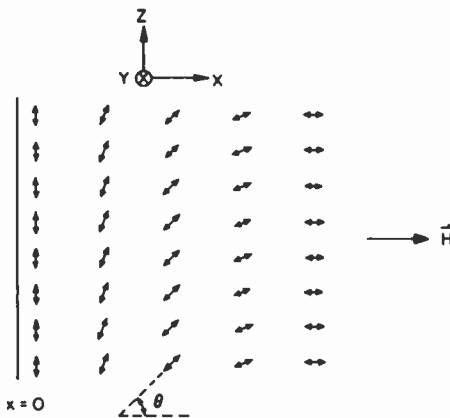


Fig. 4—Distortion of the director field when the molecules are pinned to the wall perpendicular to the external magnetic field direction. The nematic molecules are assumed to be diamagnetic with positive anisotropy.

side by a wall that is treated so that the directors near the wall are pinned along the z -direction. A magnetic field is applied along the x -axis, so that far away from the wall the directors would lie along the field direction. There is a transition region near the wall where the directors gradually change from one direction to the other. The problem is to find the characteristic length of that transition region. From

Fig. 4 we have

$$\begin{aligned} n_x &= \cos\theta(x), \\ n_y &= 0, \\ n_z &= \sin\theta(x). \end{aligned}$$

Straightforward calculation gives

$$\begin{aligned} [\nabla \cdot \hat{n}(\vec{r})]^2 &= \sin^2\theta \left[\frac{d\theta(x)}{dx} \right]^2, \\ [\nabla \times \hat{n}(\vec{r})]^2 &= \cos^2\theta \left[\frac{d\theta(x)}{dx} \right]^2, \\ -\frac{\Delta\chi}{K} [\hat{H} \cdot \hat{n}(\vec{r})]^2 &= -\frac{\Delta\chi}{K} [H \cos\theta(x)]^2. \end{aligned}$$

Substitution into Eq. [7] yields

$$\frac{F}{A} = \frac{K}{2} \int_0^{\infty} dx \left(\left[\frac{d\theta(x)}{dx} \right]^2 - \frac{\Delta\chi}{K} [H \cos\theta(x)]^2 \right). \quad [10]$$

where A is the area of the bounding wall. Application of the Euler-Lagrange equation to Eq. [10] gives an equation for the $\theta(x)$ that minimizes the free energy of the system:

$$\frac{K}{H^2 \Delta\chi} \frac{d^2\theta(x)}{dx^2} - \sin\theta \cos\theta = 0. \quad [11]$$

The combination $K/(H^2 \Delta\chi)$ has the dimension of (length)². We define

$$\xi_M = \frac{1}{H} \sqrt{\frac{K}{\Delta\chi}} \quad [12]$$

as the characteristic distance of the problem. Eq. [11] can now be rewritten as

$$\begin{aligned} \frac{\sin\theta \cos\theta}{\xi_M^2} \frac{d\theta}{dx} &= \frac{d^2\theta}{dx^2} \frac{d\theta}{dx} = \frac{1}{2} \frac{d}{dx} \left(\frac{d\theta}{dx} \right)^2 \\ \frac{\sin\theta d\sin\theta}{\xi_M^2 dx} &= \frac{1}{2} \frac{d}{dx} \left(\frac{d\theta}{dx} \right)^2 \end{aligned}$$

or

$$\frac{1}{2} \frac{1}{\xi_M^2} \frac{d \sin^2\theta}{dx} = \frac{1}{2} \frac{d}{dx} \left(\frac{d\theta}{dx} \right)^2 \quad [13]$$

Integration of Eq. [13] yields

$$\left(\frac{d\theta}{dx}\right)^2 = \left(\frac{\sin\theta}{\xi_M}\right)^2 + C.$$

The constant of integration is fixed by the condition that as $x \rightarrow \infty$, $\theta \rightarrow 0$ and $d\theta/dx \rightarrow 0$. Therefore $C = 0$, and

$$\frac{d\theta}{dx} = \pm \frac{\sin\theta}{\xi_M}.$$

Choosing the $-$ sign for $x > 0$ and integrating once more, we have

$$\ln\left(\tan\frac{\theta}{2}\right) = -\frac{x}{\xi_M},$$

or

$$\theta(x) = 2 \arctan[\exp\{-x/\xi_M\}], \text{ where } x = 0. \quad [14]$$

Eq. [14] is plotted in Fig. 5. As we can see, ξ_M is the characteristic length scale below which the magnetic field does not have much in-

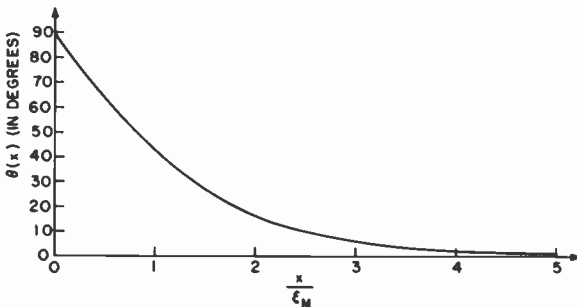


Fig. 5—Tilt angle (deviation from the field direction) of the director field plotted as a function of distance from the wall. The distance is measured in units of magnetic coherence length, which is the characteristic length of magnetic phenomena in nematic liquid crystals.

fluence on the relative orientations of the directors. Another way of saying the same thing is that ξ_M defines the scale of magnetic phenomena. ξ_M is usually called the "magnetic coherence length." For $K \sim 10^{-6}$ dyne, $\Delta\chi \sim 10^{-7}$ cgs units, and $H \sim 10\text{kOe}$, ξ_M is about $3 \mu\text{m}$.

Suppose now that in place of the magnetic field an electric field is applied. If impurity conduction and other dynamical effects are neglected, the problem is qualitatively the same, and a quantity ξ_E can be obtained which is the exact analog of ξ_M . Substitution of $\Delta\epsilon/4\pi$ for $\Delta\chi$ and E for H in Eq. [12] gives

$$\xi_E = \frac{1}{E} \sqrt{\frac{4\pi K}{\Delta\epsilon}}. \quad [15]$$

Setting $\xi_M = \xi_E$, we can compare the relative effectiveness of magnetic and electric fields in orienting the nematic directors. The relation is

$$E = \sqrt{\frac{4\pi\Delta\chi}{\Delta\epsilon}} H. \quad [16]$$

Taking $H = 1$ Oe, $\Delta\chi \sim 10^{-7}$ cgs unit, and $\Delta\epsilon \sim 0.1$, we have

$$E = \sqrt{\frac{4\pi\Delta\chi}{\Delta\epsilon}} H \simeq \sqrt{10^{-5}} H \simeq \frac{1}{300} \frac{\text{statvolt}}{\text{cm}} = 1 \text{ V/cm}.$$

Therefore, one oersted of magnetic field is equivalent to the order of one volt/cm of electric field in terms of effectiveness in orienting the nematic liquid crystals.

3.3 Fréedericksz Transition

Consider a planar cell of nematic liquid crystal with directors on both surfaces anchored perpendicular to the walls as shown in Fig. 6. It was first observed by Fréedericksz¹⁰ in 1927 that such a cell would undergo an abrupt change in its optical properties when the strength of an external magnetic field, applied normal to the director (z -direction in Fig. 6), exceeded a well-defined threshold. (In the original experiment one wall of the cell was concave in shape so as to give some variation in the cell thickness.) Fréedericksz further noted that the strength of the magnetic field at threshold was inversely proportional to the cell thickness d .¹¹ This Fréedericksz transition is now a well-studied phenomenon, and has found applications in liquid-crystal display devices. The transition is essentially due to the magnetic alignment of the bulk sample directors at sufficiently high field strength. However, both the abruptness of its onset and the relationship between the threshold field strength and the cell thickness are of theoretical and practical interest. Here we will use the continuum

theory to calculate the various properties of the Fréedericksz transition. From Fig. 6 we get

$$\begin{aligned}n_x &= \cos\theta(x), \\n_y &= 0, \\n_z &= \sin\theta(x).\end{aligned}$$

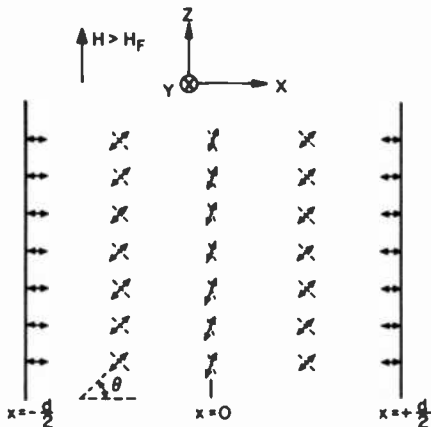


Fig. 6—Local nematic directors in a Fréedericksz cell when $H > H_F$. Dotted lines indicate the equivalent tilt configuration of the directors. Tilt angle θ is defined as shown.

From these expressions one obtains

$$[\nabla \cdot \hat{n}(\vec{r})]^2 + [\nabla \times \hat{n}(\vec{r})]^2 = \left[\frac{d\theta(x)}{dx} \right]^2,$$

and

$$-\frac{\Delta\chi}{K} [H \cdot \hat{n}(\vec{r})]^2 = -\frac{\Delta\chi}{K} H^2 \sin^2\theta.$$

Substitution into Eq. [7] and application of the Euler-Lagrange equation results in

$$\xi_M^2 \frac{d^2\theta}{dx^2} + \sin\theta \cos\theta = 0. \quad [17]$$

Using the same manipulations as those for Eq. [11], we get

$$\left(\frac{d\theta}{dx}\right)^2 = C - \frac{\sin^2\theta}{\xi_M^2}. \quad [18]$$

The constant of integration C is obtained by noting that, from the symmetry of the problem, $d\theta/dx = 0$ at $x = 0$. Defining $\theta(x = 0)$ as θ_M , we get $C = \sin^2\theta_M/\xi_M^2$, and

$$\frac{d\theta}{dx} = \pm \frac{1}{\xi_M} \sqrt{\sin^2\theta_M - \sin^2\theta}, \quad [19]$$

where the + sign corresponds to the solution in region $x < 0$ and the - sign corresponds to the solution in region $x > 0$. Since the solution is symmetric about $x = 0$, we will choose the + sign in the following calculations. Integration of Eq. [19] yields

$$\int_{-\frac{d}{2}}^x \frac{dx}{\xi_M} = \int_0^{\theta(x)} \frac{d\theta'}{\sqrt{\sin^2\theta_M - \sin^2\theta'}},$$

or

$$\frac{1}{\xi_M} \left(\frac{d}{2} + x \right) \sin\theta_M = \int_0^{\theta(x)} \frac{d\theta'}{\sqrt{1 - \left[\frac{\sin\theta'}{\sin\theta_M} \right]^2}}, \quad [20]$$

where $-d/2 \leq x \leq 0$. The solution of Eq. [20] will proceed in two steps. First θ_M will be determined as a function of ξ_M (or of H , since $\xi_M \equiv \sqrt{K/\Delta\chi}/H$). Then this $\theta_M(H)$ can be substituted back into Eq. [20] for the solution of $\theta(x)$ as a function of H .

From the definition of θ_M we get

$$\frac{d}{2\xi_M} \sin\theta_M = \int_0^{\theta_M} \frac{d\theta'}{\sqrt{1 - \left(\frac{\sin\theta'}{\sin\theta_M} \right)^2}}. \quad [21]$$

This equation can be solved graphically as in Fig. 7 by plotting, as a function of $\sin\theta_M$, the left- and right-hand sides on the same graph and locating the points of intersection. By expanding the integral on the right-hand side of Eq. [21], denoted here as $L(\sin\theta_M)$, for small values of θ_M , we get the slope

$$\left. \frac{dL(\sin\theta_M)}{d \sin\theta_M} \right|_{\theta_M = 0} = \frac{\pi}{2}.$$

Therefore, for $d/(2\xi_M) < \pi/2$ the only solution of Eq. [21] is $\theta_M = 0$.

However, when $d/(2\xi_M) > \pi/2$, a second solution with $\theta_M \neq 0$ is obtained that gives lower free energy than the $\theta_M = 0$ solution. The critical magnetic field H_F for the transition is found by equating $d/(2\xi_M)$

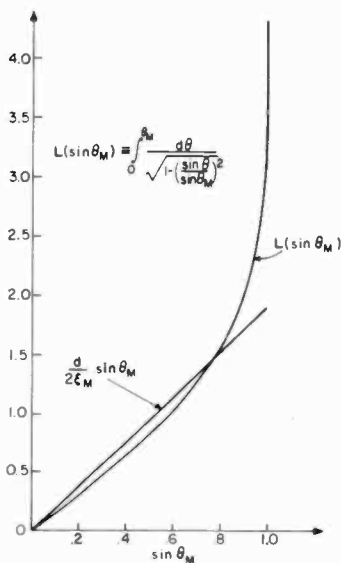


Fig. 7—Graphical solution of Eq. [21].

and $\pi/2$. Substitution of $\sqrt{K/\Delta\chi}/H$ for ξ_M gives

$$H_F = \sqrt{\frac{K}{\Delta\chi}} \frac{\pi}{d}, \quad [22]$$

which agrees with Fréedericksz's observation that the threshold field strength varies inversely with the thickness of the sample. The form of Eq. [22] can be understood by a simple plausibility argument. In section 3.2 we have seen that the magnetic coherence length ξ_M can be thought of as that length below which the magnetic field does not have much influence on the relative orientations of the directors. By applying this interpretation of ξ_M to our present example it is clear that only when $\xi_M < d/2$ would it be possible for the magnetic field to have significant influence on the orientations of the directors. Therefore, we would estimate

$$H_F \simeq \sqrt{\frac{K}{\Delta\chi}} \frac{2}{d},$$

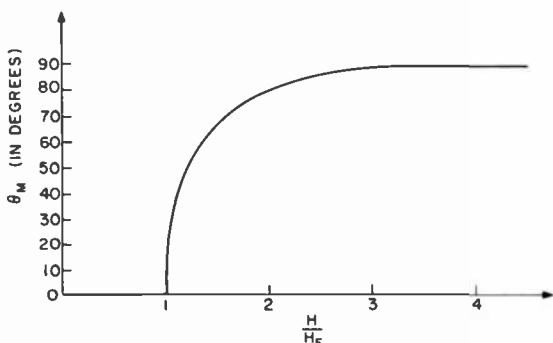


Fig. 8—Tilt angle of the directors at the center of Fréedericksz cell, θ_M , plotted as a function of reduced field H/H_F . For H/H_F slightly greater than 1, θ_M behaves as $\sim(H/H_F - 1)^{1/2}$.

which differs with the exact result only by a factor of $\pi/2$. In Fig. 8, θ_M is plotted as a function of H/H_F . For $H \sim H_F$, Eq. [21] can be expanded around $\theta_M = 0$ to give $\theta_M \propto (H - H_F)^{1/2}$.

Having obtained $\theta_M(H)$, we can now determine $\theta(x)$ as a function of H . By writing $d/2\xi_M = \pi H/2H_F$, Eq. [20] is put in the form

$$\frac{\pi H}{2 H_F} \left(1 + \frac{2x}{d} \right) \sin \theta_M = \int_0^{\theta(x)} \frac{d\theta'}{\sqrt{1 - \left(\frac{\sin \theta'}{\sin \theta_M} \right)^2}} \quad [23]$$

The right-hand side can be numerically integrated on computer, and the results $\theta(x)$ are plotted in Fig. 9 for three different values of H .

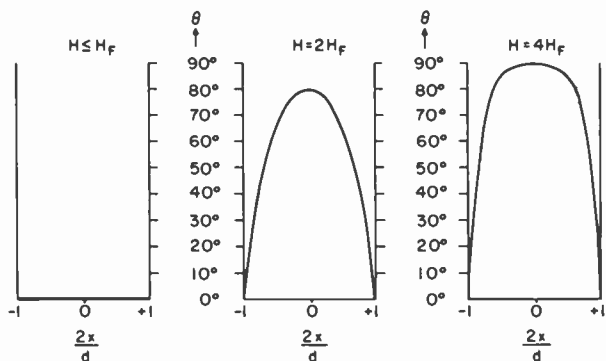


Fig. 9—Tilt angle of the directors plotted as a function of position in a Fréedericksz cell for three different magnetic field strengths.

The Fréedericksz transition can be induced by an electric field as well as by a magnetic field. The threshold electric field in that case is given by

$$E_F = \frac{\pi}{d} \sqrt{\frac{4\pi K}{\Delta\epsilon}}, \quad [24]$$

or

$$V_F = E_F d = \pi \sqrt{\frac{4\pi K}{\Delta\epsilon}}. \quad [25]$$

For $K \sim 10^{-6}$ dyne, $\Delta\chi \sim 10^{-7}$ cgs unit, $\Delta\epsilon \sim 0.1$, the critical magnetic field H_F is ~ 10 Oe for $d \sim 1$ cm, and the critical voltage is ~ 10 V, independent of cell thickness.

To conclude the discussion of the Fréedericksz transition, we note that for $H > H_F$ ($V > V_F$) there are two equivalent tilt configurations of the directors, denoted by the solid and the dotted lines in Fig. 6. In practice, for $H > H_F$ (or $V > V_F$) both tilt configurations are usually present, and regions of different tilt patterns are separated by visible disinclination lines.

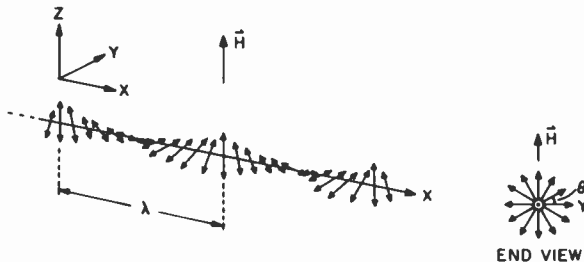


Fig. 10—Two views of the local directors in a cholesteric liquid crystal. In order to induce the cholesteric–nematic transition, a magnetic field H is applied perpendicular to the cholesteric helical axis. The angle θ used in the calculation is defined as shown.

3.4 Field-Induced Cholesteric–Nematic Transition

Consider a sample of cholesteric liquid crystal placed in a magnetic field H , with the field direction perpendicular to the cholesteric helical axis as shown in Fig. 10. From Eqs. [5], and [6], the free energy of the system over one period (or pitch) of the helix, λ , can be written as

$$\frac{F(\lambda)}{A} = \frac{K_{22}}{2} \int_0^\lambda dx \left\{ \left[\left| \widehat{n}(\bar{r}) \cdot \nabla \times \widehat{n}(\bar{r}) \right| - \frac{\pi}{\lambda_0} \right]^2 - \frac{\Delta\chi}{K_{22}} H^2 \sin^2\theta \right\}, \quad [26]$$

where A is the area of the sample in the y - z plane, assumed to be a constant, λ_0 is the pitch of the cholesteric helix at $H = 0$, θ is the angle between a local director and the y -axis as defined in Fig. 9, and $x = 0$ is defined by any point at which $\theta = 0$ (or π). With

$$\begin{aligned} n_x &= 0, \\ n_y &= \cos\theta(x), \\ n_z &= \sin\theta(x), \end{aligned}$$

we have

$$\widehat{n}(\bar{r}) \cdot \nabla \times \widehat{n}(\bar{r}) = \frac{d\theta(x)}{dx}$$

and

$$\frac{F(\lambda)}{A} = \frac{K_{22}}{2} \int_0^\lambda dx \left\{ \left[\frac{d\theta}{dx} - \frac{\pi}{\lambda_0} \right]^2 - \frac{\Delta\chi H^2 \sin^2\theta}{K_{22}} \right\}. \quad [27]$$

Here, we have to remember to take the absolute value of $d\theta/dx$. Application of the Euler-Lagrange equation yields

$$\xi_M^2 \frac{d^2\theta}{dx^2} + \sin\theta\cos\theta = 0,$$

which, as seen previously, can be put in the form

$$\left(\frac{d\theta}{dx} \right)^2 = \frac{1}{\xi_M^2} \left(\frac{1}{k^2} - \sin^2\theta \right). \quad [28]$$

where k^2 is an integration constant. At $H = 0$, it follows from Eq. [27] that $(d\theta/dx)$ equals a constant, (π/λ_0) . Therefore, k must behave as $\sim H$ for $H \rightarrow 0$ in order to cancel the H^2 from $1/\xi_M^2$ in Eq. [28]. Writing Eq. [28] in the form

$$\frac{d\theta}{dx} = \pm \frac{1}{k\xi_M} \sqrt{1 - k^2 \sin^2\theta}, \quad [28a]$$

we note that for finite values of H , $d\theta/dx$ is no longer a constant.

Plotting the z -component of the local director, $n_z = \sin\theta(x)$, as a function of position along the helical axis (x -axis) reveals that the sinusoidal pattern for $n_z(x)$ at $H = 0$ becomes distorted at finite values of H as shown in Fig. 11. The distortion makes $n_z(x)$ more square-wave-like and lengthens the pitch of the helix. Both of these effects can be understood on the basis that alignment along the magnetic

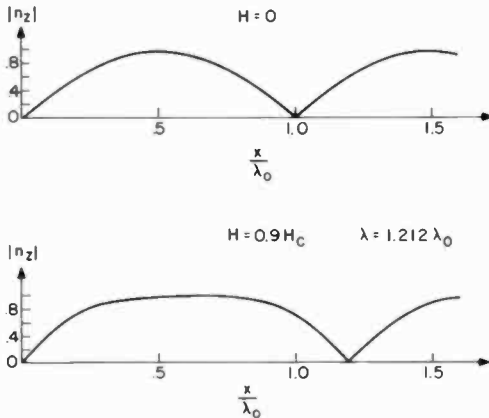


Fig. 11—Component of the cholesteric local director along the external field direction (z) for two different magnetic field strengths. Note that at finite field strength the helical pitch is lengthened and the sinusoidal shape of the curve at $H = 0$ is distorted, becoming more square-wave-like.

field direction lowers the energy of the system. The \pm signs for $d\theta/dx$ indicate the two possible senses of the helical twist. Since they are equivalent, we choose the $+$ sign in the following calculation. From the expression for $d\theta/dx$ we can get an expression for the pitch λ :

$$\begin{aligned} \lambda &= \int_0^\lambda dx = \int_0^\pi d\theta \frac{dx}{d\theta} = \int_0^\pi \frac{\xi_M k}{\sqrt{1 - k^2 \sin^2 \theta}} d\theta \\ &= 2\xi_M k \int_0^{\pi/2} \frac{d\theta}{\sqrt{1 - k^2 \sin^2 \theta}} \end{aligned} \quad [29]$$

At this point, it becomes necessary to know k^2 as a function of H . To do that, we must substitute Eq. [28a] back into Eq. [27] and minimize the average free-energy density by varying k^2 . Let us rewrite Eq. [27] as

$$g = \frac{2F(\lambda)}{q_0^2 K_{22} A \lambda} = \frac{1}{\lambda} \int_0^\pi d\theta \frac{dx}{d\theta} \left(\left[\frac{1}{q_0 \xi_M k} \sqrt{1 - k^2 \sin^2 \theta} - 1 \right]^2 - \frac{\sin^2 \theta}{q_0^2 \xi_M^2} \right), \quad [30]$$

where g is a dimensionless average free-energy density and $q_0 \equiv \pi/\lambda_0$. Substitution of Eq. [28a] for $dx/d\theta$ and expansion of the terms in the integrand gives

$$g = 1 - \frac{2\pi}{\lambda q_0} + \frac{2}{k \lambda^2 q_0^2} \int_0^\pi d\theta \sqrt{1 - k^2 \sin^2 \theta} - \frac{1}{k^2 q_0^2 \xi_M^2}. \quad [31]$$

Detailed steps leading from Eq. [30] to Eq. [31] are given in the Appendix. Differentiation of g with respect to k^2 yields

$$\begin{aligned} \frac{dg}{dk^2} &= \frac{2\pi}{\lambda^2 q_0} \frac{d\lambda}{dk^2} - \frac{2}{k \lambda^2 q_0} \frac{1}{\xi_M q_0} \frac{d\lambda}{dk^2} \int_0^\pi d\theta \\ &\times \sqrt{1 - k^2 \sin^2 \theta} + \frac{1}{k^4 q_0^2 \xi_M^2} - \frac{1}{k^4 q_0^2 \xi_M^2} \\ &= \frac{d\lambda}{dk^2} \frac{2}{\lambda^2 q_0} \left(\pi - \frac{1}{k \xi_M q_0} \int_0^\pi d\theta \sqrt{1 - k^2 \sin^2 \theta} \right). \end{aligned} \quad [32]$$

The desired equation for determining k as a function of H is obtained by setting $dg/dk^2 = 0$:

$$\xi_M q_0 = \sqrt{\frac{K_{22}}{\Delta \chi}} \frac{\pi}{H \lambda_0} = \frac{2}{\pi} \frac{1}{k} \int_0^{\frac{\pi}{2}} d\theta \sqrt{1 - k^2 \sin^2 \theta}. \quad [33]$$

Define

$$\begin{aligned} E_1(k) &\equiv \int_0^{\frac{\pi}{2}} \frac{d\theta}{\sqrt{1 - k^2 \sin^2 \theta}}, \\ E_2(k) &\equiv \int_0^{\frac{\pi}{2}} d\theta \sqrt{1 - k^2 \sin^2 \theta}. \end{aligned}$$

where E_1 and E_2 are the complete elliptic integrals of the first kind and the second kind, respectively. Eqs. [29] and [33] can be put in the form

$$\lambda = 2 \xi_M k E_1(k),$$

and

$$\frac{\pi \xi_M}{\lambda_0} = \frac{2}{k \pi} E_2(k),$$

Combining the two equations yields

$$\frac{\lambda}{\lambda_0} = \frac{4}{\pi^2} E_1(k) E_2(k). \quad [34]$$

$E_1(k)$ diverges at $k = 1$. Therefore, Eq. [34] has a singularity when

$$\frac{\xi_M \pi}{\lambda_0} = \frac{2}{\pi} E_2(1) = \frac{2}{\pi},$$

which defines a critical magnetic field

$$H_c = \sqrt{\frac{K_{22}}{\Delta \chi}} \frac{\pi^2}{2\lambda_0}. \quad [35]$$

If one takes $K_{22} \sim 10^{-6}$ dyne, $\Delta \chi \sim 10^{-6}$ cgs units, $\lambda_0 \sim 10^{-4}$ cm, H_c is ~ 50 kOe. A similar threshold can be obtained if the magnetic field is replaced by an electric field:

$$E_c = \sqrt{\frac{4\pi K_{22}}{\Delta \epsilon}} \frac{\pi^2}{2\lambda_0}. \quad [36]$$

Eqs. [29], [33], [34], and [35] were first obtained by de Gennes.¹² In terms of H_c , Eq. [33] can be put in the form

$$\frac{H_c}{H} k = E_2(k). \quad [33a]$$

For $H > H_c$ this equation has no solution. When $H < H_c$, the values of k ranges from 0 to 1 as plotted in Fig. 12. In Fig. 13 we show a plot of λ/λ_0 vs. H/H_c . At $H = H_c$ the pitch diverges and the cholesteric phase transforms into the nematic phase. Experimentally this curve is well verified.^{13,14}

Finally, it should be noted that if the field is initially applied parallel to the helical axis, the cholesteric helix would usually rotate at $H < H_c$ so as to make the field perpendicular to the helical axis. Therefore, the geometry shown in Fig. 10 is always the situation seen experimentally just before the field strength reaches the cholesteric-nematic transition threshold.¹⁴

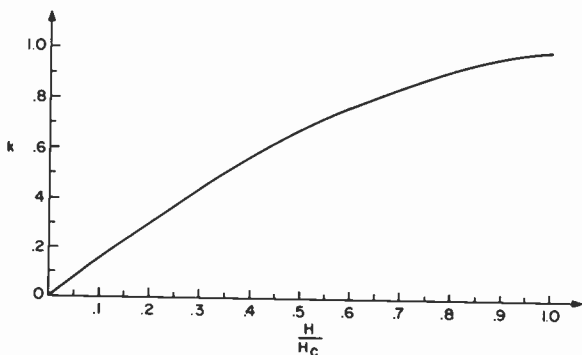


Fig. 12—Solution of Eq. [33a].

4. Concluding Remarks

The above discussion of the continuum theory of liquid crystals is by no means complete. There exist many more effects that can be described by the continuum theory, either in its present or modified form. In view of the diverse applications of the theory, the selection

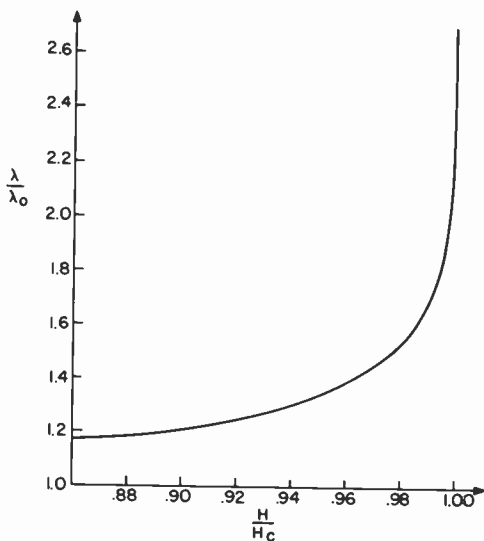


Fig. 13—Ratio of the helical pitch in finite field to the pitch in zero field, λ/λ_0 , plotted as a function of reduced field H/H_c . The divergence at $H/H_c = 1$ is logarithmic in nature.

of the four examples discussed in this paper is based on the consideration that they all have practical relevance to liquid-crystal display devices. It is hoped that their description by the continuum theory can, on the one hand, demonstrate the power and the flavor of the theory and, on the other hand, complement the discussion of the device physics aspects of these effects in other papers of this series.

Appendix

In this appendix we show the steps leading from Eq. [30] to Eq. [31]. From Eqs. [28a] and [30] we have

$$\begin{aligned}
 g &= \frac{1}{\lambda} \int_0^\pi d\theta \frac{k\xi_M}{\sqrt{1 - k^2 \sin^2 \theta}} \left\{ 1 - \frac{2\sqrt{1 - k^2 \sin^2 \theta}}{kq_0\xi_M} \right. \\
 &+ \left. \frac{1 - k^2 \sin^2 \theta}{k^2 q_0^2 \xi_M^2} - \frac{\sin^2 \theta}{q_0^2 \xi_M^2} \right\} \\
 &= \frac{k\xi_M}{\lambda} \int_0^\pi d\theta \frac{d\theta}{\sqrt{1 - k^2 \sin^2 \theta}} - \frac{2\pi}{\lambda q_0} + \frac{1}{k\lambda\xi_M q_0^2} \\
 &\times \int_0^\pi d\theta \sqrt{1 - k^2 \sin^2 \theta} - \frac{1}{q_0^2 \lambda \xi_M^2} \int_0^\lambda dx \sin^2 \theta. \quad [37]
 \end{aligned}$$

By writing $\sin^2 \theta = (1/k^2) - \xi_M^2 (d\theta/dx)^2$, the fourth term in Eq. [37] can be simplified as

$$\begin{aligned}
 -\frac{1}{q_0^2 \lambda \xi_M^2} \int_0^\lambda dx \sin^2 \theta &= -\frac{1}{k^2 q_0^2 \xi_M^2} + \frac{1}{q_0^2 \lambda} \int_0^\pi \left(\frac{d\theta}{dx} \right) d\theta \\
 &= -\frac{1}{k^2 q_0^2 \xi_M^2} + \frac{1}{k\lambda\xi_M q_0^2} \int_0^\pi d\theta \sqrt{1 - k^2 \sin^2 \theta} \quad [38]
 \end{aligned}$$

Therefore,

$$g = 1 - \frac{2\pi}{\lambda q_0} + \frac{2}{k\lambda\xi_M q_0^2} \int_0^\pi d\theta \sqrt{1 - k^2 \sin^2 \theta} - \frac{1}{k^2 q_0^2 \xi_M^2}. \quad [39]$$

References:

- 1 P. J. Wojtowicz, "Introduction to the Molecular Theory of Nematic Liquid Crystals," *RCA Review*, **35**, p. 105, March 1974.
- 2 P. J. Wojtowicz, "Generalized Mean Field Theory of Nematic Liquid Crystals," *RCA Review*, **35**, p. 118, March 1974.

- ³ H. Zocher, "The Effect of a Magnetic Field on the Nematic State," *Trans. Faraday Soc.*, **29**, p. 945 (1933).
- ⁴ C. W. Oseen, "The Theory of Liquid Crystals," *Trans. Faraday Soc.*, **29**, p. 883 (1933).
- ⁵ F. C. Frank, "On the Theory of Liquid Crystals," *Faraday Soc. Disc.*, **25**, p. 19 (1958).
- ⁶ E. G. Priestley, "Nematic Order: The Long Range Orientational Distribution Function," *RCA Review*, **35**, p. 144, March 1974.
- ⁷ P. Sheng, "Hard Rod Model of the Nematic-Isotropic Phase Transition," *RCA Review*, **35**, p. 132, March 1974.
- ⁸ P. G. de Gennes, *Lecture Notes on Liquid Crystal Physics*, Part I (1970).
- ⁹ See, for example, C. P. Fan and M. J. Stephen, "Isotropic-Nematic Phase Transition in Liquid Crystals," *Phys. Rev. Lett.*, **25**, p. 500 (1970).
- ¹⁰ V. Fréedericksz and A. Reppew, "Theoretisches und Experimentelles zur Frage nach der Natur der Anisotropen Flüssigkeiten," *Z. Physik*, **42**, p. 532 (1927).
- ¹¹ V. Fréedericksz and V. Zolina, "Forces Causing the Orientation of an Anisotropic Liquid," *Trans. Faraday Soc.*, **29**, p. 919 (1933).
- ¹² P. G. de Gennes, "Calcul de la Distorsion d'une Structure Cholesteric par un Champ Magnetique," *Solid State Comm.*, **6**, p. 163 (1968).
- ¹³ G. Durand, L. Leger, F. Rondelez, and M. Veysie, "Magnetically Induced Cholesteric-to-Nematic Phase Transition in Liquid Crystals," *Phys. Rev. Lett.*, **22**, p. 227 (1969).
- ¹⁴ R. B. Meyer, "Distortion of a Cholesteric Structure by a Magnetic Field," *Appl. Phys. Lett.*, **14**, p. 208 (1969).

Electrohydrodynamic Instabilities in Nematic Liquid Crystals

Dietrich Meyerhofer

RCA Laboratories, Princeton, N. J. 08540

Abstract—The threshold condition for the Williams-domain hydrodynamic instability in nematic liquid crystals is reviewed. A calculation of threshold voltage is performed that is a generalization of previous results. One simplifying assumption (fluid flow along the boundaries is finite) is used that allows an analytical solution as shown of the problem. It is shown that this assumption leads to only a small error. The threshold voltage and domain spacing are calculated for MBBA as function of frequency without any adjustable parameters and found to be in excellent agreement with experiment. The range of applicability of the conduction regime (Williams domains) is discussed.

Introduction

The best-known electrohydrodynamic instabilities in liquid crystals are the Williams domains.¹ They are observed when an electric field is applied to a thin layer of a nematic liquid crystal having negative dielectric anisotropy and sufficient electrical conductivity. They manifest themselves as a set of parallel straight lines separated by a constant distance that is approximately equal to the cell thickness. They appear above a well-defined threshold voltage and exist in their original form over only a small voltage range. At higher voltages, the pattern becomes more complicated and leads to heavily scattering turbulence (dynamic scattering).²

The structure of the domain instability is well-understood qualitatively.³ The liquid flows in cylindrical motion at right angles to the

domain walls, which represent the vortices of the motion. The hydrodynamic motion is not visible directly, but becomes manifest because of the anisotropy in index of refraction. The pattern is only visible for light polarized perpendicular to the domain walls, which means that the director (parallel to the optic axis) is located in the plane perpendicular to the walls. The flow and alignment pattern in this plane are sketched in Fig. 1, following Penz.³

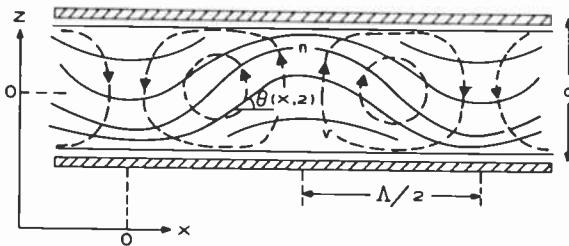


Fig. 1—Cross section through a liquid crystal cell at right angles to the domain lines. The solid lines indicate the director orientation n , the dashed lines represent the flow v .

It should be noted here that hydrodynamic instabilities are also possible in isotropic liquids. Examples are the interaction of thermal gradients and gravitational forces (Bénard's problem⁴) and electric-field-driven flow under space charge limited current conditions.⁵ The latter is the likely cause of flow that has been observed in liquid crystals above the nematic-isotropic transition⁶ (N-L point). In contrast to this, the instabilities discussed here depend on the anisotropic nature of the material parameters.

The nature of the Williams domain instability was explained by Helfrich who calculated the threshold voltage of domain formation for the case of dc voltage and one-dimensional geometry.⁷ The calculations were extended to ac fields by Dubois-Violette⁸ and to two-dimensional geometry by Penz and Ford.⁹ They show good qualitative agreement with measured thresholds.

In this paper we will extend the threshold calculations to show how the instability arises and to combine both frequency dependence and two-dimensional features. We will compare the results with measured values of threshold voltage and domain spacing as function of ac frequency.¹⁰ Good quantitative agreement will be demonstrated.

Nature of the Instability and the Balance of Forces

We now calculate the threshold of domain formation following the concepts of Helfrich.⁷ We consider a thin planar cell with electrodes on the two surfaces. We assume that the dielectric anisotropy is negative ($\Delta\epsilon = \epsilon_{\parallel} - \epsilon_{\perp} < 0$) and that the liquid crystal is aligned uniformly parallel to the surface by suitable surface treatment. The geometry is that of Fig. 1; the director lies in the x - z plane and is parallel to the x -axis at the surfaces. There is no variation in the y -direction and all variations in the x -direction are periodic with period Λ . In this geometry, the electric field alone does not distort the liquid and any instability must be of hydrodynamic nature.

To calculate the threshold, we assume a small fluctuation of the director $\theta(x, z)$ and calculate whether the fluctuation grows or decays in time. In the absence of applied fields, there is only an elastic torque (Γ_{elast}), which tends to restore the uniform alignment. An applied electric field in the z -direction produces two kinds of forces. First, there is a purely dielectric restoring torque (Γ_{diel}) due to $\Delta\epsilon < 0$. Second, the anisotropy in the conductivity produces a charge separation (similar to the Hall effect) through which the applied field exerts a force on the mass of the liquid causing it to flow. The nonuniformity of the flow (shear) produces a torque on the director (Γ_{visc}) that is in such a direction as to increase the fluctuation. The magnitude of Γ_{diel} and Γ_{visc} both increase as the square of the applied field so that, if $|\Gamma_{\text{visc}}|$ is larger than $|\Gamma_{\text{diel}}|$, there will exist a field at which $|\Gamma_{\text{visc}} + \Gamma_{\text{diel}}|$ is larger than $|\Gamma_{\text{elast}}|$ and the alignment will become unstable.

In calculating the torque, we make the assumption that $\theta \ll \pi/2$. This will lead to linearized equations and all torques will be proportional to θ . This permits an accurate calculation of the threshold, but does not allow the determination of the distortion above threshold for which higher order terms in θ are required.

Dielectric Response

Apply an external field $E^0 = V/d$. Thus, the field in the sample is given by $\mathbf{E} = (E_x, 0, E^0 + E_z')$ where $E_x, E_z' \ll E^0$. Because $\nabla \times \mathbf{E} = -\partial B/\partial t = 0$,

$$\frac{\partial E_x}{\partial z} = \frac{\partial E_z}{\partial x} = \frac{\partial E_z'}{\partial x} \quad [1]$$

The director \mathbf{n} lies in the (x, z) plane at angle θ to the x axis, so $\mathbf{n} =$

$(\cos\theta, 0, \sin\theta) \approx (1, 0, \theta)$. The dielectric and conductivity tensors (ϵ , σ) are both uniaxial and parallel to \mathbf{n} , and are given by

$$\epsilon_{ij} = \epsilon_{\perp} \delta_{ij} + \Delta\epsilon n_i n_j \quad [2]$$

$$\Delta\epsilon = \epsilon_{\parallel} - \epsilon_{\perp}$$

with an identical relationship for σ . If we keep only first order terms in θ , E_x , E_z' , we obtain

$$D_x = \epsilon_{\perp} E_x + \Delta\epsilon \theta E_z = \epsilon_{\perp} E_x + \Delta\epsilon \theta E^{\circ} \quad [3]$$

$$D_z = \Delta\epsilon \theta E_x + \epsilon_{\parallel} E_z = \epsilon_{\perp} E^{\circ} + \epsilon_{\parallel} E_z'$$

$$j_x = \sigma_{\perp} E_x + \Delta\sigma \theta E^{\circ} \quad [4]$$

$$j_z = \sigma_{\parallel} E^{\circ} + \sigma_{\perp} E_z'$$

The free charge is given by

$$\rho = \nabla \cdot \mathbf{D} = \epsilon_{\perp} \frac{\partial E_x}{\partial x} + \Delta\epsilon E^{\circ} \frac{\partial \theta}{\partial x} + \epsilon_{\parallel} \frac{\partial E_z'}{\partial z} \quad [5]$$

and from the charge continuity equation

$$-\frac{\partial \rho}{\partial t} = \nabla \cdot \mathbf{j} = \sigma_{\perp} \frac{\partial E_x}{\partial x} + \Delta\sigma E^{\circ} \frac{\partial \theta}{\partial x} + \sigma_{\parallel} \frac{\partial E_z'}{\partial z} \quad [6]$$

Eqs. [1], [5], and [6] define E_x , E_z' , and ρ in terms of E_0 and $d\theta/dx$.

Hydrodynamic Effects

The hydrodynamic equations describe the relationships between the applied forces and the fluid velocities. As given by Leslie,¹¹ in linear approximation, they are

$$F_i + \sum_j \frac{\partial \sigma_{ij}'}{\partial x_j} = 0 \quad [7]$$

for the isothermal, steady-state case. Here, \mathbf{F} is the applied body force

$$\mathbf{F} = \rho \mathbf{E} = \rho(0, 0, E^{\circ}) \quad [8]$$

and σ' is the viscous stress tensor (σ'_{ij} is as defined by Penz⁹). For an

incompressible fluid, there is the additional requirement

$$\nabla \cdot \mathbf{v} = 0, \quad [9]$$

where \mathbf{v} is the fluid velocity.

The viscous tensor as obtained from thermodynamic considerations and symmetry properties is defined in terms of velocity gradients and director orientations as

$$\begin{aligned} \sigma_{ij}' = & -p\delta_{ij} + \alpha_1 \sum_{kl} n_k n_l A_{kl} n_i n_j + \alpha_2 n_j N_i + \alpha_3 n_i N_j \\ & + \alpha_4 A_{ij} + \alpha_5 \sum_k n_j n_k A_{ki} + \alpha_6 \sum_k n_i n_k A_{kj}, \end{aligned} \quad [10]$$

where

$$\begin{aligned} A_{ij} &= \frac{1}{2} \left(\frac{\partial v_i}{\partial x} + \frac{\partial v_j}{\partial x_i} \right), \\ N &= -\frac{1}{2} [\nabla \times \mathbf{v}] \times \mathbf{n}, \end{aligned} \quad [11]$$

p is the hydrostatic pressure, and the α_i 's are the viscosity coefficients. The velocity gradients are assumed small, so that the only non-zero terms are

$$\begin{aligned} A_{xx} &= \frac{\partial v_x}{\partial x}, \quad A_{xz} = A_{zx} = \frac{1}{2} \left(\frac{\partial v_x}{\partial z} + \frac{\partial v_z}{\partial x} \right), \\ A_{zz} &= \frac{\partial v_z}{\partial z}, \quad N_z = \frac{1}{2} \left(\frac{\partial v_x}{\partial z} - \frac{\partial v_z}{\partial x} \right) \end{aligned}$$

and

$$\begin{aligned} \sigma_{xx}' &= (\alpha_1 + \alpha_4 + \alpha_5 + \alpha_6) \frac{\partial v_x}{\partial x} \\ \sigma_{xz}' &= \frac{1}{2} (-\alpha_3 + \alpha_4 + \alpha_6) \frac{\partial v_z}{\partial x} + \frac{1}{2} (\alpha_3 + \alpha_4 + \alpha_6) \frac{\partial v_x}{\partial z} \\ \sigma_{zx}' &= \frac{1}{2} (-\alpha_2 + \alpha_4 + \alpha_5) \frac{\partial v_z}{\partial x} + \frac{1}{2} (\alpha_2 + \alpha_4 + \alpha_5) \frac{\partial v_x}{\partial z} \\ \sigma_{zz}' &= \alpha_4 \frac{\partial v_x}{\partial z}. \end{aligned} \quad [12]$$

Inserting Eqs. [8] and [12] into Eq. [7], we obtain

$$\begin{aligned}
 -F_x = 0 = \frac{\partial \sigma_{xx}'}{\partial x} + \frac{\partial \sigma_{xz}'}{\partial z} = -\frac{\partial p}{\partial x} + (\alpha_1 + \alpha_4 + \alpha_5 + \alpha_6) \frac{\partial^2 v_x}{\partial x^2} \\
 + \frac{1}{2}(-\alpha_3 + \alpha_4 + \alpha_6) \frac{\partial^2 v_z}{\partial x \partial z} + \frac{1}{2}(\alpha_3 + \alpha_4 + \alpha_6) \frac{\partial^2 v_x}{\partial z^2} \quad [13]
 \end{aligned}$$

$$\begin{aligned}
 -F_z = -\rho E_0 = \frac{\partial \sigma_{zx}'}{\partial x} + \frac{\partial \sigma_{zz}'}{\partial z} = -\frac{\partial p}{\partial z} + \alpha_4 \frac{\partial^2 v_z}{\partial z^2} + \frac{1}{2}(-\alpha_2 + \alpha_4 \\
 + \alpha_5) \frac{\partial^2 v_z}{\partial x^2} + \frac{1}{2}(\alpha_2 + \alpha_4 + \alpha_5) \frac{\partial^2 v_x}{\partial x \partial z}. \quad [14]
 \end{aligned}$$

Eqs. [9], [13], and [14] can be solved for v_x , v_z , and p in terms of ρ which was previously defined in terms of $d\theta/dx$.

The Boundary Value Problem in the Conduction Regime

The boundary conditions of the two-dimensional problem are that θ , E_x , v_x , and v_z all must be zero at the electrodes ($z = \pm d/2$). Penz and Ford⁹ have solved the various equations for these boundary conditions in the dc case. The solution had to be obtained numerically, which obscures the physical processes.

We can obtain a much simpler solution by relaxing one boundary condition and letting v_x be finite at the electrode. While this can not be the case in practice, due to viscous forces, we will show below that the approximation is a good one. Penz³ demonstrated experimentally that the distortion of the director above the Williams domain threshold may be described as

$$\theta = \theta^0 \sin q_x x \cos q_z z, \quad [15]$$

where $q_z = \pi/d$, $q_x = 2\pi/\Lambda$. This is the pattern plotted in Fig. 1. By inspection, and by making use of Eqs. [1] and [9], we can write the simplest trial functions

$$\begin{aligned}
 E_x &= E_x' \sin q_x x \cos q_z z \\
 E_z' &= S E_x' \cos q_x x \sin q_z z \\
 v_x &= S v_z' \sin q_x x \sin q_z z \\
 v_z &= v_z' \cos q_x x \cos q_z z
 \end{aligned} \quad [16]$$

where $S = q_z/q_x = \Lambda/2d$. The corresponding flow pattern is indicated in Fig. 1 (the figure anticipates v_z' being negative).

Inserting the values of E_x and E_z' in Eqs. [5] and [6] and solving for ρ , one obtains

$$\rho + \frac{\epsilon_1 + S^2\epsilon_1}{\sigma_1 + S^2\sigma_1} \frac{\partial \rho}{\partial t} = \left[\Delta\epsilon - \frac{\epsilon_1 + S^2\epsilon_1}{\sigma_1 + S^2\sigma_1} \Delta\sigma \right] E^0 \theta^0 q_x \cos q_x \cos q_z. \quad [17]$$

Let the applied field be sinusoidal,

$$E^0 = \sqrt{2} E_0 \cos \omega t. \quad [18]$$

and assume that θ and \mathbf{v} are independent of time. This defines the *conduction regime* of Dubois-Violette et al⁸ in which Williams domains can exist. Thus Eq. [17] is solved to obtain

$$\rho = -\tau \sigma_H \sqrt{2} E_0 \frac{\cos \omega t + \omega \tau \sin \omega t}{1 + \omega^2 \tau^2} q_x \theta^0 \cos q_x \cos q_z, \quad [19]$$

where

$$\tau = \frac{\epsilon_1 + S^2\epsilon_1}{\sigma_1 + S^2\sigma_1}; \quad \sigma_H = \Delta\sigma - \frac{\Delta\epsilon}{\tau}$$

in the notation of Dubois-Violette. τ is the equivalent dielectric relaxation time.

Inserting Eqs. [18] and [19] into Eq. [5], one obtains

$$E_x' = -\frac{\tau \sigma_H \frac{\cos \omega t + \omega \tau \sin \omega t}{1 + \omega^2 \tau^2} + \Delta\epsilon \cos \omega t}{\epsilon_1 + S^2\epsilon_1} \sqrt{2} E_0 \theta^0, \quad [20]$$

the desired relationship between E_x and θ .

Next, we insert Eq. [16] into Eqs. [13] and [14] and eliminate ρ to obtain

$$q_x^3 \eta_1 + (\alpha_1 + \eta_1 + \eta_2) S^2 + \eta_2 S^4 \{v_z' \sin q_x \cos q_z\} = -E_0 \frac{\partial \rho}{\partial x}. \quad [21]$$

where $\eta_1 = \frac{1}{2}(-\alpha_2 + \alpha_4 + \alpha_5)$, $\eta_2 = \frac{1}{2}(\alpha_3 + \alpha_4 + \alpha_6)$ are the Helfrich viscosity parameters (Penz and Ford⁹ use the same notation, but interchange η_1 and η_2). The left-hand side of Eq. [21] is time independent, so the right-hand side can be averaged over time (after inserting Eq. [19]) to obtain

$$-\tau\sigma_H E_0^2 (q_x^2 \theta^2 \sin q_x x \cos q_z z) \frac{1}{1 + \omega^2 \tau^2}.$$

Therefore,

$$v_z' = \frac{-\theta^2 E_0^2}{q_x [(1 + S^2)(\eta_1 + S^2 \eta_2) + S^2 \alpha_1]} \frac{\tau \sigma_H}{1 + \omega^2 \tau^2}. \quad [22]$$

The Torque Balance Equation

We can now calculate the various torques acting on the director. Because of the two-dimensional geometry, only the y -component of the torque is non-zero. The dielectric and elastic torques are obtained most easily by taking the functional derivative of the free energy with respect to θ .⁸

$$\Gamma_y = \frac{-\partial F}{\partial \theta} \quad [23]$$

The elastic free energy is given by Frank¹² as

$$\begin{aligned} F_{\text{elast}} &= \frac{1}{2} [k_{11} (\nabla \cdot \mathbf{n})^2 + k_{22} (\mathbf{n} \cdot \nabla \times \mathbf{n})^2 + k_{33} (\mathbf{n} \times \nabla \times \mathbf{n})^2] \\ &= \frac{k_{11}}{2} \left(\frac{\partial n_x}{\partial x} + \frac{\partial n_z}{\partial z} \right)^2 + \frac{k_{33}}{2} \left(\frac{\partial n_x}{\partial z} - \frac{\partial n_z}{\partial x} \right)^2. \end{aligned} \quad [24]$$

Inserting the values for \mathbf{n} , and keeping only linear terms,

$$\begin{aligned} \Gamma_{\text{elast},y} &= - \left(k_{11} \frac{\partial^2 \theta}{\partial z^2} + k_{33} \frac{\partial^2 \theta}{\partial x^2} \right) \\ &= q_x^2 (k_{33} + S^2 k_{11}) \theta_0 \sin q_x x \cos q_z z. \end{aligned} \quad [25]$$

This is a restoring torque ($\Gamma/\theta > 0$), i.e., it tends to decrease θ_0 .

The dielectric free energy is

$$F_{\text{die}} = \frac{1}{2} \mathbf{E} \cdot \mathbf{D}. \quad [26]$$

Making use of Eq. [2] and the exact value of $\mathbf{n} = (\cos\theta, 0, \sin\theta)$, one obtains

$$\Gamma_{\text{die},y} = -\Delta \epsilon E_z (E_x + E_z \theta). \quad [27]$$

Inserting Eqs. [15] and [20] into Eq. [27] and averaging over time, one obtains

$$\begin{aligned} \Gamma_{\text{diel},y} &= -\Delta\epsilon E_0^2 \left\{ \frac{-\tau\sigma_H(1 + \omega^2\tau^2)^{-1} + \Delta\epsilon}{\epsilon_1 + S^2\epsilon_\perp} + 1 \right\} \theta_0 \sin q_x x \cos q_z z \\ &= -\Delta\epsilon E_0^2 \left\{ \frac{\tau\sigma_H}{\epsilon_1 + S^2\epsilon_\perp} \frac{\omega^2\tau^2}{1 + \omega^2\tau^2} \right. \\ &\quad \left. + (1 + S^2) \frac{\sigma_\perp}{\sigma_1 + S^2\sigma_\perp} \right\} \theta_0 \sin q_x x \cos q_z z \end{aligned} \quad [28]$$

for $\Delta\epsilon < 0$, $\Gamma/\theta > 0$, and this is also a restoring torque as predicted.

The viscous torque that the flow exerts on the director is given by^{9,13}

$$\begin{aligned} \Gamma_{\text{visc},y} &= \sigma_{xz}' - \sigma_{zx}' \\ &= \frac{1}{2}(\alpha_2 - \alpha_3 + \alpha_6 - \alpha_5) \frac{\partial v_z}{\partial x} + \frac{1}{2}(\alpha_3 - \alpha_2 + \alpha_6 - \alpha_5) \frac{\partial v_x}{\partial z} \\ &= -K_1 \frac{\partial v_z}{\partial x} + K_2 \frac{\partial v_x}{\partial z} \quad [29] \\ &= q_x v_z' (K_1 + S^2 K_2) \sin q_x x \cos q_z z, \\ &= -\frac{E_0^2 (K_1 + S^2 K_2)}{\eta_1 + (\alpha_1 + \eta_1 + \eta_2) S^2 + \eta_2 S^4} \frac{\tau\sigma_H}{1 + \omega^2\tau^2} \theta_0 \sin q_x x \cos q_z z. \end{aligned}$$

where Eq. [22] has been used. K_1 and K_2 are the combinations of viscosity parameters Helfrich⁷ calls the shear-torque coefficients. If the Parodi relationship¹³ ($\alpha_6 - \alpha_5 = \alpha_2 + \alpha_3$) is used, they become

$$K_1 = -\alpha_2, \quad K_2 = \alpha_3. \quad [30]$$

Since K_1 is larger than K_2 and positive, $\Gamma_{\text{visc}}/\theta < 0$ and this can be seen to be the driving torque.

All three torques have the same spatial dependence and are proportional to θ . This confirms that our set of trial functions, Eqs. [16], are consistent. The threshold for domain formation may now be calculated by setting the sum of the torques equal to zero. After some rearrangement,

$$\begin{aligned} \frac{E_0^2}{q_x^2} &= [(k_{33} + S^2 k_{11})(1 + \omega^2\tau^2)] \left[\frac{(K_1 + S^2 K_2)(1 + S^2)}{(1 + S^2)(\eta_1 + S^2\eta_2) + S^2\alpha_1} \right. \\ &\quad \left. + \frac{\sigma_x\epsilon_\perp - \sigma_\perp\epsilon_x}{\sigma_1 + S^2\sigma_\perp} + \Delta\epsilon \frac{(1 + S^2)\sigma_\perp}{\sigma_1 + S^2\sigma_\perp} + \omega^2\tau^2 \Delta\epsilon \frac{(1 + S^2)\epsilon_\perp}{\epsilon_1 + S^2\epsilon_\perp} \right]^{-1}. \end{aligned} \quad [31]$$

where

$$\tau = \frac{\epsilon_{\parallel} + S^2 \epsilon_{\perp}}{\sigma_{\parallel} + S^2 \sigma_{\perp}}$$

Eq. [31] has been cast in this form to allow comparison with previous work. If $\omega = 0$, Eq. [31] of Penz and Ford⁹ is obtained (α_{\parallel} is very small or zero); if $\omega = 0$ and $S = 0$, Eq. [5.2] of Helfrich;⁷ and if $S = 0$, Eq.

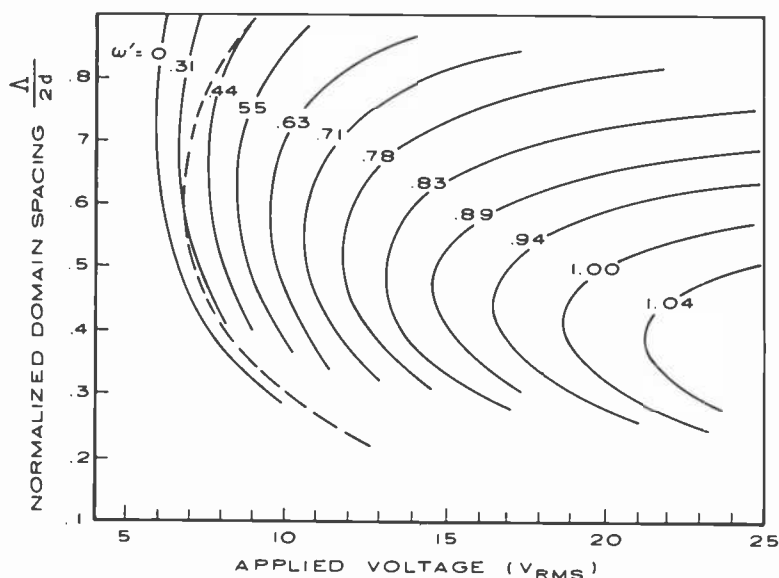


Fig. 2—Plot of Eq. (32) for MBBA (Table 1): $S = \Lambda/2d$ versus V . The parameter is the reduced frequency ω' . The dashed curve is the domain spacing given by Penz and Ford.⁹ Instability occurs at the point on the curve where the voltage is a minimum.

[III,9] of Dubois-Violette⁸ (except for a different definition of the viscosity factor). We note, however, that Penz and Ford's Eq. [31] has a different meaning, because it simply relates E_0 and the various values of S that form the more complicated solutions to the exact boundary value problem (q_z is not defined *a priori*). In the present case, the form of the solution has been given in Eqs. [15] and [16] and q_z has been defined as π/d . Therefore, we can rewrite Eq. [31]

$$V_{th}^2 = \frac{\pi^2}{S^2} (k_{33} + S^2 k_{11}) (1 + \omega^2 \tau^2) \left[\frac{K_1 + S^2 K_2}{\eta_1 + S^2 \eta_2} \cdot \frac{\sigma_1 \epsilon_1 - \sigma_1 \epsilon_1}{\sigma_1 + S^2 \sigma_1} + \Delta \epsilon \frac{(1 + S^2) \sigma_1}{\sigma_1 + S^2 \sigma_1} + \omega^2 \tau^2 \Delta \epsilon \frac{(1 + S^2) \epsilon_1}{\epsilon_1 + S^2 \epsilon_1} \right]^{-1}, \quad [32]$$

which relates the applied voltage V to the domain spacing Λ . The threshold voltage is determined by minimizing V with respect to S . Eq. [32] demonstrates that the relationship is independent of cell thickness, which also appears to be the case for the exact result.⁹

Table 1—Material Parameters of MBBA⁹

k_{11}	$= 6.10 \times 10^{-12}$ newton
k_{33}	$= 7.25 \times 10^{-12}$ newton
$\epsilon_{ }$	$= 4.72$
ϵ_{\perp}	$= 5.25$
η_1	$= 103.5 \times 10^{-3}$ kg/m/sec
η_2	$= 23.8 \times 10^{-3}$ kg/m/sec
α_2	$= -77.5 \times 10^{-3}$ kg/m/sec
α_3	$= -1.2 \times 10^{-3}$ kg/m/sec
$\sigma_{ }/\sigma_{\perp}$	$= 1.5$

Numerical Results and Comparison with Experiment

Eq. [32] is plotted in Fig. 2 for various values of the normalized frequency $\omega' = \omega/\omega_c = \omega\tau_c$, $\tau_c = \epsilon_{||}/\sigma_{||}$. The numerical values used are the same as those used by Penz and Ford⁹ for MBBA (Table 1). For comparison, Fig. 2 also shows the complete solution of these authors ($\omega = 0$). As can be seen, our approximation leads to a somewhat lower threshold, because we have neglected the viscosity force of the walls on the liquid. Note that the threshold for the one-dimensional case ($S = 0$, $q_x = \pi/d$ in Eq. [31]), 2.57 V, is considerably in error. From the curves of Fig. 2, the values of threshold voltage and the corresponding domain spacing are obtained as a function of voltage. They are plotted in Fig. 3 as a function of frequency. Also shown are experimental results of MBBA taken from the paper of Meyerhofer and Sussman¹⁰ for a 10- μ m-thick cell of MBBA with the alignment parallel to the surface. Since the conductivity had not been measured independent-

ly, the experimental data were normalized to agree with the calculated threshold at the highest frequency. The agreement is very satisfactory and shows that the inconsistency discussed in Ref. [10], that resulted when the actual values of Λ are inserted in the Orsay equation,

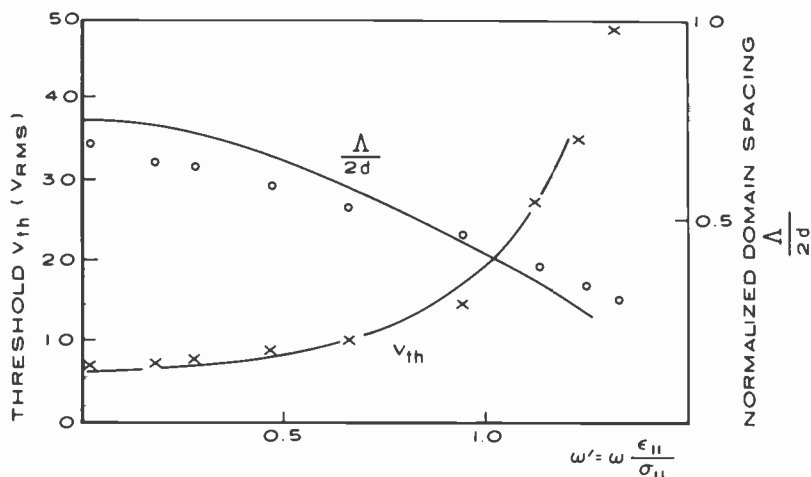


Fig. 3—Threshold and domain spacing as function of ω' . The lines are calculated from the curves of Fig. 2, and the points are the experimental results.¹⁰ The only adjustment of the data was to determine $\tau_c = \epsilon_{||}/\sigma_{||}$ by fitting the measured threshold to the calculated one at one frequency, because the value of $\sigma_{||}$ was not available.

is due to the one-dimensional nature of that theory, and it disappears when the two-dimensional calculation is performed. The good agreement is further demonstrated in Fig. 4, where the threshold voltage is plotted versus domain size (Fig. 2 of Ref. [10]) and the calculated curve has no adjustable parameters.

Range of Applicability

The calculations we have performed apply to the "conduction regime" because of the assumption that θ is constant in time. The range of this regime has been discussed in detail by Dubois-Violette et al⁸ and shown experimentally by Meyerhofer and Sussman.¹⁰ The low-frequency limit varies as d^{-2} ; below this frequency both θ and ρ are

time dependent. The upper frequency limit, near ω_c , is independent of thickness; above this frequency the dielectric regime applies, where ρ is constant and θ varies.

The conduction regime as described by Figs. 2 to 4 occurs in suitably doped nematic liquid crystals of negative dielectric anisotropy. This can be seen qualitatively by studying the denominator of Eq. [32]. The first (viscous) term must be larger than the second (dielectric) term for the denominator to be positive and instability to occur. This restricts negative values of $\Delta\epsilon$ to the range -2 to 0 for materials

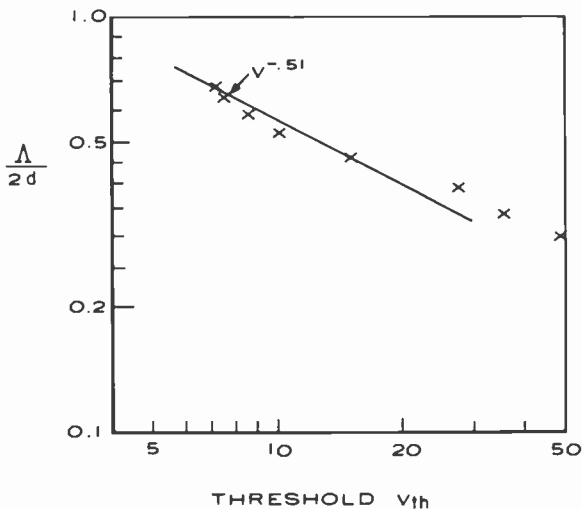


Fig. 4—The data of Fig. 3 plotted as domain spacing versus threshold with frequency as parameter. The crosses are the experimental results.¹⁰ There are no adjustable parameters.

similar to MBBA and PAA ($K_1/\eta_1 = 0.75$, $\sigma_{\parallel}/\sigma_{\perp} = 1.5 > \epsilon_{\parallel}/\epsilon_{\perp}$). For such materials, the threshold increases strongly with frequency, leading to a cutoff of the conduction regime near $\omega\tau_c = 1$.

Eq. [32] shows that instability can also take place for $\Delta\epsilon > 0$, as discussed by Dubois-Violette⁸ and Penz.¹⁴ In that case, the threshold voltage becomes independent of frequency at high frequency, but this is not a conduction regime because V_{th} is then only dependent on k and ϵ . Furthermore, this threshold is higher than that of the dielectric Freedericksz transition¹⁵ for the case of the entire sample deforming uniformly ($S = 0$, $V_{th} = \pi\sqrt{k_{11}/\Delta\epsilon}$), and so will not occur. In fact,

Williams domains will occur only over the range of $\Delta\epsilon$ from 0 to approximately 0.5. These considerations are in agreement with experimental observations.¹⁶

References:

- ¹ R. Williams, "Domains in Liquid Crystals," *J. Chem. Phys.*, **39**, p. 384 (1963).
- ² G. H. Heilmeyer, L. A. Zaroni, and L. A. Barton, "Dynamic Scattering: A New Electrooptic Effect in Certain Classes of Nematic Liquid Crystals," *Proc. IEEE*, **56**, p. 1162 (1968).
- ³ P. A. Penz, "Voltage-Induced Velocity and Optical Focusing in Liquid Crystals," *Phys. Rev. Lett.*, **24**, p. 1405 (1970); "Order Parameter Distribution for the Electrohydrodynamic Mode of a Nematic Liquid Crystal," *Mol. Cryst. Liq. Cryst.*, **15**, p. 141 (1971).
- ⁴ S. Chandrasekhar, *Hydrodynamic and Hydromagnetic Stability*, Clarendon Press, Oxford, England (1961).
- ⁵ N. Filici, "Phénomènes hydro et Aérodynamiques dans la Conduction des diélectriques Fluids," *Rev. Gen. Elect.*, **78**, p. 717 (1969).
- ⁶ H. Gruler and G. Meier, "Correlation between Electrical Properties and Optical Behaviour of Nematic Liquid Crystals," *Mol. Cryst. Liq. Cryst.*, **12**, p. 289 (1971).
- ⁷ W. Helfrich, "Conduction-Induced Alignment of Nematic Liquid Crystals: Basic Model and Stability Considerations," *J. Chem. Phys.*, **51**, p. 4092 (1969).
- ⁸ E. Dubois-Violette, P. G. deGennes, and O. Parodi, "Hydrodynamic Instabilities of Nematic Liquid Crystals under AC Electric Fields," *J. Phys. (Paris)*, **32**, p. 305 (1971).
- ⁹ P. A. Penz and G. W. Ford, "Electromagnetic Hydrodynamics of Liquid Crystals," *Phys. Rev.*, **A6**, p. 414 (1972).
- ¹⁰ D. Meyerhofer and A. Sussman, "Electrohydrodynamic Instabilities in Nematic Liquid Crystals in Low-Frequency Fields," *Appl. Phys. Lett.*, **20**, p. 337 (1972).
- ¹¹ F. M. Leslie, "Some Constitutive Equations for Anisotropic Fluids," *Quart. J. Mech. Appl. Math.*, **19**, p. 357 (1966); and "Some Constitutive Equations for Liquid Crystals," *Arch. Ration. Mech. Analysis*, **28**, p. 265 (1968).
- ¹² F. S. Frank, "On the Theory of Liquid Crystals," *Discuss. Faraday Soc.*, **25**, p. 19 (1958).
- ¹³ O. Parodi, "Stress Tensor for a Nematic Liquid Crystal," *J. Phys. (Paris)*, **31**, p. 581 (1970).
- ¹⁴ P. A. Penz, "Electrohydrodynamic Solutions for Nematic Liquid Crystals with Positive Dielectric Anisotropy," *Mol. Cryst. Liq. Cryst.*, **23**, p. 1 (1973).
- ¹⁵ V. Freedericksz and W. Zvetkoff, "Über die Einwirkung des Elektrischen Feldes auf Anisotrope Flüssigkeiten. II. Orientierung der Flüssigkeit im Elektrischen Felde," *Acta Physicochim. USSR*, **3**, p. 895 (1935).
- ¹⁶ H. Gruler and G. Meier, "Electric Field-Induced Deformations in Oriented Liquid Crystals of the Nematic Type," *Mol. Cryst. Liq. Cryst.*, **16**, p. 299 (1972); W. H. deJeu, C. J. Gerritsma, and T. W. Lathouwers, "Instabilities in Electric Fields of Nematic Liquid Crystals with Positive Dielectric Anisotropy: Domains, Loop Domains, and Reorientation," *Chem. Phys. Lett.*, **14**, p. 503 (1972).

Liquid-Crystal Displays— Packaging and Surface Treatments

L. A. Goodman

RCA Laboratories, Princeton, N. J. 08540

Abstract—Electrode materials and techniques for cell construction are presented. Next, the common surface orientations and the methods for obtaining them are described. Third, two examples are given that demonstrate the relationship between packaging technology and liquid-crystal alignment.

1. Introduction

For the proper operation of liquid-crystal display devices, appropriate cell construction and surface treatment methods are necessary. In this article, first, some of the general packaging techniques that are being used today are outlined. Second, the common conductive coatings are listed and standard preparation methods given. Third, the diverse surface treatment methods are summarized and, finally, some relationships between cell construction and device operation are discussed.

2. Packaging

The standard sandwich cell configuration for liquid-crystal displays is schematically illustrated in Fig. 1. Normally, low cost soda-lime soft glass is used. However, more expensive borosilicate and fused silica substrates can also be utilized. The spacing between top and bottom glass plates varies from 5 to 50 μm with nominal values being in the 10 to 20 μm range. The spacer composition is restricted by possi-

ble chemical reactions with the liquid crystal. Glass frits and relatively inert organic materials such as Teflon and Mylar can be used as the spacer materials.

The sealing materials are limited both by the need for compatibility with the liquid crystal and by the need for a fairly hermetic seal

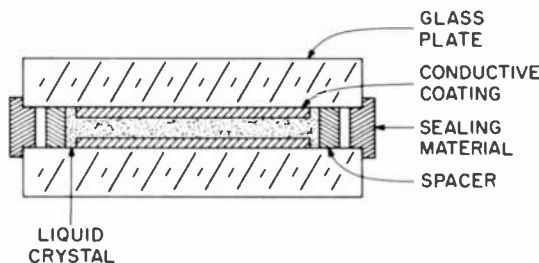


Fig. 1—Side view of schematic representation of a liquid-crystal cell.

since both moisture and oxygen can react with many mesomorphic systems in a deleterious fashion. Other criteria for selecting sealing materials are thermal expansion match with the glass plates, bonding strength, sealing temperature, and manufacturing cost. Glass frits, solder glasses, and polymeric materials are suitable sealing materials.

3. Electrodes

At least one of the conductive coatings in a liquid-crystal display must be transparent. The most common transparent conductive coating material is a mixture of indium oxide and tin oxide. This material can be prepared by several different techniques which include (1) rf sputtering of indium-tin oxide powder targets,¹ (2) dc sputtering of highly conducting indium-tin oxide powder targets,² (3) dc reactive sputtering of an indium-tin alloy,³ (4) thermal evaporation,⁴ and (5) high-temperature (400°C) bake-out of spun-on solutions.⁵ The sheet resistance of as-deposited indium-tin oxide coatings can vary from 2 ohms/square up to many kilohms per square.² After bake-out in air at temperatures in excess of 500°C, the resistance increases by a factor of 3 to 10.^{1,2} The required sheet resistance for liquid-crystal displays is in the 100 to 500 ohms/square range. The optical transmission of these films is excellent, and some typical results are given in Fig. 2.

Another compound commonly used for conductive coatings is antimony-doped tin oxide, which is usually deposited by a pyrolytic spray

process at temperatures between 600 and 700°C. The chemical durability, abrasion resistance, electrical conductivity, and typical transmission are all very adequate. Surface resistances as low as 40 ohms/square can be achieved with a transmission in excess of 75–80%.

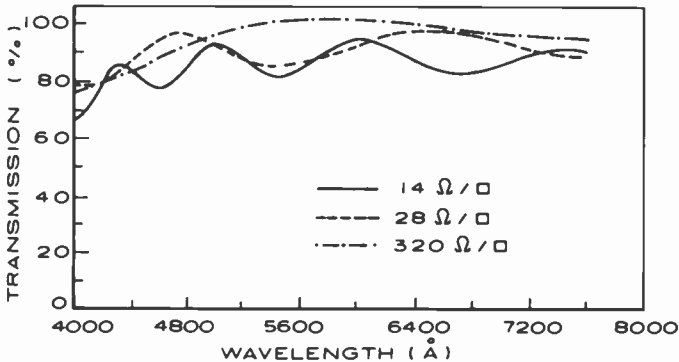


Fig. 2—Transmission versus wavelength for $\text{In}_2\text{O}_3\text{-SnO}_3$ films deposited in argon to different thicknesses.¹

The chemically deposited tin oxide suffers from two important disadvantages as compared to the vacuum-deposited indium–tin oxide. At the high temperatures necessary for the spray deposition process, soft glass loses its flatness. The different approaches previously listed for creating the indium–tin oxide films can all be performed at sufficiently low temperature that the soft glass substrates do not warp. In liquid-crystal displays, where a relatively narrow spacing between opposite electrodes is required, the loss in flatness caused by the spray process is a distinct drawback.

Antimony-doped tin oxide can also be deposited by sputtering, but the sheet resistance is not as low as with sputtered indium–tin oxide. In addition, for the tin oxide concentrations normally used, the indium–tin oxide films can be readily etched in hydrochloric acid.^{3,6} Antimony-doped tin oxide films are not readily soluble in acids or bases, but they can be etched by a procedure using zinc dust and hydrochloric acid.⁷

Reflective electrodes are readily obtained by the evaporation of metals—for example, aluminum or chromium. Other coatings such as layers of insulating dielectrics are also used to obtain specular surfaces. These can be deposited by both electron-beam and thermal-evaporation methods.⁴

4. Surface Orientation

A unit vector called the director denotes the average orientation of the long molecular axes in any local region of the fluid. For the purpose of maximizing the contrast ratio of the display, it is desirable that the orientation of the directors be the same throughout the fluid whether the applied voltage is on or off. Two important examples of maximum ordering are shown in Fig. 3. For perpendicular (or homeo-

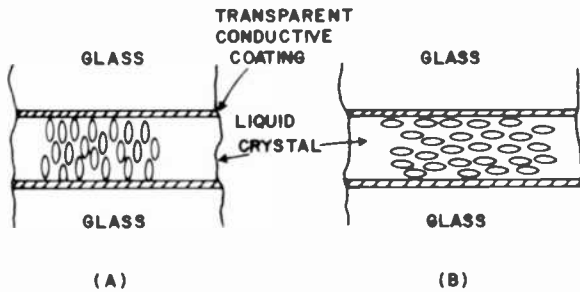


Fig. 3—Side view (A) of homeotropic and (B) of homogeneous orientations.

tropic) alignment, all of the long molecular axes are perpendicular to the cell walls. Looking down through the cell, the fluid appears to be isotropic, and this state is optically clear. When the mesomorphic medium possesses uniform parallel (or homogeneous) orientation, the director is parallel to the cell walls over dimensions of a millimeter or more and points in only one direction. As observed in a top view, the fluid has the optical properties of a uniaxial single crystal with the director describing the main axis (see Fig. 4A). The "head" and the "tail" of the director can be interchanged without changing the observable fluid properties.

There are two other examples of fluid orientation that are closely related to uniform parallel alignment. In the first case, the director also lies parallel to the cell surfaces. However, the director orientation in the plane parallel to the cell walls is not uniform; rather, it changes randomly over dimensions on the order of micrometers. This orientation is known as random parallel alignment (see Fig. 4B).

The second related example is the planar or Grandjean texture of the cholesteric mesophase. In the planar state, the main helix axis is perpendicular to the electrode surfaces of the cell. Consequently, the director is always oriented parallel to the surface with the orientation

of the director varying in helical fashion with linear distance along the helix axis (see Figure 4C).

Four states of bulk orientation have been described so far. Because of the long-range ordering forces that operate in liquid crystals, the preceding bulk orientations can be produced by the proper treatment

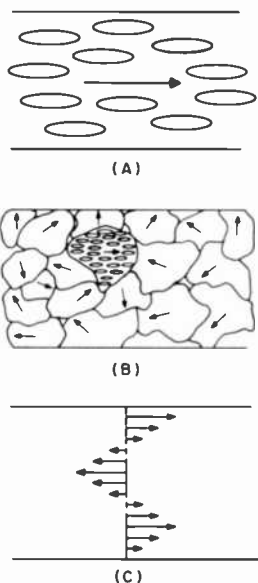


Fig. 4—Top view (A) of homogeneous orientation and (B) of random parallel alignment (the arrows represent the directors) (C) Side view of cholesteric planar texture. Length of director arrows illustrates the amount of twist of each layer.

of the surface region between the liquid crystal and the cell walls. The mechanisms of surface alignment have been poorly understood, but recent investigations seem to be leading toward a better comprehension of them.

In his work on optical textures in mesomorphic materials, Friedel presented an interesting discussion of both the uniform parallel and perpendicular states.⁸ However, the techniques he describes for achieving these two states are rather cumbersome. Since that time, a number of investigators have described different methods for obtaining perpendicular alignment. These have included chemical etching,^{9,10} coating with lecithin,¹¹ and physical adsorption of organic surfactant additives such as the polyamide resin Versamid¹² or impuri-

ties in the fluid¹³ that are the thermal decomposition products of the mesomorphic material.

Petrie et al¹⁴ indicated that additives of certain surface-active molecules such as tertiary amines, quaternary ammonium salts, and pyridinium salts produced perpendicular alignment. Specifically, Haller and Huggins¹⁵ reported that the quaternary ammonium salt, hexadecyltrimethylammoniumbromide (HTAB), caused perpendicular alignment.

Zocher¹⁶ stated that uniform parallel alignment could be obtained if the cell surfaces were first unidirectionally rubbed. Various materials such as paper, tissue, and cotton wool were used to achieve uniform parallel alignment. Chatelain¹⁷ hypothesized that the parallel orientation resulted from the forces generated by the presence of an adsorbed layer of fatty contaminants on the cell surface, and the directionality was achieved by the unidirectional rubbing. However, he could not eliminate the possibility that mechanical deformation of surface might have induced the observed alignment.

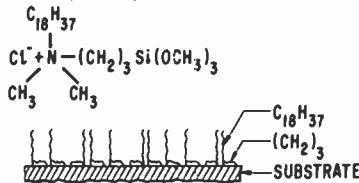
Several recent articles support the theory that physicochemical forces, e.g., van der Waals, hydrogen bonding, and dipolar forces, are dominant. Proust et al¹⁸ have obtained both uniform parallel and perpendicular alignment by depositing monolayers of hexadecyltrimethylammoniumbromide (HTAB) from aqueous solution onto glass slides prior to the insertion of the liquid crystal between the slides. They stated that perpendicular alignment was obtained when the bromide compound was densely packed in the monolayer; consequently, the molecules were oriented normal to the glass slide. Uniform parallel alignment was observed when the monolayer was less densely packed and the molecules were oriented parallel to the surface. They achieved the directionality necessary for uniform parallel orientation by withdrawing the glass slides from the bromide-containing solution in one direction.

Kahn¹⁹ has also demonstrated the importance of physicochemical forces. He has prepared highly stable surface aligning conditions by the utilization of silane coupling agents that were chemically bonded to the glass surface. The preparation of the organosilane layer was affected by the nature of the metal oxide surface, the degree of surface hydration, and the pH of the solutions used for deposition. The alkoxy silane monomers of the general type $RSiX_3$ were found to be quite useful for aligning liquid crystals. R is an organofunctional orienting group and X designates a hydrolyzable group attached to the silicon. Schematic illustrations of the cured coatings and the chemical formulas for the silane agents are given in Fig. 5. The DMOAP coating resulted in perpendicular alignment of the liquid crystal; parallel

alignment of the mesomorphic molecules was produced by the cured MAP layer.

Berreman^{20,21} calculated the difference in elastic strain energy that occurs when a nematic fluid lies parallel to grooves in a surface rather than perpendicular to them. As a consequence of his calculations and experimental observations made by himself and Dryer,¹¹ Berreman has suggested that the anisotropy in elastic strain energy of the liquid crystal is sufficient to induce the alignment of the fluid director parallel to the grooves in the surface. Furthermore, he concluded that

(a) *N,N*-dimethyl-*N*-octadecyl-3-aminopropyltrimethoxysilyl chloride (DMOAP)



(b) *N*-methyl-3-aminopropyltrimethoxysilane (MAP)

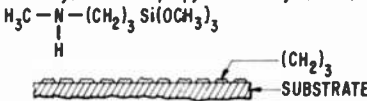


Fig. 5—Chemical formulae for two silane coupling agents and their geometric relationship to a substrate when cured.¹⁸

the elastic energy considerations explain the tendency of some nematic molecules to align perpendicular to a surface that is rough in two dimensions even if physicochemical forces would normally cause the molecules to lie parallel to a flat surface of the same solid.

Creagh and Kmetz^{22,23} have recently suggested an explanation of surface orientation forces that is a synthesis of both the physicochemical and geometric factor hypotheses. Using chemically cleaned tin oxide coated glass substrates, they investigated a number of different surface aligning conditions. Thorough cleaning with chromic acid was required because they found that, in the absence of the cleaning, trace remnants of carbon on the glass surface caused nematic fluids such as MBBA and PAA (*p*-azoxyanisole) to align with the long axes of the molecules parallel to the surface. With the appropriate cleaning, these materials aligned in the perpendicular state.

The data presented in Fig. 6 summarizes the results of their tests on surface alignment. Cells were prepared with different aligning







		Surfactant		
		None	Lecithin	Carbon
Grooves	No	 (Random tilt with E)		Random 
	Yes	 (Tilt along grooves with E)		 Homogeneous

Fig. 6—Matrix of alignment results for various grooving and surfactant conditions.²³

agents and either with or without grooves. The grooves were obtained by rubbing the surfaces with a diamond paste. Fig. 7 is a typical electron micrograph of a rubbed surface. The tabulated results show that the evaporated carbon layer gave parallel orientation with the grooves providing the unidirectionality necessary for uniform parallel alignment.

With both lecithin-coated and chemically cleaned surfaces, rub-

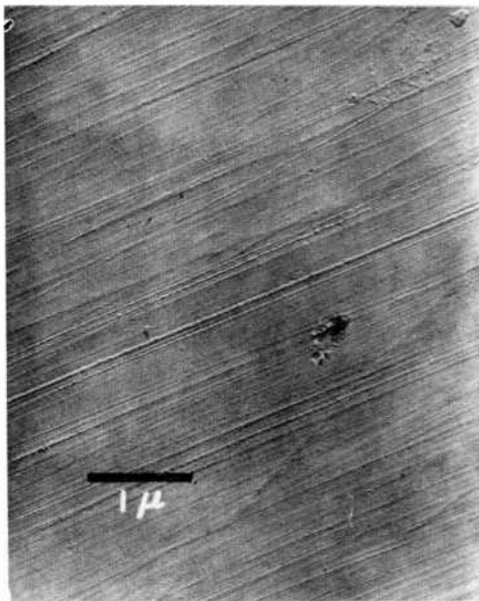


Fig. 7—Scanning electron micrograph of a substrate grooved with 1- μ m diamond paste and then cleaned.²³

bing did not result in uniform parallel alignment. In both situations, perpendicular orientation occurred for no applied voltage. When a voltage was applied to the fluid, either one of two configurations appeared. With no grooving, the nematic fluid adopted the random parallel condition, whereas when the surfaces were rubbed with the diamond paste, the nematic director adopted a uniform orientation in the direction of rubbing.

As a result of their experimental observations, Creagh and Kmetz claimed that the determination of whether a liquid crystal adopts the perpendicular or parallel orientation can be made on the basis of the relative surface energy of the substrate and the surface tension of the fluid. They asserted that when the surface energy of the substrate is low compared to that of the liquid crystal the fluid does not wet the surface, and intermolecular forces within the fluid produce the perpendicular texture. However, if the relative surface energy of the solid is high, the fluid wets the substrate, and the long axes of the molecules align parallel to the surface. They also quoted the results of Proust et al.¹⁸ in support of their theory. Apparently, the surface energy is lower when the hexadecyltrimethylammoniumbromide molecules are densely packed on the surface than when they are diffusely packed.

Their observation that the nematic director was normal to thoroughly cleaned surfaces is somewhat at variance with the above conclusions, since one would expect the solid surface to possess a high surface free energy, but they have given an explanation. The apparent discrepancy was presumably caused by the presence of a thin layer of water on the surface. They cited the results of Shafrin and Zisman,²⁴ namely, that at normal relative humidity, the critical surface tension of glass at 20°C is about 30 dynes/cm for nonhydrophilic liquids. This surface water can only be removed by prolonged heating. In further support of their theory, Creagh and Kmetz were able to achieve random parallel alignment on flame-fired platinum substrates. Fig. 8 is a summary of their results on the effect of surface energy on orientation.

In the model of Creagh and Kmetz, the main effect of grooving appears to have been the provision of a preferred direction for the molecules in accord with calculations made by Berreman^{20,21} and Grabmeier et al.^{25,26} The physicochemical forces determined whether the molecules were parallel or perpendicular to the substrate surface. They concluded that Chatelain's hypothesis was correct—that the conventional rubbing technique provided uniform parallel alignment by grooving an organic surface layer produced by the rubbing medium, be it cloth or paper.

Kahn, Taylor, and Schonhorn²⁷ have expanded upon the ideas discussed by Creagh and Kmetz.^{22,23} In essence, Kahn et al agreed with the concepts propounded by Creagh and Kmetz with regard to the relative importance of the physicochemical and elastic forces in the

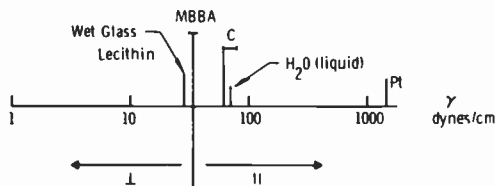


Fig. 8—Alignment of MBBA on substrates with different surface energies.²³

fluid. However, they did not describe the physicochemical interaction between the liquid and the solid in terms of the liquid surface tension, γ_L , and the surface tension of the solid, γ_S . Rather they characterized the solid by its critical surface tension, γ_c , and the liquid by its surface tension, γ_L . The critical surface tension of a solid is an empirically determined quantity first proposed by Zisman and associates²⁸ to classify low-energy solid surfaces.

As explained by Adamson,²⁹ γ_c is not a fundamental property of the solid surface alone, but also depends upon the nature of fluid in contact with the solid. Apparently, it is only a fixed quantity for a given homologous series of organic liquids on the solid. γ_c values can vary somewhat from one homologous series of liquids to another.

Kahn et al,²⁷ also noted that the γ_c of a solid, in particular one of high surface energy, can be drastically lowered by the presence of a layer of liquid molecules that has been preferentially adsorbed at the solid-liquid interface. If the molecules in the monolayer have both polar and nonpolar ends, the polar ends will often attach themselves to the high-energy surface, with the nonpolar portion facing into the liquid. As far as the bulk liquid is concerned, the nonpolar groups present a lower surface energy to the fluid than the free solid surface, and consequently the effective γ_c is lowered. The adsorbed monolayer can consist of intentionally added impurities in the fluid¹²⁻¹⁴ or unintentional impurities. In addition, for certain impurity-free liquids, the molecular structure may be such that the fluid cannot spread on its own monolayer. These are known as "autophobic" liquids.²⁸

Proust and Ter-Minassian-Saraga³⁰ have measured the contact

angle ϕ and calculated the work of adhesion, $W_A = \gamma_L (1 + \cos \phi)$, of MBBA to glass surfaces coated with a monolayer of HTAB. As previously described,¹⁸ the MBBA had either uniform parallel or perpendicular orientation depending upon the surface density of the HTAB. They have found that the contact angle associated with parallel alignment was 32° instead of 0° . Also, in spite of the fact that the alignment changed sharply from parallel to perpendicular due to a small increase in the surface density of HTAB, the contact angle only increased slightly—to 37° . The work of adhesion gradually decreased during the transition from parallel to perpendicular orientation. The general criterion enunciated by Creagh and Kmetz^{22,23} that parallel alignment is caused by stronger solid-liquid forces than those present with perpendicular alignment was verified, but parallel alignment was not associated with wetting of the solid by the surface.

Haller³¹ has measured the contact angle at the solid-liquid interface for three different liquid crystals in contact with coated solid surfaces and has also observed the alignment properties of the various liquid crystals in sandwich cells with the specially treated surfaces. The surface energy of the glass plates was varied by treatment with either an organic monolayer or multi-molecular layer. Of the three liquid crystals, only MBBA exhibited perpendicular orientation on glass surfaces coated with octadecyltrichlorosilane, HTAB, or barium stearate. All three liquid crystals, MBBA, BECS (4-n-butyl-4-ethoxy-2-chlorostilbene) and LiCristal IV (isomeric mixture of 4-methoxy-4'-butylazoxybenzenes) had surface tensions far in excess of the γ_c 's of the coatings that were measured with unnamed isotropic test liquids. It should be noted that the three liquid crystals have different central linkages, and it is possible that this variation in chemical structure accounts for the diverse results. Haller concluded that the proposed correlation between wetting and alignment properties was too general, and specific details of the interaction forces were necessary for a precise prediction of the alignment properties.

A technique for producing uniform parallel alignment that does not involve organic coatings has been described by Janning.³² The surface preparation consisted of evaporating materials such as gold, aluminum, platinum, or silicon monoxide onto the substrate at an angle of 85° to the substrate normal. The films were 100 \AA or less thick. Cells containing MBBA and using glass plates coated in this manner exhibited uniform parallel alignment.

Recently Guyon, Pieranski, and Boix³³ investigated the dependence of liquid-crystal orientation on the angle, θ , between the evaporation direction and the normal to the substrate. Their principal results were:

- (1) $0 < \theta < 45^\circ$. No preferred direction for the alignment of MBBA was observed.
- (2) $45^\circ < \theta < 80^\circ$. Uniform parallel alignment was obtained with the preferred direction being perpendicular to the plane containing the direction of evaporation and the normal to the substrate.
- (3) $80^\circ < \theta < 90^\circ$. The fluid director possessed a preferred direction of orientation in the plane of evaporation; however, the direction did not lie parallel to substrate, but instead it was tilted out of the substrate plane at an angle between 20° and 30° .

The authors hypothesized that the evaporated coatings were deposited with a sawtooth surface profile whose shape depended on the oblique angle of incidence. For $45^\circ < \theta < 80^\circ$, it was felt that the long axes of the fluid lay parallel to the long axes of the sawtooth grooves. They also argued for $80^\circ < \theta < 90^\circ$ that the liquid crystal director was pointed into the teeth of sawtooth. Most of their data was obtained with SiO_x , but they stated that similar data was achieved with C and Au.

Complete microscopic confirmation of their model has not yet been obtained, although using high magnification with an electron microscope, Dixon, Brody, and Hester³⁴ have observed fine structure in 85° evaporated SiO_x films with the structure oriented in the plane of evaporation.

Guyon et al³³ did not state the exact nature of the liquid-crystal orientation with films evaporated at $\theta = 0^\circ$. Meyerhofer³⁵ has measured random parallel alignment for $\theta = 0^\circ$ evaporations. A reasonable conclusion that can be drawn from the data is that, when in contact with mesomorphic fluids, freshly evaporated SiO_x films produce parallel alignment in liquid crystals through physicochemical forces. At the present time, it is still not clear whether the directionality induced in the liquid crystal by obliquely evaporated SiO_x film is caused by the sawtooth model or some other anisotropic property of the SiO_x .

5. Influence of Packaging on Surface Orientation

In the section on packaging we have indicated that some liquid crystals are adversely affected by coming in contact with moisture; consequently, for these materials a good water-tight seal is necessary. The moisture can increase the fluid conductivity, produce a lowering of the mesomorphic-isotropic transition, or can participate in the production of impurities in the fluid that are adsorbed onto the surface

and that can modify the alignment of the liquid crystal through a change of the forces at the solid-liquid interface.

Not only may the choice of sealing technique be important for controllable liquid-crystal orientation, but the effect of the interaction at the glass-liquid crystal interface must be considered in the selection of the type of glass to be used in the liquid crystal cells. Workers at E. Merck Co.³⁶ stated that it was easier to achieve perpendicular alignment on borosilicate glass than soda-lime glass when both types of glass pieces had been heated above 100°C. They claimed that the alkali impurities in the soda-lime glass caused a disorientation of the liquid crystal in some unknown manner. They were able to prevent the alkali-induced misorientation by rinsing the heated plates in chromosulfuric acid or water. They suggested that overcoating the glass surface with inorganic thin films such as MgF_2 and SiO_2 should alleviate the condition. Also, they found that the addition of certain surfactants such as lecithin or tetraalkyl ammonium salts to the liquid crystal produces good perpendicular alignment even between two soft glass plates that had been heated above 100°C.

We have found³⁷ that even with as much as 0.1% of HTAB added to MBBA, misorientation gradually occurred on solid glass surfaces that had been heated to 400°–500°C. When the cells were first made, good perpendicular alignment was achieved. However, over a period of time of up to several months at 25–30°C, or within a few hours at 85°C, the fluid slowly lost its perpendicular orientation. Cells made with fused silica plates did not exhibit this degradation. The data obtained from an ion-scattering analysis of the surfaces of the glass plates fired at high temperature showed a strong excess of cations, in particular, alkali ions. These results strongly support the original suggestion of alkali-induced misalignment.

6. Summary

A short outline of the standard conductive coatings and packaging methods has been presented.

Most of the paper has been devoted to a discussion of the different surface treatments used to obtain controllable molecular alignment in liquid-crystal cells. The methods reviewed for obtaining parallel or perpendicular alignment were the use of surfactant additives, organic coatings on the solid surface, rubbing of the solid surface, and evaporation of inorganic materials. The data in the literature strongly suggests that the strength of the physicochemical forces at the liquid-crystal-solid interface is the most important element in determining

whether parallel or perpendicular orientation will occur. However, the details of the interaction are sufficiently complicated that it is very difficult at the present time to make totally valid predictions about orientation for a specific solid surface and a particular liquid crystal. The directionality necessary for uniform parallel alignment can be provided by physical grooving of the solid surface, unidirectional withdrawal of the glass substrates from a coating solution, or by using an oblique angle of incidence during the evaporation of inorganic materials onto the glass surfaces.

Finally, two examples have been presented which show the relationship between packaging techniques and liquid-crystal molecular orientation.

References:

- ¹ J. L. Vossen, "RF Sputtered Transparent Conductors II: The System $\text{In}_2\text{O}_3\text{-SnO}_2$," *RCA Rev.*, **32**, p. 289, June 1971.
- ² D. B. Fraser and H. D. Cook, "Highly Conductive Transparent Films of Sputtered $\text{In}_{2-x}\text{Sn}_x\text{O}_{3-y}$," *J. Electrochem. Soc.*, **119**, p. 1368 (1972).
- ³ F. H. Gillery, "Transparent Conductive Coatings of Indium Oxide," *Information Display*, **9**, p. 17 (1972).
- ⁴ R. Clary, Optical Coating Lab., Inc., Santa Rosa, California; private communication.
- ⁵ Emulsitone Solution No. 673, Emulsitone Co., Millburn, N.J.
- ⁶ Bulletin on Indium Oxide Conductive Coatings, Optical Coating Laboratory, Inc., Santa Rosa, Calif.
- ⁷ Bulletin entitled "Nesa and Nesatron Glass," PPG Industries, Industrial Glass Products, Pittsburgh, Penna.
- ⁸ G. Friedel, "The Mesomorphic States of Matter," *Ann. Physique*, **18**, p. 273 (1922).
- ⁹ H. Zocher, *Z. Phys. Chem.*, **132**, 285 (1928).
- ¹⁰ M. F. Schiekel and K. Fahrenschon, "Deformation of Nematic Liquid Crystals with Vertical Orientation in Electrical Fields," *Appl. Phys. Lett.*, **19**, p. 391 (1971).
- ¹¹ J. F. Dryer, "Epitaxy of Nematic Liquid Crystals," p. 1113 in *Liquid Crystals 3*, G. H. Brown and M. M. Labes, eds., Gordon and Breach, London (1973).
- ¹² W. Haas, J. Adams, and J. Flannery, "New Electro-Optic Effect in a Room-Temperature Nematic Liquid Crystal," *Phys. Rev. Lett.*, **25**, p. 1326 (1970).
- ¹³ T. Uchida, H. Watanabe, and M. Wada, "Molecular Arrangement of Nematic Liquid Crystals," *Jap. J. Appl. Phys.*, **11**, p. 1559, (1972).
- ¹⁴ S. E. Petrie, H. K. Bucher, R. T. Klingbiel, and P. I. Rose, "Aspects of Physical Properties and Applications of Liquid Crystals," *Organic Chemical Bulletin* **45**, No. 2 (1973), Eastman Kodak Co., Rochester, N.Y.
- ¹⁵ I. Haller and H. A. Huggins, Additive for Liquid Crystal Material, U.S. Patent 3,656,834, April 18, 1972.
- ¹⁶ H. Zocher and K. Coper, *Z. Phys. Chem.*, **132**, p. 195 (1928).
- ¹⁷ P. Chatelain, *Bull. Soc. Franc. Miner. Christ.* **66**, p. 105 (1943).
- ¹⁸ J. Eroust, L. Ter-Minassian-Saraga, and E. Guyon, "Orientation of a Nematic Liquid Crystal by Suitable Boundary Conditions," *Sol. St. Commun.*, **11**, p. 1227 (1972).
- ¹⁹ F. J. Kahn, "Orientation of Liquid Crystals by Surface Coupling Agents," *App. Phys. Lett.*, **22**, p. 386 (1973).
- ²⁰ D. W. Berreman, "Solid Surface Shapes and the Alignment of an Adjacent Nematic Liquid Crystal," *Phys. Rev. Lett.*, **28**, p. 1683 (1972).
- ²¹ D. W. Berreman, "Alignment of Liquid Crystals by Grooved Surfaces," *Mol. Cryst. and Liq. Cryst.*, **23**, p. 215 (1974).
- ²² L. T. Creagh and A. R. Kmetz, "Performance Advantages of Liquid Crystal Displays with Surfactant-Produced Homogeneous Alignment," *Digest of 1972 Soc. for Information Display International Symp.*, San Francisco, Calif., p. 90.

- ²³ L. T. Creagh and A. R. Kmetz, "Mechanism of Surface Alignment in Nematic Liquid Crystals," 4th International Liquid Crystal Conf., Kent, Ohio, Aug. 1972, paper No. 20.
- ²⁴ E. G. Shafrin and W. A. Zisman, "Effect of Adsorbed Water on the Spreading of Organic Liquids on Soda-Lime Glass," *J. Amer. Ceramic Soc.*, **50**, p. 478 (1967).
- ²⁵ J. G. Grabmeier, W. F. Greubel, H. H. Keuger, and U. W. Wolff, "Homogeneous Orientation of Liquid Crystal Layers," 4th International Liquid Crystal Conf., Kent, Ohio, Aug. 1972, Paper No. 103.
- ²⁶ U. Wolff, W. Greubel, and H. Kruger, "The Homogeneous Alignment of Liquid Crystal Layers," *Mol. Cryst. and Liq. Cryst.*, **23**, p. 187 (1974).
- ²⁷ F. J. Kahn, G. N. Taylor, and H. Schonhorn, "Surface-Produced Alignment of Liquid Crystals," *Proc. IEEE*, **61**, p. 823 (1973).
- ²⁸ W. A. Zisman, "Relation of the Equilibrium Contact Angle to Liquid and Solid Constitution," *Adv. Chem. Ser.*, **43**, p. 1 (1964).
- ²⁹ A. W. Adamson, *Physical Chemistry of Solids*, 2nd ed. New York: Interscience, 1967, Chap. VII.
- ³⁰ J. E. Proust and L. Ter-Minassian-Saraga, "Notes des Membres et Correspondants et Notes Présentées ou Transmises Par Leurs Soins," *C. R. Acad. Sci.*, **276C**, p. 1731 (1973).
- ³¹ I. Haller, "Alignment and Wetting Properties of Nematic Liquids," *Appl. Phys. Lett.*, **24**, p. 349 (1974).
- ³² J. L. Janning, "Thin-Film Surface Orientation for Liquid Crystals," *Appl. Phys. Lett.*, **21**, p. 173 (1972).
- ³³ E. Guyon, P. Pieranski, and M. Boix, "On Different Boundary Conditions of Nematic Films Deposited on Obliquely Evaporated Plates," *Letters in Appl. and Eng. Science*, **1**, p. 19 (1973).
- ³⁴ G. D. Dixon, T. P. Brody, and W. A. Hester, "Alignment Mechanism in Twisted Nematic Layers," *Appl. Phys. Lett.*, **24**, p. 47 (1974).
- ³⁵ D. Meyerhofer, Private Communication.
- ³⁶ Current Information on Liquid Crystals No. 4 (1973), E. Merck Co., Darmstadt, Federal Republic of Germany.
- ³⁷ L. Goodman and F. DiGeronimo, "Nematic Liquid Crystal Misalignment Induced by Excess Alkali Impurities in Soft Glass," 5th International Liquid Crystal Conf., Stockholm, Sweden, June 1974.

Pressure Effects in Sealed Liquid-Crystal Cells

Richard Williams

RCA Laboratories, Princeton, N. J. 08540

Abstract—The thermal expansion coefficient for nematic liquids is about 100 times that for glass. When the liquid is hermetically sealed into a cell, this mismatch generates an internal pressure whenever the ambient temperature is different from the filling temperature. The magnitude of the effect is very strongly dependent on the detailed cell design. A simple analysis of the problem shows those factors that are most important.

Introduction

Liquid crystal cells are hermetically sealed glass containers completely filled with liquid. Two plane-parallel plates are sealed all around the edges to a frit glass spacer. The cell is then filled with liquid through two holes and sealed off with plugs of fusible metal. This construction gives rise to some internal pressure effects, because the thermal expansion coefficient of the liquid is about 100 times that of the glass. If the cell is filled and sealed off at room temperature, the liquid will exert a pressure at all higher temperatures. At lower temperatures it will be under tension. The pressure will deform the cell, making the walls bow out. This makes the volume enclosed by the cell a little larger and reduces the pressure but does not eliminate it completely. Some pressure or tension will always remain for temperatures different from the filling temperature. Repeated expansion and contraction may lead to loss of hermeticity or other cell failure. In what follows, the magnitude of the effect is calculated and the important factors are analyzed.

Fig. 1 shows the effect schematically and gives the notation used for the cell dimensions. The thickness of the layer of the liquid crystal is z , the length and width of the cell are b and a , and t is the thickness of the glass plates.

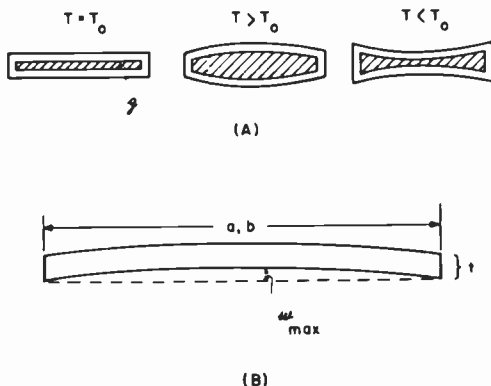


Fig. 1—(A) Expansion and contraction effects as the filled cell is maintained at a temperature T higher or lower than the filling temperature T_0 . (B) Deformation of one of the plates: a , b are the width and length and t is the thickness of the glass. The maximum displacement w_{max} is at the center of the plate.

If the temperature is raised after filling, the liquid expands, and the cell walls bow out to accommodate the change in volume. We can neglect the thermal expansion of the glass and the changes of the liquid volume due to changes in pressure, since both these effects are small compared to the volume change of the liquid due to thermal expansion. The cell walls are held at the edges and the pressure of the liquid exerts a uniform force per unit area over the surface.

Consider the case where the cell is filled and sealed at temperature T_0 and later warmed to temperature T . As the walls bow out, the edges stay fixed. The maximum displacement, w_{max} , of the plate from its unstressed position will be at the center (Fig. 1). We need to determine the volume change Δv due to this deformation of the cell walls. The volume v_0 of the original undeformed cell is abz . Simple geometric considerations show that when $w_{max} \ll a$ the increase in volume due to the bowing out of the walls is

$$\Delta v = ab \frac{w_{max}}{2} \quad [1]$$

Δv is also equal to the increase in volume of the liquid due to thermal

expansion. Using the thermal expansion coefficient α_L of the liquid, we can express this as

$$\Delta l = abz\alpha_L(T - T_0). \quad [2]$$

Since Eqs. [1] and [2] must be equal,

$$w_{max} = 2z\alpha_L(T - T_0). \quad [3]$$

To get the pressure p required to give a deformation w_{max} is a standard problem in the strength of materials. It involves the cell dimensions and the mechanical properties of glass. For our particular case of a plate of uniform thickness held at the edges,¹ the solution is

$$w_{max} = \frac{Cpa^4}{Et^3}, \quad [4]$$

where E is Young's modulus and, for typical glasses, has the value 6×10^{11} dynes/cm². C is a tabulated function that depends on the ratio a/b , i.e., the ratio of cell width to cell length. t is the thickness of the glass. From Eqs. [3] and [4] we get

$$p = \frac{2\alpha_L zEt^3(T - T_0)}{Ca^4}. \quad [5]$$

For MBBA (N-(p'-methoxybenzylidene)-p-n butylaniline), α_L has the value of 0.85×10^{-3} over the range of interest.² (The volume change at the nematic-isotropic transition is small compared to the thermal expansion and will be neglected.)

Effect of Temperature Change

The magnitude of the pressure developed by thermal expansion is shown in Fig. 2 for a cell 1 cm wide, 2 cm long, made of glass 1.0 mm thick and filled with a layer of MBBA 12.5 μ m thick ($\frac{1}{2}$ mil). For these dimensions the value of C is 0.11.

Three cases of filling and sealing are shown, corresponding to three different temperatures T_0 : 0°, 25°, and 50°C. The pressure change Δp may be either positive or negative, depending on whether the ambient temperature is greater than or less than T_0 . The final cell pressure difference may amount to about 1 atmosphere for an operating range of 100°C. The pressure inside the cell will fluctuate continuously as the ambient temperature changes. This will be a continuous test of the hermetic sealing plugs. Eq. [5] shows the factors in cell design that lead to high pressures. These are the thickness of the liquid

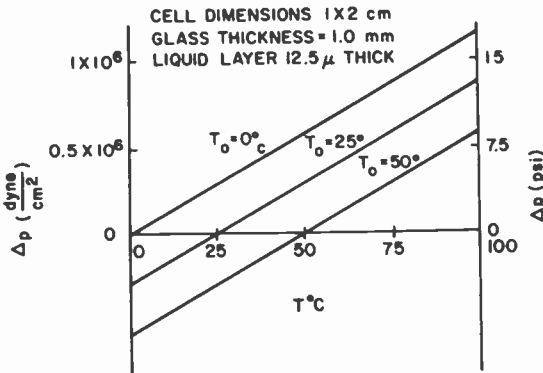


Fig. 2—Pressure changes Δp that result when a cell is filled at one temperature, T_0 , and put in an ambient at another temperature, T .

layer, the thickness of the glass plates, and the overall cell size. The effect will be most serious for small cells, such as watch displays, and it can be alleviated by using thinner glass and thinner layers of liquid crystal.

Effect of Glass Thickness

Fig. 3 shows the effect of the thickness of the glass plates for a given temperature change with other conditions fixed. This is the t^3 depen-

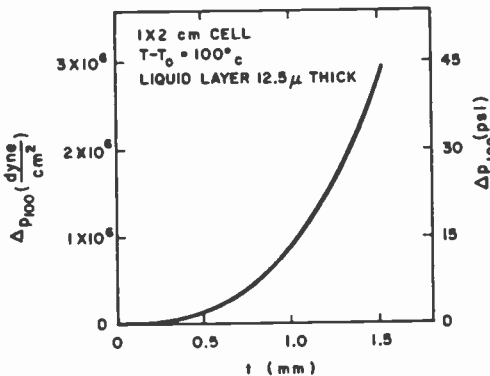


Fig. 3—Effect of the thickness t of the glass plates on the pressure change Δp_{100} , caused by heating the cell 100° above the filling temperature.

Recent Papers by RCA Authors

Listing is alphabetical by name of primary author. For copies of reprints, the reader should contact the publication directly.

- B. Abeles and P. Sheng, "Hopping Conductivity in Granular Disordered Systems," *Proc. of Amorphous & Semiconductors Conf.*, p. 1321.
- A. Aksevad, R. E. Novak, and D. L. Patterson, "New Bi-Based Garnet Films for Magnetic-Bubble Devices with Magneto-Optic Applications," *Amer. Inst. Phys. Conf. Proc. #18, 19th Annual Conf.*, p. 949, 1973.
- J. Blanc, "Diffusion Coefficients Varying with a Power of the Concentration: Convenient Solutions and a Reexamination of Zn in GaAs," *J. Appl. Phys.* Vol. 45, No. 5.
- A. Bloom, R. A. Bartolini, and D. L. Ross, "An Organic Recording Medium for Volume-Phase Holography," *Appl. Phys. Letters*, Vol. 24, No. 12, p. 612, June 15, 1974.
- D. P. Bortfeld, "Analysis of Heterojunction Optical Waveguides with a Modulated Region Smaller than the Guide Width," *J. Quant. Electronics*, Vol. QE-10, No. 7, p. 551, July 1974.
- J. Conradi, "Temperature Effects in Silicon Avalanche Diodes," *Solid State Electronics*, Vol. 17, p. 99, 1974.
- G. W. Cullen, M. T. Duffy, and C. C. Wang, "Materials Integration through Heteroepitaxial Growth on Insulating Substrates," *Chemical Vapor Disposition, 4th Int'l. Conf.*, Oct. 1973.
- W. Czaja, and C. F. Schwerdtfeger, "Evidence for Bose-Einstein Condensation of Free Excitons in AgBr," *Solid State Communications*, Vol. 15, No. 1, p. 87, 1974.
- J. G. Davy and J. J. Hanak, "RF Bias Evaporation (Ion Plating) of Nonmetal Thin Films," *J. Vac. Sci. & Tech.*, Vol. 11, No. 1, p. 43, Jan./Feb. 1974.
- D. A. deWolf, "Strong Irradiance Fluctuations in Turbulent Air, III. Diffraction Cutoff," *J. Opt. Soc. Amer.*, Vol. 64, No. 3, p. 360, March 1974.
- J. P. Dismukes and B. J. Curtis, "An Investigation of Convective Effects," *Chemical Vapor Disposition, 4th Int'l. Conf.*, Boston, Oct. 1973.
- J. P. Dismukes, J. Kane, B. Binggeli, and H. P. Schweizer, "Chemical Vapor Disposition of Cathodoluminescent Phosphor Layers," *Chemical Vapor Disposition, 4th Int'l. Conf.*, Boston, Oct. 1973.
- M. Ettenberg, H. Kressel, and H. F. Lockwood, "Degradation of $Al_xGa_{1-x}As$ Heterojunction Electro-luminescent Devices," *Appl. Phys. Letters*, Vol. 25, No. 1, p. 82, July 1974.
- K. Feher, "Digital/Analog Microwave Transmission Study," Doctorate Thesis presented at the Univ. of Sherbrooke, March 1974.
- W. H. Fonger and C. W. Struck, "Relation Between the Huang-Rhys-Pekar and the Single-Configurational-Coordinate Models of Localized Centers," *J. Luminescence*, Vol. 8, No. 6, p. 452, April 1974.
- H. Fujita and Y. Okada, "Measurements of the Reflectivity of Single Crystal Ag_2F at Room Temperature," *J. Phys. Soc. Japan*, Vol. 37, No. 1, p. 104, July 1974.
- J. I. Gittleman, B. Abeles, and S. Bozowski, "Superparamagnetism and Relaxation effects in Granular $Ni-SiO_2$ and $Ni-Al_2O_3$ Films," *Phys. Rev. B.*, Vol. 9, No. 9, May 1974.
- M. Glicksman, R. E. Enstrom, S. A. Mittleman, and J. R. Appert, "Electron Mobility in $In_xGa_{1-x}As$ Alloys," *Phys. Rev.*, Vol. 9, No. 4, p. 1621, Feb. 15, 1974.
- J. M. Hammer and W. Phillips, "Low-Loss Single-Mode Optical Waveguides and Efficient High-Speed Modulators of $LiNb_3Ta_{1-x}O_3$," *Appl. Phys. Letters* 1, Vol. 24, No. 11, June 1974.
- T. T. Hitch, "Adhesion, Phase Morphology, and Bondability of Reactively Bonded and Frit-Bonded Gold and Silver Thick-Film Conductors," *J. Electronic Materials*, Vol. 3, No. 1, p. 552, 1974.
- T. T. Hitch and J. J. Nunes, "A Method for the Rapid Orientation of Back-Reflection Laue X-ray Photographs for Zinc," *J. Appl. Crystallography*, Vol. 7, Pt. 1, Feb 1974
- E. F. Hockings, "Selection of Scientific Periodicals in an Industrial Research Library," *J. Amer. Soc. for Information Science*, Vol. 25, No. 2, March & Apr. '74.
- R. E. Honig, "Analysis of Surfaces and Thin Films by Mass Spectrometry," *Advances in Mass Spectrometry*, Vol. 6, p. 337, 1974.
- H. O. Hook, "Abstract: The Capabilities and Limitations of Photolithography," *J. Vac. Sci. Tech.*, Vol. 11, No. 1, Jan/Feb. 1974
- M. M. Hopkins and A. Miller, "Optical Waveguides in Barium Sodium Niobate," *Appl. Phys. Letters*, Vol. 25, No. 1, p. 47, July 1974.

- M. Inoue, "Lattice Green's Function for the Face Centered Cubic Lattice," *Amer. Inst. Phys.*, Feb. 12, 1974 and *J. Math. Phys.*, Vol. 15, No. 6, June 1974.
- V. K. Jha, "Cascaded Network Optimization Program," *Trans. IEEE Microwave Theory and Tech.*, Vol. 22, No. 3, March 1974.
- H. Kawamoto, "P⁺Graded Junction-N⁺ High-Efficiency Avalanche (Trapatt) Diode," *Supplement to J. Jap. Soc. Appl. Phys.*, Vol. 43, p. 246, 1974.
- S. A. Keneman, "Surface Relief Holograms in Evaporated Arsenic Trisulfide Films," *Thin Solid Films*, Vol. 21, p. 281-285, 1974.
- W. F. Kosonocky, J. E. Carnes, M. G. Kovac, P. Levine, F. V. Shallcross, and R. L. Rodgers, "Control of Blooming in Charge Coupled Imagers," *RCA Rev.*, Vol. 35, No. 1, p. 3, March 1974.
- H. Kressel and H. F. Lockwood, "A Review of Gradual Degradation Phenomena in Electroluminescent Diodes," *J. de Physique*, Vol. 35, No. 4, p. C3-223, April 1974.
- H. Kressel, P. Robinson, S. H. McFarlane, R. V. D'Aiello, and V. L. Dalal, "Epitaxial Silicon P-N Junctions on Polycrystalline Ribbons Substrates," *Appl. Phys. Letters*, Vol. 25, No. 4, p. 197, Aug. 1974.
- I. Ladany and C. C. Wang, "Properties of GaP Light-Emitting Diodes Grown on Spinel Substrates," *Solid State Electronics* '74, Vol. 17, p. 573.
- H. W. Lehmann and R. Widmer, "Abstract: RF Sputtering of ZnO Films," *J. Vac. Sci. and Tech.*, Vol. 11, No. 1, Jan/Feb. 1974.
- A. W. Levine, "Structure-Property Relationships in Thermotropic Organic Liquid Crystals," *RCA Rev.*, Vol. 35, No. 1, p. 94, March 1974.
- H. F. Lockwood, T. E. Stockton, K. F. Etzold, and D. P. Marinelli, "The GaAs P-N-P-N Laser Diode," *J. Quant. Electronics*, Vol. QE-10, No. 7, p. 567, July 1974.
- R. U. Martinelli, "Effects of Cathode Bumpiness on the Spatial Resolution of Proximity Focused Image Tubes," *Appl. Optics*, Vol. 12, No. 8, Aug. 1973.
- R. U. Martinelli, "Secondary Emission and Photoemission from Negative Electron Affinity GaP:Cs," *J. Appl. Physics*, Vol. 45, No. 7, p. 3203, July 1974.
- Y. Okada, and H. Fujita, "A Near-Normal Incidence Scanning Reflectometer in the Visible Range," *Japanese J. Applied Physics*, Vol. 13, No. 2, p. 341, Sept. 29, 1973.
- F. Okamoto, "Chemical Etchants for the Fabrication of Thin Film Patterns of Silver on Acid- and Base-Sensitive Oxides," *Japanese J. Appl. Phys.*, Letter to the Editor, Vol. 13, No. 2, p. 383, Oct. 1973.
- J. I. Pankove, J. E. Berkeyheiser and E. A. Miller, "Properties of Zn-doped GaN: 1. Photoluminescence," *J. Appl. Phys.*, Vol. 45, No. 3, March 1974.
- J. I. Pankove and H. E. P. Schade, "Photoemission from GaN," *Appl. Phys. Letters*, Vol. 25, No. 1, p. 53, July 1974.
- S. M. Perlow, "Intermodulation Distortion in Resistive Mixers," *RCA Rev.*, Vol. 35, No. 1, p. 25, March 1974.
- E. B. Priestley, "Nematic Order: The Long Range Orientational Distribution Function," *RCA Rev.*, Vol. 35, No. 1, p. 144, March 1974.
- E. B. Priestley, "Liquid Crystal Mesophases," *RCA Rev.*, Vol. 35, No. 1, p. 81, March 1974.
- W. Rehwald and R. Widmer, "Crystal Growth and Elastic, Piezoelectric, and Ultrasonic Properties of Bismuth Orthosilicate Bi₄(SiO₄)₃," *J. Phys. and Chem. of Solids*, Vol. 34, No. 12, p. 2269, Feb. 5, 1973.
- W. Rehwald, "The Study of Structural Phase Transitions by Means of Ultrasonic Experiments," *Advances in Phys.*, Vol. 22, No. 6, p. 721, Nov. 1973.
- L. Schiff, "Random-Access Digital Communication for Mobile Radio in a Cellular Environment," *IEEE Trans. Communications*, Vol. COM22, No. 5, p. 689, May 1974.
- P. Sheng, "Hard Rod Model of the Nematic-Isotropic Phase Transition," *RCA Rev.* Vol. 35, No. 1, p. 132, March 1974.
- I. P. Shkarofsky, "Voltage Gradients in Turbulent Arcs," *Canadian J. Phys.* Vol. 52, No. 1, p. 68, 1974.
- H. S. Sommers, Jr. and D. O. North, "Spontaneous Power and the Coherent State of Injection Lasers," *J. Appl. Phys.*, Vol. 45, No. 4, April 1974.
- P. D. Southgate, "Impedance Matching of Pyroelectric Radiation Sensors Using Alternating Series Elements," *Proc. IEEE*, Vol. 62, No. 4, p. 540, April 1974.
- D. L. Staebler and W. Phillips, "Fe-Doped LiNbO₃ for Read-Write Applications," *Appl. Optics*, Vol. 13, No. 4, April 1974.
- E. F. Steigmeier, H. Auderset, and G. Harbecke, "Soft Mode and Critical Opalescence in SrTiO₃," *Anharmonic Lattices, Structural Transitions and Melting, NATO-A.S.I., Applied Sciences Series*, No. 1, p. 153-160, 1974.
- C. W. Struck and W. H. Fonger, "Recursion Analysis of the Configurational Coordinate Model for Equal Force Constants," *J. Chem. Phys.*, Vol. 60, No. 5, March 1974.
- C. W. Struck and W. H. Fonger, "Condon Moments for the Configurational Coordinate Model," *J. Chem. Phys.*, Vol. 60, No. 5, March 1974.

- G. A. Swartz, Y. S. Chiang, C. P. Wen, and A. Gonzalez, "Performance of P-Type Epitaxial Silicon Millimeter-Wave Impatt Diodes," *IEEE Trans. Electron Devices*, Vol. ED-21, No. 2, p. 165, Feb. 1974.
- E. Tosatti, and G. Harbeke, "Anisotropic Exciton Polaritons," *Il Nuovo Cimento*, Vol. 22, No. 1, p. 87-109, 1974.
- D. Vilkomerson, "Acoustic Imaging with Thin Annular Apertures," *Acoustical Holography*, Vol. 5.
- J. L. Vossen, G. L. Schnable, and W. Kern, "Process for Multilevel Metallization," *J. Vac. Sci. and Tech.*, Vol. 11, No. 1, Jan/Feb. 1974.
- C. C. Wang, F. C. Dougherty, P. J. Zanzucchi, and S. H. McFarlane, III, "Epitaxial Growth and Properties of GaAs on Magnesium Aluminate Spinel," *J. Electrochem. Soc.*, Vol. 121, No. 4, April 1974.
- H. A. Weakliem, R. Braunstein, and R. Stearns, "Wavelength Modulation Spectra of SrTiO₃," *Solid State Communications*, Vol. 15, No. 1, p. 5-8, 1974.
- R. K. Wehner, "Small-Angle Scattering of Phonons and Sound Propagation in Liquid Helium Below 0.6 K," *Phys. Rev. A*, Vol. 9, No. 6.
- J. Weisbecker, "A Simplified Microcomputer Architecture," *Computer Reprint*, p. 41, March 1974.
- C. E. Weitzel, "Changes in the Photoconductivity of Sputtered Films of Cadmium Sulphide Resulting from Oxygen Chemisorption," *Surface Science*, Vol. 40, p. 555, 1973.
- R. Williams, "Image Force Interactions at the Interface Between an Insulator and a Semiconductor," *J. Appl. Phys.*, Vol. 45, No. 3, p. 1239, March 1974.
- R. Williams and R. S. Crandall, "The Structure of Crystallized Suspensions of Polystyrene Spheres," *Phys. Letters*, Vol. 48A, No. 3, p. 225, June 1974.
- P. J. Wojtowicz, "Introduction to the Molecular Theory of Nematic Liquid Crystals," *RCA Rev.* Vol. 35, No. 1, p. 105, March 1974.
- P. J. Wojtowicz, "Generalized Mean Field Theory of Nematic Liquid Crystals," *RCA Rev.*, Vol. 35, No. 1, p. 105, March 1974.
- P. J. Wojtowicz and P. Sheng, "Critical Point in the Magnetic Field-Temperature Phase Diagram of Nematic Liquid Crystals," *Phys. Letters*, Vol. 48A, No. 3, p. 235, June 1974.
- W. M. Yim and R. J. Paff, "Thermal Expansion of AlN, Sapphire, and Silicon," *J. Appl. Phys.*, Vol. 45, No. 3, p. 1456, March 1974.
- W. M. Yim and J. P. Dismukes, "A Survey of Interface Stability Criteria in the Elemental Alloy Systems: Ge-Si, Bi-Sb, and Se-Te," *J. Crystal Growth*, Vol. 22, p. 287, 1974.

Patents Issued to RCA Inventors Second Quarter 1974

April

- J. Avins Brightness Control (3,804,981)
J. N. Breckman Separation Control of Aircraft by Non-Synchronous Techniques (3,803,608)
Y. C. Brill Dual Thrust Level Monopropellant Spacecraft Propulsion System (3,807,657)
L. R. Campbell Capacitive-Discharge Timing Circuit Using Comparator Transistor Base Current to Determine Discharge Rate (3,808,466)
B. Case and J. E. Miller Digital Range Rate Computer (3,803,602)
B. Case Digital Tracker (3,803,604)
B. Case and J. E. Miller Track Gate Movement Limiter (3,803,605)
R. B. Clover, Jr. Low Birefringent Orthoferrites (3,804,766)
D. F. Griepentrog and R. J. Gries Instant-On Circuit for a Television Receiver (3,801,856)
J. R. Hale and G. I. Merritt Method of Fabricating a Dark Heater (3,808,043)
J. J. Hanak Electroluminescent Film and Method for Preparing Same (3,803,438)
E. T. Hausman Hybrid Electron Device Containing Semiconductor Chips (3,805,117)
S. E. Hilliker Information Playback System (3,806,668)
D. S. Jacobson and R. A. Duclos Method for Making a Radio Frequency Transistor Structure (3,807,039)
I. Ladany and C. C. Wang III-V Compound on Insulating Substrate and Its Preparation and Use (3,802,967)
R. D. Larrabee Thermal Detector and Method of Making Same (3,801,949)
R. A. Lee and A. Bazarian, Jr. Method of Making a Directly-Heated Cathode (3,800,378)
D. W. Luz Television Deflector Circuit with Transformerless Coupling Between the Drive and Output State (3,801,857)
A. Miller Adaptive Surface Wave Devices (3,805,195)
A. M. Morrell Shadow Mask Mounting Assemblies (3,803,436)
F. H. Nicoll Electron-Beam Pumped Laser with Extended Life (3,803,510)
P. H. Robinson and R. O. Wance Method of Polishing Sapphire and Spinel (3,808,065)
R. S. Ronen and E. A. James Method of Depositing Electrode Leads (3,801,477)
R. A. Sanderson Apparatus for Easily Engaging, Disengaging, and Locking Load to Rotatable Driving Element (3,801,033)
J. F. Segro and G. L. Fassett Method of Installing a Mount Assembly in a Multibeam Cathode-Ray Tube (3,807,006)
A. H. Sommer Method for Making a Negative Effective Electron-Affinity Silicon Electron Emitter (3,806,372)
H. A. Stern Method of Closing a Liquid Crystal Device (3,807,127)
F. Sterzer Semiconductor Memory Element (3,805,125)
M. J. Teare Low Noise Detector Amplifier (Assigned to RCA Limited, Canada) (3,801,933)
I. F. Thompson and J. L. Smith Static Convergence Device for Electron Beams (3,808,570)
A. J. Visioli, Jr. and H. A. Whittlinger Gated Astable Multivibrator (3,805,184)
G. W. Webb Niobium-Gallium Superconductor (3,801,378)
J. A. Welsbecker Least Recently Used Location Indicator (3,806,883)

May

- J. Avins Television Receiver Using Synchronous Video Detection (3,812,289)
L. F. Crowley, A. M. Missenda, and D. R. Presky Automatic Squelch Tail Eliminator for Tone Coded Squelch Systems (3,810,023)
F. Caprari Series Regulated Power Supply for Arc Discharge Lamps Utilizing Incandescent Lamps (3,813,576)
D. E. Carlson, K. W. Hang, and G. F. Stockdale Method of Treating a Glass Body to Provide an Ion-Depleted Region Therein (3,811,855)

- J. D. Cavett and R. S. Hopkins, Jr. Video Stripper (3,813,488)
 M. T. Duffy and J. E. Carnes Aluminum Oxide Films for Electronic Devices (3,809,574)
 R. E. Flory Two Color Medium for Full Color TV Film System (3,812,528)
 R. A. Gange and C. C. Steinmetz Corona Discharge Device (3,809,974)
 A. N. Gardiner and H. A. Stern Liquid Crystal Device Closure Method (3,808,769)
 B. A. Grae and D. R. Andrews Tape Cartridge Player Cartridge Magazine (3,812,537)
 F. Z. Hawrylo and J. I. Pankove Method of Epitaxially Depositing Gallium Nitride from the Liquid Phase (3,811,963)
 R. C. Heuner and S. J. Niemiec Liquid Crystal Display (3,809,458)
 L. R. Hulls Magnetic Reed Sensor Suitable for use in Ignition Timing Systems (3,813,596)
 J. C. Marsh, Jr. Independent Electron Gun Bias Control (3,812,397)
 R. E. Marx Impedance Control Using Transferred Electron Devices (3,812,437)
 A. M. Morrell and F. Van Hekken Correcting Lens (3,811,754)
 M. N. Norman High Voltage Protection Circuit (3, 313, 580)
 N. R. Scheinberg High Speed Signal Following Circuit (3,812,383)
 A. C. N. Sheng Current Source (3,813,595)
 G. E. Skorup Set-Reset Flip-Flop (3,812,384)
 B. K. Smith Method for Coating only the Convex Major Surface of an Apertured Mask for a Cathode-Ray Tube (3,811,926)
 J. P. Watson Hinged Drum System (3,813,678)
 P. K. Welmer Charge Transfer Fan-In Circuitry (3,811,055)
 A. W. Young Window Detector Circuit (3,809,926)

June

- A. A. A. Ahmed Comparator Circuitry (3,816,761)
 F. X. Beck, Jr. and W. E. Kinslow, Jr. Merchandise Handling and Identifying System (3,819,012)
 M. Ettenberg Method of Epitaxially Depositing a Semiconductor Material on a Substrate (3,821,039)
 G. L. Fassett Method of Rebuilding a Cathode-Ray Tube (3,816,891)
 D. D. Freedman High-Speed Logic Circuits (3,818,242)
 N. S. Freedman, C. W. Horsting, W. F. Lawrence, and J. J. Corona Thermo-Electric Modular Structure and Method of Making Same (3,814,633)
 F. Gordon and D. R. Andrews Apparatus for Providing Individual Adjustment of Movable Multiple Transducers in a Plural Tape Cartridge Player (3,821,814)
 R. B. Goyer Digital Interface Circuit for a Random Noise Generator (3,816,765)
 D. L. Greenaway Identification Card Decoder (3,819,911)
 P. E. Haferl S-Corrected Waveform Generator (3,814,980)
 R. E. Hartwell Flowmeter (3,820,395)
 K. Katagi, W. L. Ross, and J. J. Lyon Glitch Free Vector Generation (3,821,728)
 M. T. McCaffrey and J. A. Castellano Novel Electro-Optic Devices (3,816,336)
 D. A. McClure and H. C. Nichols Balanced, Low Impedance, High Frequency Transmission Line (3,815,054)
 D. L. Neal Television Receiver Service Adjustment System (3,820,155)
 D. H. Pritchard and A. C. Schroeder Color Television (3,820,157)
 J. P. Russell and D. L. Greenaway Cryptographically Coded Cards Employing Synthetic Light Modifying Portion (3,814,904)
 H. C. Schindler Liquid-Crystal Display Device and Method of Making (3,814,501)
 J. H. Shelby and F. E. Richter Film Type Capacitor and Method of Adjustment (3,821,617)
 S. A. Steckler Controlled Oscillator (3,815,051)
 C. F. Wheatley, Jr. Current Translating Circuits (3,815,037)
 R. J. Williams Passive Cooler (3,817,320)

AUTHORS



Elmer L. Allen, Jr. attended the Philadelphia Wireless Institute in 1946. After graduating, he worked with specialized electronic equipments for military, space, and medical applications (working with digital, analog, and rf circuits) for the Philco Corporation, Nuclear Electronics Company, and the General Electric Company. He joined RCA Laboratories in 1970 and is currently engaged in solid-state microwave research.



Peter V. Goedertler obtained his Bachelor's Degree at the University of Louvain, Belgium and took a License Degree in Mathematics at the same University, majoring in theoretical physics. He taught statistics at the Antwerp Business School, and was granted a leave of absence to study microwave theory and techniques at Cruft Laboratory, Harvard University, in 1947-1948. After that, he was appointed Professor of Physics at the Philosophical College of Louvain. In 1954, he started and conducted a research project on microwave spectroscopy at the Center of Physique Nucleaire of the University of Louvain. His main work was a determination of the molecular structural constants of vinyl bromide and its deuterio substitutes. In 1958 he came to the United States and worked as a Research Associate in the Microwave Spectroscopy Group of Duke University, until joining RCA Laboratories, Princeton, N. J. in 1959. At RCA Laboratories he first studied the interaction of gas molecules with crystalline fields; in the course of this work he developed a new kind of Cs-ion source. He has been engaged in the early research on optical masers, with both gaseous and solid-state materials. He was a co-discoverer of the He-Ne "cascade" laser, and in 1965 was given an RCA Laboratories Achievement Award for his contributions to the development of the cross-pumped YAG:Nd:Cr laser.

For the last three years, he has been working on the development of various optical systems related to the processing and the display of video information.



Lawrence A. Goodman received the B.S., M.S., and Ph.D. degrees in Electrical Engineering from M.I.T. He joined RCA Laboratories in 1970 after completing his doctoral dissertation on the optical properties of cadmium sulfide. Since coming to RCA, Dr. Goodman has been investigating various aspects of liquid-crystal displays. These studies have included conductive-electrode preparation, surface-alignment phenomena, bulk electro-optic effects, and various approaches to electrically addressing liquid-crystal displays. He is a member of IEEE, SID, Tau Beta Pi, and Eta Kappa Nu.



Istvan Gorog received the B.Sc. (1961), M.Sc. (1962) and Ph.D. (1964) degrees in Electrical Engineering from the University of California at Berkeley. In 1964, Dr. Gorog joined the technical staff of the RCA Laboratories, Princeton, N. J., where his main areas of concern have been quantum electronics and electro-optical systems. His activities have included gas-laser research, holography, investigation of recording and playback techniques for prerecorded video, laser deflection, photochromic and cathodochromic devices and systems. His most recent investigations have been concerned

with the implications of the results of recent measurements of human visual perception for electronic imaging. Currently he is Head of the Optical Electronics Research Group in the Physical Electronics Research Laboratory.

During 1968 he was on leave of absence from RCA as a National Science Foundation Post-Doctoral Fellow at the Laboratori Nazionali di Frascati and the European Space Research Institute in Frascati, Italy, where he worked on the problems of production of high-temperature plasmas by laser irradiation of solid targets and scattering of laser radiation by collective plasma fluctuations.

Dr. Gorog is a member of the American Physical Society and of Eta Kappa Nu.



Joseph J. Hanak received his B.S. degree from Manhattan College in 1953, his M.S. in physical chemistry from the University of Detroit in 1956, and his Ph.D. in physical chemistry from Iowa State University in 1959. He was employed as a chemist at the Ethyl Corporation in 1954 and as a graduate research assistant at the AEC Institute for Atomic Research (Ames, Iowa) from 1955 to 1959. He joined RCA Laboratories in 1959, and is now a Fellow of the Technical Staff. Dr. Hanak has been active in the field of chemistry, metallurgy, and crystallography of the rare earth elements. He is the inventor of a vapor deposition process for Nb_3Sn ,

a process used in the construction of high-field superconducting solenoids. He has developed fabrication techniques for single-crystal ferrite recording magnetic heads. He introduced novel co-sputtering methods applicable to a large variety of materials, thereby greatly increasing productivity in materials research. Currently, he is active in the field of electroluminescence. In 1969-1970 he spent a year at RCA Laboratories, Ltd., Zurich, Switzerland on a European Research Fellowship. He was recipient of the RCA David Sarnoff Award, the John Roebling American Society for Metals Award, and three RCA Laboratories Awards for his achievements in the field of materials research.

Dr. Hanak is a member of the American Vacuum Society and of Sigma Xi.



Hirohisa Kawamoto received the B.S. degree in Electronics from Kyoto University, Kyoto, Japan, in 1961. He received the M.S. degree in 1966 and the Ph.D. degree in 1970, both in Electrical Engineering and Computer Sciences from the University of California, Berkeley. From 1961 to 1964 and from 1966 to 1968 he worked at Matsushita Electronics Corporation, Osaka, Japan. He was engaged in the study of second breakdown for p-n junctions and contributed to the development of the first transistorized 9-inch television receiver. In 1967 he was responsible for the operation of quality assurance in the Integrated Circuit Division. From 1964 to

1966 and from 1968 to 1969, he worked for the Electronics Research Laboratory at the University of California at Berkeley. He did the analysis and computer simulations on a breakdown caused by conductivity modulation in p-n-n⁺ junctions. He also did research on radiation damage in semiconductors, focusing on the recombination-generation processes inside neutron-irradiated silicon. In 1970, he became an Acting Assistant Professor at the Department of Electrical Engineering and Computer Sciences at the University of California, Berkeley. He joined RCA Laboratories in 1970 as a project scientist for the Trapatt amplifier program. In 1973 he received an RCA Achievement Award for a team effort in the development of S-band Trapatt amplifiers.

Presently, he is working on video discs and charge-coupled devices. He is a member of IEEE, Eta Kappa Nu, and Sigma Xi.



Joseph D. Knox received his B.S. degree in Electrical Engineering from the University of Dayton in Dayton, Ohio in 1966 and his M.S. and Ph.D. degrees from Case Institute of Technology in Cleveland, Ohio, in January 1970 and September 1970, respectively. During his stay at Case Institute, Dr. Knox did an extensive study of the absorption of iodine 127 and iodine 129 inside and outside the cavity of a He³-Ne²⁰ laser. In the course of this work, he developed a spectroscopic technique that gave sufficient resolution to observe the actual hyperfine structure (38 lines in all) of iodine 129. Dr. Knox also engaged in a study of the He-Ce laser, high-power CO₂

lasers, the use of cold cathodes in gas lasers, and the design and development of He-Ne lasers for special applications. He joined RCA in September 1970, working on the design and development of a laser deflection display system. His other activities include the design and fabrication of acousto-optic deflectors, modulators, and cavity "dumpers" for visible and infrared lasers. Most recently, he designed and developed fabrication techniques for an advanced lead molybdate deflector for a laser deflection system. His fabrication techniques have resulted in the development of a new group of efficient microwave delay lines operating up to 18 GHz.

Dr. Knox is a member of Tau Beta Pi (Physics and Engineering Honorary), Sigma Xi, the IEEE, and the Optical Society of America.



Michael G. Kovac received the B.S. degree from the University of Notre Dame, Notre Dame, Ind., in 1963, and the M.S. and Ph.D. degrees from Northwestern University, Evanston, Ill., in 1967 and 1970, respectively, all in electrical engineering. His research activities have included investigations of an x-ray imaging system based on the electron beam scanning of a mosaic target coupled to a gas-filled detection chamber, x-ray-induced secondary electron emissions from metal-insulator layers, and various aspects of a two-dimensional, beam-scanned ultrasonic imaging system. He worked at the General Electric Industry Control Department,

Salem, Va., prior to joining RCA Laboratories in 1970. At the Laboratories, he worked on silicon and thin-film self-scanned imaging systems. His work has included investigation of both x-y addressed image sensors and of charge-transfer image sensors. He is presently with Dytron, Inc., Waltham, Mass.

Dr. Kovac is a member of Tau Beta Pi, Eta Kappa Nu, and Sigma Xi.



Ivan Ladany obtained his B.S. and M.S. degrees from Northwestern University. In 1953, he joined the Naval Research Laboratory in Washington, D. C., where he worked briefly in the field of underwater sound, spending most of his time in semiconductor device research. Since coming to RCA Laboratories in 1966, he has worked in GaP, GaAlP and GaAs luminescent diode research and developed a technique now widely used in increasing the GaP LED (red) efficiency. In 1969 he was awarded an RCA Laboratories Achievement Award for his contributions to GaP electroluminescence. More recently he has worked on improved GaAs infrared diodes,

green emitting GaP LED's, and III-V compound growth on insulating substrates using liquid-phase epitaxy. At present, he is devoting most of his time to injection laser development.

Mr. Ladany is a member of the American Physical Society, the IEEE, and Sigma Xi.



Shing-Gong Liu received his B.S. degree in electrical engineering from Taiwan University, Taipei, Taiwan, in 1954, the M.S. degree in electrical engineering from North Carolina State College, Raleigh, North Carolina, in 1958, and the Ph.D. degree in electrical engineering from Stanford University, Stanford, Calif., in 1963. From 1958 to 1959 he worked with the IBM Laboratories, Poughkeepsie, New York. From 1959 to 1963, he was a research assistant at the Hansen Microwave Laboratories, Stanford University, where he worked in the field of microwave ferrites. He joined RCA Laboratories, Princeton, N. J., in 1963, and has since worked principally in

the areas of semiconductor microwave devices.

Dr. Liu is a member of Phi Kappa Phi, Sigma Xi, and the American Physical Society.



Dietrich Meyerhoffer received his Bachelor of Engineering Physics from Cornell University in 1954 and his Ph.D. degree in physics from MIT in 1958. Since 1958 he has been a member of the technical staff at RCA Laboratories. His Research activities have included the study of electrical properties of semiconductors and insulators, light emission from semiconductor diodes and lasers, and Q-switching of the CO₂ laser. From 1966 to 1968 he was associated with a laboratory doing applied research in support of the RCA Graphic Systems Division. He investigated the application of electronics and laser techniques to the printing industry. Since then he

has been with the Electronic Printing Group and has studied holographic recording in dichromated gelatin and the physical properties of liquid crystals.

Dr. Meyerhoffer is a member of the American Physical Society, the Optical Society of America, and the IEEE.



Winthrop S. Pike received the B.A. degree in physics from Williams College, Williamstown, Mass., in 1941. Shortly thereafter, he entered the U. S. Army Signal Corps as a radar officer. In 1946 he became a member of the technical staff of RCA Laboratories, Princeton, N. J. He worked on sensory aids for the blind, storage tubes and their application, color television receivers, cameras and encoders, highway-vehicle control devices, industrial and educational television camera chains, electronic devices for medical applications, high-altitude balloon-borne television systems for astronomical observations, and camera and data collecting systems

using solid-state sensors.

Mr. Pike has been the recipient of five RCA Achievement Awards.



H. John Prager is a graduate of the University of Vienna, Austria, and of the University of Michigan where he received an MSEE degree in 1940. He has been with RCA since 1943. His first assignment was with the RCA Electron Tube Division, Harrison, N. J., where he worked on the design and development of small power and receiving tubes. In 1959, he joined RCA Laboratories, Princeton, N. J., to perform research on solid-state microwave devices, such as varactors, tunnel diodes, optical devices, and avalanche diodes. In 1960, 1967, and 1972, he was co-recipient of RCA Achievement Awards for teamwork leading to the first tunnel-diode

amplifier and down-converter, the first Trapatt diode oscillator, and greatly improved S-band diode amplifiers.

Mr. Prager is a member of the IEEE.



Frank V. Shallcross received the A.B. degree in chemistry from the University of Pennsylvania, Philadelphia, in 1953, and the Ph.D. degree in physical chemistry from Brown University, Providence, R. I., in 1958. He was employed as a chemist by M. & C. Nuclear, Inc., Attleboro, Mass., from 1957 to 1958. In 1958 he joined RCA Laboratories, Princeton, N. J. At RCA he has done research on laser materials, thin-film photoconductors and semiconductors, television camera tubes, thin-film active devices, and silicon and thin-film self-scanned sensor arrays. Dr. Shallcross is the recipient of an RCA Laboratories Achievement Award.

He is a member of the American Chemical Society, the American Institute of Chemists, the American Association for the Advancement of Science, Phi Beta Kappa, and Sigma Xi.



Ping Sheng received his B.Sc. degree in Physics (with honors) from the California Institute of Technology in 1967. He received his Ph.D. in Physics from Princeton University in 1971. After spending two years at the Institute for Advanced Study, Princeton, N. J., as a visiting member of the School of Natural Sciences, Dr. Sheng joined the RCA Laboratories, Princeton, N. J., in 1973 as a member of the Physical Electronics Research Laboratory. Dr. Sheng has done research on a variety of subjects. As a graduate student his research effort was mainly directed toward positron theory and ferromagnetic transmission resonance. As a result of his work on

the transmission resonance a new technique was developed for measuring the magnetic critical exponent β . While at the Institute for Advanced Study, Dr. Sheng developed a theory for electron transport in granular metals and did research in the theory of liquid crystals. Currently he is engaged in research on the physical properties of granular metals and the theory of liquid crystals.

Dr. Sheng is a member of the American Physical Society.



David M. Stevenson received the B.Sc. degree in Physics from Leeds University, England, in 1960. From 1960 to 1963 he was on the Scientific Staff of the Hirst Research Center of the General Electric Company (England) Ltd., where he worked on a crossed field cyclotron resonance oscillator. From 1963 to 1968 he attended Cornell University and was employed as a Research and Teaching Assistant. He investigated electron and ion emission and plasma generation at laser irradiated surfaces, receiving the M.S. and Ph.D. degrees in Electrical Engineering in 1965 and 1968, respectively. From 1968 to 1973 Dr. Stevenson was a member of the

Technical Staff of the RCA Laboratories, Princeton, N. J. He worked in the Advanced Technology Laboratory on microwave power amplifiers and multipliers for high-power solid state sources and on microwave acoustic delay line and microwave integrated circuit techniques.

He is presently Manager of Microwave and Process Engineering at Varian Assoc., Salem Road, Beverly, Mass.



Paul K. Weimer received his A.B. degree from Manchester College in 1936, his M.A. degree in physics from the University of Kansas in 1938, and his Ph.D. degree in physics from Ohio State University in 1942. From 1937 to 1939, he taught physics and mathematics at Tabor College, Hillsboro, Kansas. Since 1942, Dr. Weimer has been engaged in research at RCA Laboratories, Princeton, N. J., where he is a Fellow and member of the technical staff. At the Laboratories he has participated in the basic development of various types of television tubes and solid-state devices. From 1959 to 1960, Dr. Weimer was granted an RCA fellowship for study

abroad, which was spent at the Laboratoire de Physique, Ecole Normale Supérieure, Paris, France, working in the field of semiconductors. He was recipient of a television Broadcasters' Award in 1946, the IRE Vladimir K. Zworykin Television Prize in 1959, and the 1966 IEEE Morris N. Liebmann Prize Award. In 1968, Dr. Weimer was awarded an honorary degree of Doctor of Science by Manchester College. He is a Fellow of the Institute of Electrical Engineers and a member of the American Physical Society.



Richard Williams received the AB in chemistry from Miami University and the Ph.D. in physical chemistry from Harvard University. He joined RCA Laboratories, Princeton, N. J., in 1958. He has worked in numerous areas, including semiconductor-electrolyte interfaces, liquid crystals, internal photoemission, and insulator physics. He was group leader in Insulator Physics from 1967 to 1970 and in Quantum Electronics from 1970 to 1972; in 1972, he was made a Fellow. He has received several achievement awards and shared in the David Sarnoff Team Award in Science in 1969. He was a visiting scientist at the RCA Zurich laboratory in 1963 and

has been a Fulbright Lecturer in Sao Carlos, Brazil, a summer school lecturer at Instituto Politecnico Nacional in Mexico, and a visiting lecturer at Princeton University.



James P. Wittke received the M.E. degree from Stevens Institute of Technology, Hoboken, New Jersey in 1949, and the M.A. and Ph.D. degrees in physics from Princeton University, Princeton, N. J., in 1952 and 1955, respectively. His doctoral research was a precision microwave determination of the hyperfine splitting in atomic hydrogen. He was an instructor in physics at Princeton for one year before joining the technical staff of RCA laboratories, Princeton. At RCA he has engaged in paramagnetic resonance and microwave maser studies, in research on optically excited crystal lasers, and in investigations of the motions and properties

of impurities in rutile. He has also worked on various classified projects. In 1967 Dr. Wittke was awarded an RCA Fellowship for a year of study abroad, which he spent at the Clarendon Laboratory at Oxford, England. Since then, he has studied the luminescence of heavily doped GaAs, helped develop new infrared-stimulated light emitting phosphors, and worked on the generation of ultra-short laser pulses, using mode-locking techniques. He is currently studying optical fiber communications systems, including measurements of the characteristics of fast light-emitting diodes and of various low-loss fibers.

Dr. Wittke is a member of the Optical Society of America, IEEE, and of Tau Beta Pi and a Fellow of the American Physical Society.



Peter J. Wojtowicz received his B.Sc. degree in chemistry (with highest honors) from Rutgers University in 1953. He received his M.S. in chemistry in 1954 and his Ph.D. in physical chemistry in 1956 from Yale University. He was a National Science Foundation Predoctoral fellow while at Yale, 1953-1956. His thesis was concerned with the statistical mechanics of the order-disorder phenomenon in solids and the theory of molten salts and fluid mixtures. Dr. Wojtowicz joined RCA Laboratories in 1956. He is a Member of the Technical Staff of the Physics and Chemistry of Solids Group of the Physical Electronics Research Laboratory. During 1966-67

he was acting head of the General Research Group. His research effort while at RCA has been directed chiefly toward the theory of magnetic materials including quantum and statistical mechanics of the thermal, structural, and magnetic properties of these substances. This work included the theory of the cooperative Jahn-Teller effect, the statistical mechanics of magnetic interactions and phase transitions, the theory of magnetic semiconductors, the theory of granular ferromagnetic metals, and the theory of the application of ferrites and garnets to various magnetic devices. He is currently engaged in the theory of liquid crystals and liquid-crystal phase transformations. Dr. Wojtowicz is the recipient of two RCA Laboratories Achievement Awards for the years 1962 and 1966. He is a fellow of the American Physical Society and a member of Sigma Xi and Phi Beta Kappa.

